Development of Kalman Filter based Algorithms for Fringe Pattern Analysis

A
Thesis Submitted
for the award of the Degree of
DOCTOR OF PHILOSOPHY
By

SHIKHA SHARMA
196102012

Under the Supervision of
Dr. RISHIKESH DILIP KULKARNI

Department of Electronics and Electrical Engineering
Indian Institute of Technology Guwahati
July, 2024

Declaration

This is to certify that the thesis entitled "**Development of Kalman Filter based Algorithms for Fringe Pattern Analysis**", submitted by me to the *Indian Institute of Technology Guwahati*, for the award of the degree of DOCTOR OF PHILOSOPHY, is a bonafide work carried out by me under the supervision of Dr. Rishikesh Dilip Kulkarni. The content of this thesis, in full or in parts, have not been submitted to any other University or Institute for the award of any degree or diploma. I also wish to state that to the best of my knowledge and understanding nothing in this report amounts to plagiarism.

Signed: _____

Shikha Sharma
Department of Electronics and Electrical Engineering,
Indian Institute of Technology Guwahati,
Guwahati-781039, Assam, India.

Date: _____

Certificate

This is to certify that the thesis entitled "**Development of Kalman Filter based Algorithms for Fringe Pattern Analysis**", submitted by Shikha Sharma (196102012), a research scholar in the *Department of Electronics and Electrical Engineering*, *Indian Institute of Technology Guwahati*, for the award of the degree of DOCTOR OF PHILOSOPHY, is a record of an original research work carried out by her under my supervision and guidance. The thesis has fulfilled all requirements as per the regulations of the institute and in my opinion has reached the standard needed for submission. The results embodied in this thesis have not been submitted to any other University or Institute for the award of any degree or diploma.

Signed: _____

Supervisor: Dr. Rishikesh Dilip Kulkarni
Department of Electronics and Electrical Engineering,
Indian Institute of Technology Guwahati,
Guwahati-781039, Assam, India.

Date: _____

Acknowledgements

I feel the inadequacy of words to express my deep sense of gratitude to my research supervisor, Dr. Rishikesh Dilip Kulkarni, for providing me an opportunity to work under his guidance. Your friendly support, constant motivation, worthy guidance and key criticism to my research methodologies ushered qualitative improvement of this manuscript. I am thankful to you for providing all the necessary inputs and a healthy work environment at our Lab and infinite degree of freedom to work on the principle of 'learning by doing' that undergoes several round of 'trial and hit' that imbibes the spirit of research that is ultimately assimilated.

I record my respectful indebtedness and gratitude to my parents Sri Sanjeev Sharma and smt. Usha Sharma, for their blessings, encouragement, unquantifiable love and affection. I attribute this achievement to my siblings for their constant blessings, support, silent prayers for my success and moreover, making me stand in this position. I wish to place a record of my sincere and heartfelt gratitude to the DC members, Dr. M.K.Bhuyan, Dr. Bosanta Ranjan Boruah and Dr. Prithwijit Guha, for their invaluable comments and suggestions during research, presentation and scientific writing of this manuscript. I extend my sincere thank to all other faculty members and and non-teaching staff of the Department of Electronics and Electrical Engineering for their love, care and familial support, who were ready round the clock to extend their help.

I finally thank all those who have helped me overtly or covertly to complete the research and study to the best of my satisfaction.

Sincerely
Shikha Sharma

Abstract

Optical interferometric measurement techniques such as optical interferometry, electronic speckle pattern interferometry, digital holographic interferometry, shearography, Moiré interferometry, fringe projection profilometry, etc. have proved to be powerful tools used for the measurement of physical parameters such as surface deformation, refractive index variations, object shape, temperature, etc. These techniques have been employed in a number of engineering and scientific applications ranging from structural health monitoring, non-destructive testing, material characterization, surface profilometry to art preservation and biomedical imaging. These setup usually involve recording of intensity of an interference pattern generated between an object perturbed and an object unperturbed wavefronts. The object perturbation typically introduces change in the phase of the wavefront. This change in phase is encoded in the form of sinusoidal variations in the intensity of the interference pattern, which is commonly termed as *interferogram* or *fringe pattern*. It is interesting to note that the other modalities such as synthetic aperture radar interferometry, magnetic resonance image, etc. also involve encoding of information in the form of phase. Therefore, the phase retrieval is essential from the fringe pattern in order to derive the object information. The purpose of fringe pattern analysis to retrieve the phase from the fringe pattern. Therefore, demand for the phase information has promoted the development of fringe analysis techniques. Spatial fringe analysis techniques typically involve different operations such as fringe denoising, fringe normalization, and fringe pattern demodulation for the phase estimation. In some cases, phase aberration compensation is also required to be performed. The thesis presents a number of spatial fringe processing algorithms based on the application of Kalman filter.

The Kalman filter is a widely popular tool for the estimation of state of a discrete-time system governed by linear stochastic difference equation. The state updates are governed by the system and measurement models. The Kalman filter has found numerous applications in systems such as navigation, communication, control, signal processing, etc. Basically, the employability of the Kalman filter depends mainly on one's ability to represent the problem at hand in a state-space form. In the present work, different state-space formulation have been developed depending on the particular fringe processing operations. In doing so, different variants of the Kalman filter are utilized depending

on the system and measurement models. In cases wherein the system and measurement models involve linear functions of the states, the standard linear Kalman filter is utilized. On the other hand, if system and/or measurement models involve nonlinear functions of the states, nonlinear version of the Kalman filter is utilized. Noting the fact that the Kalman filter is employed to fringe images which are finite in size, the fixed-length Kalman smoothing algorithm has been used for the improvement in state estimation accuracy. In general, some of the filter parameters such as process and measurement error covariance matrices are set in an empirical manner. In order to make the fringe processing operation automatic, the advanced techniques of adaptive estimation of these parameters have also been utilized.

The Kalman filter based spatial fringe analysis techniques have been developed for fringe pattern denoising, fringe normalization, and carrier modulated fringe pattern demodulation for the phase estimation. The challenging problem of closed fringe pattern demodulation has also been addressed. Numerous simulation and experimental examples have been provided. The salient features of the proposed techniques are robustness against the additive and speckle noise, good accuracy, low computational complexity, localized fringe processing, minimum or no user-defined algorithm parameters, performance independent of fringe density, ability to handle inherent fringe discontinuities, etc. The comparison of these techniques are provided with state-of-art methods to demonstrate their practical applicability.

We believe that the proposed set of spatial fringe analysis tools can prove to be an important addition to the interferometric measurement techniques for the accurate measurement of various physical parameters of interest.

Keywords: Fringe analysis, fringe denoising, fringe pattern normalization, fringe pattern demodulation, phase estimation, speckle noise, Kalman filter, extended Kalman filter, speckle interferometry, digital holographic microscopy, fringe projection profilometry.

Contents

List of Figures

List of Tables

List of Publications

Journal (Published)

- S. Sharma, and R. Kulkarni, **"Phase demodulation from a spatial carrier fringe pattern using extended complex Kalman filter"**, *Optics and Lasers in Engineering*, vol. 138, 106409, 2021.
- S. Sharma, and R. Kulkarni, S. Ajithaprasad, and R. Gannavarpu, **"Fringe pattern normalization algorithm using Kalman filter"**, *Results in Optics*, vol. 5, 100152, 2021.
- S. Sharma, and R. Kulkarni, **"Noise reduction in speckle interferometry fringe pattern using adaptive Kalman filter "**, *Optical Engineering*, vol. 60, no. 12, 124105, 2021.
- S. Sharma, and R. Kulkarni, and R. Gannavarpu, **"Wrapped phase denoising using adaptive Kalman smoother algorithm"**, *Journal of Modern Optics*, vol. 69, no. 15, 838-849, 2022.
- S. Sharma, and R. Kulkarni, **"Fringe Pattern Demodulation using Zernike Polynomials and l1-norm Regularized Extended Kalman filter"**, *Applied Optics*, vol. 61, no. 18, 5517-5523, 2022.
- S. Sharma, and R. Kulkarni, **"Adaptive extended complex Kalman filter based spatial carrier fringe pattern demodulation"**, *Asian Journal of Physics*, vol. 31, 961-971, 2022.
- S. Sharma, and R. Kulkarni, **"State space modelling approach for fringe pattern demodulation"**, *Applied Optics*, vol. 62, no. 27, 7330-7337, 2023.

Manuscript under preparation (Journal)

- R. Kulkarni, S. Sharma, M. Nystad, B.S. Ahluwalia, and A. Ahmad, **"Phase aberration compensation in digital holographic microscopy using Kalman Filter"**.

Chapter 1

Background

1.1 Introduction

In the interferometric measurement techniques such as optical interferometry, digital holographic interferometry, electronic speckle pattern interferometry, shearography, etc., the information on the measurand, for example, surface deformation, refractive index, shape, etc. is encoded in the phase of an optical wavefront [8, 9]. These technique have been used in various engineering and scientific applications such as non-destructive testing [10], art preservation, surface profilometry, structural health monitoring [11], biophotonics [12], etc.

In general, direct phase recording is not possible with a digital image sensors such as charged-couple device (CCD) and complementary metal oxide semiconductor (CMOS). Consequently, optical interferometric arrangements are utilized to encode the phase information in the form of an image with sinusoidally varying intensity. Such an image is commonly termed as *interferogram* or *fringe pattern*. A fringe pattern can be typically represented as [13]

$$\mathrm{I(x,y)} = \mathrm{a(x,y)} + \mathrm{b(x,y)}\cos[\phi(\mathrm{x,y})], \tag{1.1}$$

where, (x, y) represent the spatial coordinates; I(x, y), a(x, y) and b(x, y) represent the fringe intensity, background intensity and modulation amplitude, respectively; ϕ(x, y) represents the sought phase. It is interesting to note that the expression of the fringe pattern in Eq. (1.1) is applicable in other measurement modalities such as Moiré interferometry and fringe projection profilometry. Apart from the real-valued fringe pattern, a complex-valued fringe pattern or exponential fringe pattern (EPF) is involved in digital holographic interferometry, interferometric synthetic aperture radar imaging (InSAR),

magnetic resonance imaging (MRI), and interferometric synthetic aperture sonar (InSAS). The InSAR is a coherent interferometric imaging technique used to generate high-resolution images of the terrain surface. In this technique, the EPF signal carries the information about the height of each point of the recorded data in the form of phase (ϕ). The similar coherent interferometric imaging method is used in the InSAS to generate underwater images. The MRI involves recording of the information about the internal structure of body parts in the form of EPF. Whereas the amplitude of such an EPF carries the structural information of the body parts, the phase of the EPF carriers the information on the magnetic field inhomogeneities. The expression for EPF can be given as

$$\mathrm{I}(\mathrm{x},\mathrm{y}) = \mathrm{A}(\mathrm{x},\mathrm{y})\exp\left[\mathrm{j}\phi(\mathrm{x},\mathrm{y})\right], \tag{1.2}$$

where $\mathrm{A}(\mathrm{x},\mathrm{y})$ and $\phi(\mathrm{x},\mathrm{y})$ represent the amplitude and sought phase, respectively.

1.1.1 Fringe Pattern Analysis

Fringe pattern analysis refers to the process of extracting phase from the fringe pattern. Broadly, the fringe analysis techniques can be categorized into *temporal* [14, 15] and *spatial* [16] fringe analysis techniques. In the former, a stack of phase-shifted fringe patterns are recorded over time as follows

$$\mathrm{I}_0(\mathrm{x},\mathrm{y}) = \mathrm{a}(\mathrm{x},\mathrm{y}) + \mathrm{b}(\mathrm{x},\mathrm{y})\cos[\phi(\mathrm{x},\mathrm{y}) + \delta_0], \tag{1.3}$$
$$\mathrm{I}_1(\mathrm{x},\mathrm{y}) = \mathrm{a}(\mathrm{x},\mathrm{y}) + \mathrm{b}(\mathrm{x},\mathrm{y})\cos[\phi(\mathrm{x},\mathrm{y}) + \delta_1], \tag{1.4}$$
$$\vdots \tag{1.5}$$
$$\mathrm{I}_\mathrm{N}(\mathrm{x},\mathrm{y}) = \mathrm{a}(\mathrm{x},\mathrm{y}) + \mathrm{b}(\mathrm{x},\mathrm{y})\cos[\phi(\mathrm{x},\mathrm{y}) + \delta_\mathrm{N}], \tag{1.6}$$

where, $\delta_0, \delta_1, \cdots, \delta_\mathrm{N}$ represent the phase shifts. Such phase shifts can be introduced into the one arm of the interferometer using different phase-shifting mechanisms [17]. The phase shifting interferometry (PSI) is the most widely used method for the phase estimation as it offers high measurement accuracy and resolution [18, 19]. The phase estimate at each pixel can be independently evaluated with at least three phase-shifted interferograms ($\mathrm{N} \geq 2$) based on the least-squares approach. The PSI usually requires high mechanical stability of the optical setup for the reliable phase estimation which is difficult to achieve in practice due to environmental disturbances such as vibrations, air turbulence, etc. In such scenarios, single fringe pattern based spatial analysis techniques are found to be more suitable. In the spatial fringe analysis techniques, spatial carrier fringe modulation is utilized to retrieve the phase from a single fringe pattern [9, 20]. The carrier fringes can be introduced into the interferometric setup by introducing an angle between the two interfering light beams. The carrier modulated fringe pattern can be expressed as follows

$$\mathrm{I}(\mathrm{x},\mathrm{y}) = \mathrm{a}(\mathrm{x},\mathrm{y}) + \mathrm{b}(\mathrm{x},\mathrm{y})\cos[\omega_\mathrm{x}\mathrm{x} + \omega_\mathrm{y}\mathrm{y} + \phi(\mathrm{x},\mathrm{y})]. \tag{1.7}$$

where ω_x and ω_y represent the carrier frequencies along x and y directions, respectively. The transform based techniques are commonly employed to derive the phase estimate from the carrier modulated fringe pattern.

Fringe pattern analysis is commonly assisted with pre-processing operations such as fringe pattern denoising and normalization. The fringe analysis techniques usually provide the phase estimate in a wrapped form. That is, the true values of phase estimate are wrapped

in the range $[-\pi, \pi]$. The phase unwrapping operation is performed for retrieval of the true phase values from the wrapped phase estimate. Sometimes, the phase estimate consists of unwanted phase contribution accumulated during the fringe recording along with the desirable phase component. Phase aberration compensation is performed for the removal of the unwanted component from the phase estimate.

1.2 Kalman filter

A number of discrete-time dynamic systems can be effectively represented by a state-space model. The state of the system is described by a finite set of variables. The Kalman filter (KF) is mainly used for the estimation of state variables of a dynamic system which are typically not directly measurable. It utilizes the mathematical model of system dynamics for predicting the state variables at the current time based on their estimate at previous time step and control inputs. These state variable estimates are further updated based on the measurements available at the current time. In doing so, the uncertainties in the state estimation and uncertainties in the measurements are taken into consideration.

In the context of fringe processing, the fringe intensity can be expressed as the function of background intensity, fringe amplitude, carrier frequency, phase, etc. Although the fringe intensity exhibits spatial sinusoidal variations, it is nonstationary in nature in a sense that its frequency varies depending on the pixel location. Therefore, Kalman filter renders itself well for the fringe pattern analysis by modeling the dynamics of spatial fringe intensity variations in the state-space formulation. The state variables can be defined in terms of background intensity, fringe amplitude, phase, etc. which evolve spatially with the dynamics governed by the fringe frequency. Accordingly, the measurement, i.e. fringe intensity, becomes function of state variables. Thus, the Kalman filter implemented in a pixel-wise manner allows to retrieve information on different components contributing to the fringe intensity.

The Kalman filter is a popular technique for the state estimation of discrete-time controlled process which can be described by linear stochastic difference equation as follows

$$\mathbf{s}_x = \mathbf{F}_x \mathbf{s}_{x-1} + \mathbf{G}_x \mathbf{u}_x + \mathbf{w}_x \tag{1.8}$$

where, $\mathbf{s}_x \in \mathbb{R}^n$ represents the n-dimensional state at the x-th discrete-time instance; $\mathbf{F}_x$ represents the $n \times n$ state-transition matrix; $\mathbf{G}_x$ represents the $n \times l$ matrix relating the state to the l dimensional input $\mathbf{u}_x$. The measurement of process variables represented by a m-dimensional vector $\mathbf{z}_x$ can be represented as a function of state as the following measurement equation

$$\mathbf{z}_x = \mathbf{H}_x \mathbf{s}_x + \mathbf{v}_x. \tag{1.9}$$

In equations (1.8) and (1.9), $\mathbf{w}_x = \mathcal{N}(0, \mathbf{Q}_x)$ and $\mathbf{v}_x = \mathcal{N}(0, \mathbf{R}_x)$ represent the process noise and measurement noise with covariances $\mathbf{Q}_x$ and $\mathbf{R}_x$, respectively. The measurement matrix $\mathbf{H}_x$ relates the state $\mathbf{s}_x$ to the measurement $\mathbf{z}_x$. The KF algorithm is described in the following

- **Initialization**: The state $\mathbf{s}_x$ and state estimation error covariance matrix $\mathbf{P}_x$ are initialized to random values or based on some prior information about the system as $\hat{\mathbf{s}}_0^+$ and $\hat{\mathbf{P}}_0^+$

- **Process Update**: At each time instance $x = 1, 2, \cdots$, the state and estimation error covariance matrix are updated based on the system dynamics described by Eq. (1.8) and their past values as follows

$$\hat{\mathbf{s}}_x^- = \mathbf{F}_x \hat{\mathbf{s}}_{x-1}^+ + \mathbf{G}_x \mathbf{u}_x, \tag{1.10}$$

$$\hat{\mathbf{P}}_x^- = \mathbf{F}_x \hat{\mathbf{P}}_{x-1}^+ \mathbf{F}_x^T + \mathbf{Q}_x. \tag{1.11}$$

- **Measurement Update**:- Once the measurement is available at the current time instance, the estimates of state and error covariance matrix evaluated in the previous step are updated as per the measurement update equation Eq. (1.9). It is assumed here that the measurement matrix $\mathbf{H}_x$ accurately represents the relationship between the state and measurements. The steps of measurement update are give below:

$$\mathbf{d}_x = \mathbf{z}_x - \mathbf{H}_x \hat{\mathbf{s}}_x^-, \tag{1.12}$$

$$\mathbf{K}_x = \hat{\mathbf{P}}_x^- \mathbf{H}_x^T (\mathbf{H}_x \hat{\mathbf{P}}_x^- \mathbf{H}_x^T + \mathbf{R}_x)^{-1}, \tag{1.13}$$

$$\hat{\mathbf{s}}_x^+ = \hat{\mathbf{s}}_x^- + \mathbf{K}_x \mathbf{d}_x, \tag{1.14}$$

$$\hat{\mathbf{P}}_x^+ = (\mathbf{I} - \mathbf{K}_x \mathbf{H}_x) \hat{\mathbf{P}}_x^-, \tag{1.15}$$

  where $\mathbf{K}_x$ represents the Kalman gain; $\mathbf{I}$ represents the $n \times n$ identity matrix.

The applicability of KF depends mainly on its user ability of representing the system under investigation in the state-space form. Consequently, the KF has been found in a wide range of applications such as computer vision systems [21, 22], navigation systems [23, 24], signal processing [25, 26], etc.

It is important to note that the Kalman filter is the optimal linear filter. The algorithm is defined for linear systems and the states, process and measurement noises are assumed to have Gaussian distribution. Therefore, after linear transformation, it maintains its Gaussian properties. However, in the case of nonlinear systems, the process update (Eq. (1.8)) and/or measurement update (Eq. (1.9)) may be nonlinear as shown below

$$\mathbf{s}_x = \mathrm{f}(\mathbf{s}_{x-1}) + \mathbf{w}_x, \tag{1.16}$$

$$\mathbf{z}_x = \mathrm{h}(\mathbf{s}_x) + \mathbf{b}\mathrm{v}_x \tag{1.17}$$

If the process update function f is nonlinear then the state distribution after transformation may not maintain its Gaussian properties and hence the algorithm may not converge towards to the true state. The same thing may occur if the measurements are nonlinear function of the states. In such situations, the extended Kalman filter (EKF) algorithm is used for state estimation which performs linearization of the nonlinear functions locally around the mean value of the current state estimate at each time instance. The Jacobian matrices are calculated and are used in the process and measurement update equations. Apart from the EKF, the unscented Kalman filter (UKF) [27–30] is also used for the state estimation especially in the case of highly nonlinear process and/or measurement update functions.

Chapter 2

Literature Review, Motivation and Objectives

As mentioned previously, the fringe processing involves pre-processing operations such as fringe denoising and fringe normalization prior to the phase demodulation. In addition, the post-processing operations of phase unwrapping and in some cases of phase aberration compensation are also important. Especially in the case of single fringe pattern some of these operations are imperative. In this chapter, we present a literature review on these fringe pattern analysis techniques. Based on the literature survey, the motivation of the thesis work has been provided. Accordingly, the thesis objectives are formulated and are presented below along with the thesis organization.

2.1 Fringe/Phase Pattern Denoising

2.1.1 Literature Review

In general, the fringe patterns are corrupted by multiplicative-type speckle noise caused due to the illumination of optically rough surface with coherent light source. The presence of speckle noise severely affects the phase extraction accuracy and reduces the quality of the fringe pattern. The performance of pre-processing operation of fringe denoising is crucial in deciding the phase estimation accuracy and effectively the measurement accuracy of physical parameters [31]. Consequently, a number denoising techniques have been developed over the years for *real fringe pattern* (or simply *fringe pattern*) and *phase fringe pattern* (or simply *phase pattern*). In the following, the principles of different fringe denoising techniques are discussed. The most simple type of denoising algorithm is based on moving average filter. It is a linear, low pass filter which replaces the intensity of each pixel by an average of pixel intensities within the window surrounding

that pixel. The cut-off frequency of the moving average filter is decided by the window size. The fixed window size results in spatially varying performance in fringe denoising [31]. A trade-off exists between the filtering performance and fringe blurring in selecting a window size. Selection of a small window causes minimal fringe distortion but poor noise filtering, whereas selection of a larger window provides effective noise filtering but undesirable fringe blurring. To overcome these limitations of moving average filter, spin filter based algorithms [32, 33] were reported. These algorithms utilize the fact that the maximum fringe intensity variation is observed along the direction perpendicular to the tangent to the fringe. On the other hand, fringe intensity variation is minimum in the direction tangential to the fringes. In spin filtering, the tangent directions to fringes are identified. As the fringe intensities in tangential direction are almost constant with variations caused only due to the noise, averaging along the tangential direction provide better denoising performance. Further, an improved spin filter algorithm had been proposed which is based on curved filtering windows. At first, a continuous fringe orientation map is computed by third order polynomial fitting of local fringe intensity. However, low pass filtering only along a curved line is not sufficient to remove the heavy speckle noise. Therefore, instead of using curved line window, curved surface window is used. As a number of iterations are required to achieve the acceptable filtering performance, the computation time associated with these methods are significantly high.

Another important method of fringe denoising is based on partial differential equations (PDE) [34, 35]. The PDE based denoising algorithms perform low pass filtering of fringe pattern based on the intensity diffusion to remove the noise. The speed of diffusion at the edges or boundaries of the fringe image is controlled to avoid the fringe deblurring. To further conserve the edge details during the process of filtering, anisotropic filtering process [36] is used. Similar to spin filtering algorithms, filtering is performed in the direction parallel to the fringes. The PDE based denoising algorithm reported in [37] considers the following second-order PDE wherein the intensity diffusion speed is controlled in the direction of the edges is performed based on the fringe regions. However, it results in an unwanted blocking effect. This limitation is overcome by the fourth-order PDE-based algorithm [38]. This method is also suitable for removing speckle noise from high-density fringe pattern.

A dimensionality reduction technique based on the singular value decomposition (SVD) has been reported [39] for fringe pattern denoising. Considering two-dimensional fringe image as a matrix, its rank is typically lower than the image dimension in the absence of noise. On the other hand, the rank becomes equal to the image dimension in the presence of noise. The SVD of the fringe image provides its decomposition into a number of constituent image components. The contribution of each of these image components is represented by its corresponding singular value. Due to the uniform distribution of the noise, the singular values associated with the noise components are lower in magnitude in comparison to the singular values corresponding to the noise-free image components. This fact has been utilized to obtain a noise-free estimate of the fringe image by utilizing the few dominant singular values with high magnitudes and their corresponding singular vectors.

Fringe denoising techniques such as the image decomposition method [40], non-local mean (NLM) based algorithms [41, 42], block-matching and 3D filtering (BM3D) denoising [43], etc have also been reported. The fundamental concept behind image decomposition methods [40] involves the decomposition of fringe patterns into low and high density components. Each component undergoes different filtering strategies by

constructing appropriate energy functions within their respective functional spaces. In NLM method, the weighted average of all the similar patches of the fringe pattern are calculated. Basically, this method is based on the concept of self similarity. The BM3D method uses non-local denoising technique by utilizing grouping and collaborative filtering. This method is similar to NLM technique. However, NLM is a spatial domain denoising technique, whereas BM3D is a transform domain denoising technique. The BM3D method effectively preserves the fine details and textures while performing denoising.

In the case of PSI and digital holographic interferometry, the measurement data is obtained in the form of the EPF given in Eq. (1.2). Since the phase information is of main importance, we consider the amplitude of the EPF be unity as

$$\mathrm{I(x,y)} = \exp[\mathrm{j}\phi(\mathrm{x},\mathrm{y})] \tag{2.1}$$

The complex-valued EPF is usually corrupted by phase noise which needs to be removed prior to phase unwrapping. However, due to the wrapping operation involved in the phase retrieval, there exist inherent 2π phase discontinuities in the wrapped phase. The conventional low-pass filtering of such phase results in smoothing these discontinuities along with the noise removal. Such a smoothing is detrimental to the subsequent phase unwrapping operation. Therefore, filtering of phase estimates in wrapped form is not recommended. Various techniques have been reported for phase denoising, such as sine-cosine average filter [44, 45], regularization methods [46, 47], least square method [48, 49], partial differential equations [50], windowed Fourier transform [51], localized Fourier transform [52], etc. In the sine-cosine moving-average filter method, the cosine and sine fringe images are obtained corresponding to the noisy wrapped phase. Since the continuous nature of these images, they are independently filtered based on the conventional low-pass moving average filter. Subsequently, the denoised phase estimate is obtained by inverse tangent of ratio of denoised sine and cosine images. This method mainly suitable only for slowly varying phase patterns. Its performance deteriorates for high-density phase patterns. This limitation is overcome by the anisotropic sine-cosine average filtering method [53] by selecting the window size based on the fringe density. The large window is selected in the direction of the low-density phase region, whereas the small window is selected in the direction of the high-density phase regions. However, the selection of window size depends on the prior knowledge of fringe density. The PDEs based methods such as second order oriented partial differential equation method [54], coupled non-linear oriented partial differential equation method [55] are proposed for phase pattern denoising. These methods require an estimate of fringe orientation for each pixel. However, it is difficult to calculate accurate fringe orientation with phase patterns consisting of high speckle noise. This eventually affect the denoising performance.

One of the most popular methods of phase pattern denoising are transform-based methods. The window Fourier filtering (WFF) method [51] is found to provide good denoising performance in a wide range of phase imaging applications. Its performance and computation time significantly depends on the selection of multiple user-defined parameters. Phase denoising method based on 2-D continuous wavelet transform [56] and monogenic wavelets transform [57] are reported which claim to preserve the edges details. In the localized Fourier filtering (LFF) method, the EPF is subdivided into overlapping patches due to which it fails to preserve the edges in the fringe pattern. A similar approach of patch-wise denoising based on the SVD has been proposed in [58]. The above mentioned

denoising utilize the conventional signal processing techniques involving user-defined algorithm parameters.

Due to the recent advancements in machine learning based algorithm, they have been employed for the real fringe and phase pattern denoising [59–62]. Deep learning techniques for fringe/phase denoising are typically based on a convolutional neural networks, which aims to learn an objective function by optimizing the cost function on a training data set. In Ref. [59] deep convolutional neural network model is trained by a set of fringe patterns with and without noise. After training the model, noisy fringe patterns are used as an input of the model and the denoised fringe patterns are predicted as the output of the trained model. A fringe denoising method based on residual dense convolutional neural network is proposed in Ref. [60] which utilized the U-net autoencoder. These methods are reported to provide good fringe denoising performance without user-defined parameters and in a computationally efficient manner. Wrapped phase denoising using CNNs [61] performs effective denoising, where the numerator (sine fringes) and the denominator (cosine fringes) of the arctangent function of the noisy phase pattern are denoised separately. This method provides good denoising results without adjusting the parameters for Gaussian noise but fails to process the speckle noise. An effective phase denoising technique based on a deep learning technique reported in Ref. [62] is shown to effectively filter the speckle noise from the wrapped phase without deteriorating the phase quality.

2.1.2 Motivation

The main aim of any fringe denoising technique is to remove the noise by preserving the details of the fringe/phase pattern. In the works on fringe denoising mentioned in the previous section, most of the methods are dependent on use defined parameters. In addition, they introduce fringe blurring during the noise removal especially at the fringe boundaries and fringe discontinuities. Although some of these algorithm provide satisfactory results, they come at the cost of high computation time. The major limitation of most of these algorithms is that their performance depends on the fringe density. Consequently, the optimal algorithm parameter selection becomes user-dependent based on the fringe pattern at hand. Although the deep leaning techniques are shown to provide good fringe denoising performance, it mainly depends on the large size training dataset. It may not provide good performance in all the scenarios. Considering these facts, it is important to develop a fringe denoising algorithm which can overcome these limitations and at the same time it should not be computationally intensive.

2.1.3 Objectives

Considering the limitations of the state-of-art fringe denoising techniques, the following research objectives are considered in the present thesis work.

Development of a fringe denoising technique providing the following features:

- Fringe density independent performance
- Ability to handle inherent fringe discontinuities

- Minimum loss of fringe signal (fringe blurring)
- Low computation time in comparison to state-of-art methods
- Ability to handle both additive and speckle noise with varying speckle sizes

2.2 Fringe Pattern Normalization

2.2.1 Literature Review

The typical fringe pattern represented by Eq. (1.1) is given below

$$I(x, y) = a(x, y) + b(x, y)\cos[\phi(x, y)]. \tag{2.2}$$

Since the information is encoded in the phase (ϕ) part for the fringe pattern, the background intensity and fringe amplitude represent the redundant information. The presence of these quantities affects the accuracy of phase estimation and are considered as source of error in phase estimation. Therefore, fringe normalization is a desirable preprocessing operation, especially for two frame phase shifting method or in the demodulation of closed fringe patterns. Normalized fringe pattern can also be used in another fringe processing operation such as fringe skeletonizing.

The background intensity and fringe amplitude variations occur due to the different optical components used while recording the data, uneven illumination of light sources, and the aberrant reflectivity of the test sample. Recently, various techniques have been reported in the literature for fringe pattern normalization. The orthogonal projection technique based method has been reported for fringe normalization [63]. In this method, two orthogonal bandpass filters are used to obtain the normalized fringe pattern. The performance of this method reduces with fringe pattern having stepped contrast variation and with low modulation region. Another method for fringe normalization is based on a quadrature operator using one-dimensional Reisz filters [64]. This method performs n-dimensional fringe pattern normalization based on n-dimensional quadrature transform. However, this method requires preprocessing the fringe pattern to remove the bias term. Various other methods for fringe normalization such as directional derivatives [65], adaptive monogenic filter [66], bi-dimensional empirical mode decomposition [67], and Zernike polynomial [68] method have been proposed. The method in Ref. [67] involves bias removal and data-driven technique for fringe pattern normalization based on the bi-dimensional empirical mode decomposition method and partial Hilbert transform method. This method is also suitable for the fringe pattern with stepped contrast variation and low modulation region. The Zernike polynomial [68] method for fringe normalization is based on Zernike polynomial fitting and local region contrast modulation. The main limitation is the algorithm is applicable for fringe pattern where the fringe data is available over a circular region.

2.2.2 Motivation

As mentioned previously, fringe pattern normalization is a desirable pre-processing step prior to phase demodulation. It is especially crucial in the closed fringe pattern phase

demodulation and two-frame based phase shifting techniques. However, the fringe normalization may result in the loss of essential fringe data which is not desirable. In the works of fringe normalization discussed in the previous section, most of the method requires bias suppression before normalization. Moreover, the inherent discontinuities in the interference data, background intensity and fringe amplitude may affect the fringe normalization. Considering these facts, it is important to develop a fringe normalization algorithm which can overcome these limitations.

2.2.3 Objectives

Considering the limitations of the state-of-art fringe normalization techniques, the following research objectives are considered in the present thesis work.

Development of a fringe normalization technique providing the following features:

- High fringe contrast
- Fringe density independent performance
- Applicability to both carrier modulated and closed fringe patterns

2.3 Fringe Pattern Demodulation

2.3.1 Literature Review

Once the fringe denoising and fringe normalization are performed, the most important operation of fringe demodulation needs to be performed for the phase estimation. A number of techniques have been reported over the years for fringe demodulation. These technique can be mainly classified into temporal and spatial fringe analysis technique. Temporal phase shifting [14, 15] is the most widely used method for phase extraction, wherein multiple phase shifted fringe patterns are recorded corresponding to a state of object under investigation. It offers high measurement accuracy and resolution, however it is not suitable for the measurement of dynamic events in real-time. Moreover, the measurements are typically sensitive to the environmental disturbances, such as vibrations. To enhance robustness against environmental noise, additional techniques for fringe demodulation [69–71] have been reported which involve acquisition of two random phase shifted fringe patterns. The phase difference between these patterns is subsequently utilized to extract the phase information. Whereas the demodulation technique in [69] must rely on fringe normalization for accurate phase estimation, the spatial phase shifting techniques in [70, 71] does not require fringe pattern normalization.

Spatial fringe analysis techniques are prominently used for the dynamic measurements as it involves a single recording of fringe pattern corresponding to a state of object under investigation. The most popular techniques are transform-based [17], for example, Fourier transform (FT)[72, 73] , windowed Fourier transform (WFT)[74, 75], wavelet transform (WVT)[76, 77], etc. The FT based method is the most commonly used due to its simplicity in implementation and the fast Fourier transform (FFT) routines available in many programming languages. Fringe signal is inherently non-stationary in nature,

whereas the FT is mainly suitable for stationary signal analysis. As a result, the local fringe frequency is an important parameter which is not provided by the FT-based fringe demodulation. The WFT is designed for the analysis of non-stationary signal wherein the FT transform is performed locally within a small window around each pixel. To do so, the WFT basis function is obtained by the multiplication of the Fourier basis function with a real-valued window function. The WFT performs the signal decomposition into a number of windowed Fourier basis functions. The localized signal analysis by the WFT provides the information of fringe frequency at each pixel. A number of algorithm parameters such as window size, frequency range, threshold, etc. need to be user-defined in the WFT-based method. The fixed-window size results in a constant space-frequency resolution. Similar to the WFT method, the WVT method is suitable for the non-stationary signal analysis. As opposed to the WFT, the WVT method involves adaptive selection of the window size which provided the optimal space-frequency resolution. Both one-dimensional and two-dimensional WVT methods have been reported for fringe pattern demodulation. In the WFT and WVT method, two phase estimation approaches can be considered.

- In the first, phase-based method, the best match of the complex-valued WFT/WVT basis with the fringe signal at each pixel is evaluated. The phase of the complex amplitude associated with the best-matched basis is considered to be the phase estimate at that pixel. The phase estimate obtained with the approach is in a wrapped form which requires subsequent phase unwrapping.
- In the second, phase gradient-based method, the frequency of the best matched WFT/WVT basis with the fringe signal at each pixel is estimated. This localized-frequency estimate can be considered to be the phase derivative. The integration of phase derivative provides the estimate of unwrapped phase.

The WVT phase-based method utilizes analytical mother wavelets for phase demodulation. Some examples of analytical mother wavelets[78] are B-spline, Gaussian, Paul, etc. The Fourier transform of the analytical mother wavelet have zero value for the negative frequency. The Paul wavelet is shown to provide the best time/space-localization and poorest frequency-localization in comparison with other mother wavelets at high signal-to-noise ratio (SNR). The Morlet wavelet perform reliable phase demodulation at low SNR in the case of slowly varying phase. In some applications, the phase derivative estimate obtained from the phase-gradient approach is of more significance. For example, in the surface deformation analysis using the ESPI, the phase is directly proportional to displacement, whereas phase derivative provides the information on displacement derivative, i.e. strain. The defect detection can be more clearly performed with the strain measurements. Therefore, the direct estimate of phase derivative can be useful in some applications. It is important to note that phase derivative estimate can also be obtained from the phase estimate using numerical differentiation. However, it has been observed that this operation provides noisy estimate of the phase derivative. Several other techniques for spatial fringe pattern analysis involves Hilbert transform (HT) method [79, 80], regularized phase tracking (RPT) [81, 82], variational image decomposition [83], etc. The HT based methods require fringe pattern pre-processing for the background intensity removal. In addition, the presence of noise have significant impact on the phase estimation accuracy in these methods. The regularized phase tracking methods [81] require a normalized fringe pattern for phase demodulation. However, this drawback is overcome by the generalized regularized phase tracking method [82] but

provides poor fringe demodulation in the area where the fringe data is sparse. The variational image decomposition based method [83] is found to provide better performance compared to the Fourier transform and wavelet transform based methods.

Most of the spatial fringe demodulation techniques involve the introduction of carrier fringes which are modulated by the phase information associated with the object under investigation. The carrier fringes allows for the sign unambiguous phase estimation. However, they reduce the dynamic range of the measurement. In order to achieve reliable phase estimate, the maximum spatial variation of the phase should be lower than the carrier frequency. Moreover, the maximum carrier frequency is limited by the spatial resolution of the digital sensor (CCD/CMOS). In order to achieve high dynamic range of measurement, closed fringe pattern demodulation techniques are used for the phase estimation. Some of the closed spatial fringe demodulation techniques for phase estimation are regularized phase tracking (RPT) [84–89], Hilbert transform (HT) method [90], local adaptive quadrature filter (LAQF) [91], frequency guided methods [92, 93], wavelet transform [94], phase-fitting with basis functions [95, 96], and Zernike-polynomial-based phase-fitting technique [97], etc. The RPT method is one of the effective methods for closed fringe demodulation. In this method, the estimated phase accuracy diminishes near the saddle points [84]. To further enhance this method, a fringe follower scanning technique has been introduced to avoid critical points [85]. However, it requires fringe pattern normalization prior to demodulation and is sensitive to noise. This limitation is overcome by the generalized regularized phase tracking (GRPT) [87] method. However, it fails to produce reliable phase estimates in the low fringe density regions. A two-dimensional HT method [90] transforms the demodulation problem into an orientation estimation problem. The LAQF method involves a quadrature filter applied locally around the a pixel within an analysis window. This method found to provide noise-robust phase estimate without fringe pattern normalization. Frequency guided method for closed fringe demodulation are based on a frequency guided scanning strategy to accurately identify the location of critical points. In this method, local frequency is estimated by using an optimisation technique which helps to determine the sign of the phase. A modified frequency guided method is proposed [92] to reduce the computation time complexity. In this method, the local frequency is estimated directly by calculating the gradient of the obtained phase with an undefined sign making the algorithm faster. Most of the above described methods for closed fringe demodulation are highly sensitive noise and have high time complexity. In the phase fitting with basis functions approach [95, 96], the phase in a given row or column is represented as a weighted linear combination of a certain number of linearly independent basis functions. Accurate weight estimation is performed to directly obtain the unwrapped phase estimate. Another important method for closed fringe demodulation is based on deep learning techniques [98, 99]. Deep learning methods for fringe demodulation have made significant progress in the past few decades. This is an optimization-based technique that is suitable for non-linear models. The closed fringe demodulation is typically a non-linear problem. In deep learning-based closed demodulation technique [98], when the actual data significantly differs from the data used in the supervised learning, then the estimated results are obtained with worse accuracy. The closed fringe demodulation by yuan [99] proposed an algorithm that provides high accuracy.

2.3.2 Motivation

The motivation of the thesis is to address some the following issues in the state-of-art fringe pattern demodulation techniques:

- The transform-based techniques require some prior knowledge of carrier frequency, fringe density, etc. for the reliable phase estimation from the carrier modulated fringe pattern. Such information may not be available in some scenarios.
- The phase estimation accuracy and computation time of these techniques depends significantly on the user-defined algorithm parameters.
- The phase estimation accuracy reduces at the fringe and/or image boundaries.
- The closed fringe demodulation techniques are sensitive to the noise. The presence of phase sign ambiguity results in erroneous unwrapped phase estimate.

2.3.3 Objectives

Considering the limitations of the state-of-art fringe demodulation techniques, the following research objectives are considered in the present thesis work.

Development of carrier and closed fringe demodulation techniques providing the following features:

- Carrier fringe demodulation
  - Minimum user-defined algorithm parameters
  - Phase estimation with high noise robustness and high accuracy (even at image boundaries)
  - Minimum or no requirement of fringe pre-processing
  - Low computation time in comparison to state-of-art methods
- Closed fringe demodulation
  - Phase estimation with high accuracy under the assumption of spatially continuous distribution
  - Devoid of local sign ambiguity

2.4 Phase Aberration Compensation

2.4.1 Literature Review

In quantitative phase imaging techniques such as digital holographic microscopy, the estimated phase may contain unwanted phase contribution apart from the object-related phase due to the imperfect optical components. For example, the microscope objective used in the microscopic setup for magnification introduces additional phase curvature in the measured phase. Such a contribution is usually termed as phase aberration. It

is essential to remove the phase aberration prior to translating the phase measurement into the associated physical quantity. As an example, the quantitative phase imaging of bio-specimen is utilized to derive the cell morphological parameters (volume, surface area, etc.) and statistical parameters (mean, entropy, standard deviation, etc.) from the phase measurement. These parameters are key in the cell-classification and disease identification.

Phase aberration compensation is an important post-processing algorithm to extract the phase contribution associated with the object under investigation from the measured phase. Various methods have been reported over the years for phase aberration compensation which can be broadly be categorized into physical methods [100–103] and numerical methods [104, 105].

In the physical method of aberration compensation, a reference phase is measured in addition to the object-related phase. The reference phase measurement needs to be performed with the same experimental setup parameters used during the object phase recording. However, such a reference phase measurement may not always be possible. Typically, the object-free area in the specimen is used to record the reference phase. However, finding such an area may be difficult especially in the case of densely populated objects such as cells or tissues. In addition, the behaviour of the aberration can be different in different region of interest which arises due to the sample itself.

On the other hand, numerical compensation methods can suppress the phase aberrations without any need for the reference phase. In these methods, the aberration component is modeled in functional forms such as parabolic functions [106, 107], standard polynomials [108, 109], spherical surface [110], and Zernike polynomials [111–113]. The amount of aberration described by the model parameters can be retrieved either with the spectral analysis [104, 114] or least square fitting [109, 110]. In spectral analysis technique, the phase aberration compensation accuracy is limited due to the sampling interval in the Fourier domain. The least-square fitting approach requires manual intervention in selecting the object-free region within the phase image. The phase aberration is estimation by deriving the model parameters associated with pre-defined functional forms. The principal component analysis technique [106] has also been employed. This technique assumes the presence of only spherical phase aberrations and linear phase tilt. Recently, the deep learning technique [113] has been utilized for aberration compensation which is found suitable for removing higher-order aberrations as well. However, extensive training dataset is required to achieve the required results. In additions, its application may be limited to specific sample type depending on the training dataset.

2.4.2 Motivation

The motivation of the thesis is to address some the following issues in the state-of-art phase aberration compensation techniques:

- The physical method for aberration compensation is not feasible in all practical scenarios.
- The numerical method may deteriorate the object-related phase component while removing the phase aberration component.

- In some scenarios, the specific functional forms may not accurately represent the phase aberration component. As a result, some phase residues may remain even after aberration compensation.
- In the case of deep learning techniques, the quantity and quality of available dataset play crucial role.

2.4.3 Objectives

Considering the limitations of the state-of-art for phase aberration compensation, the following research objectives are considered in the present thesis work.

Development of a phase aberration compensation technique with following features:

- Numerical aberration compensation without the reference phase
- Minimum loss of sought phase
- Generic model of aberration component of phase.

2.5 Thesis Organization

The thesis work is organized into eight chapters. The content of each chapter is briefly summarized in the following.

- **Chapter 1 Introduction**: This chapter introduces the concepts of interferogram/fringe pattern, importance of fringe pattern analysis and Kalman filter.
- **Chapter 2 Literature Review, Motivation and Objectives**: This chapter discusses some of the important state-of-art techniques reported in the literature for the fringe pattern analysis. Based on this survey, the motivation for the thesis work is described. Accordingly, the thesis objectives and expected results are defined.
- **Chapter 3 Fringe Pattern Denoising**: The first thesis objective of fringe pattern denoising is addressed in this chapter. The fringe denoising algorithms are proposed using the standard Kalman filter and adaptive Kalman filter. Similarly, the complex-valued fringe denoising algorithm is proposed based on the adaptive Kalman filter. The performances of these algorithms are evaluated using parameters such as peak signal-to-noise-ratio, speckle index, quality index, normalized mean square error and standard deviation. Both simulated and experimental results are provided to demonstrate the practical applicability of the proposed methods.
- **Chapter 4 Fringe Pattern Normalization**: In this Chapter, a new algorithm is proposed for the fringe normalization using a smoothing Kalman filter. The background intensity and the fringe amplitude are estimated consecutively in the proposed algorithm. These estimates are subsequently utilized to obtain the normalized fringe pattern. Simulation and experimental results validate the practical applicability of the proposed algorithm and its performance is appraised using quality index.

- **Chapter 5 Carrier Fringe Pattern Demodulation**: This chapter discusses third research objective of the thesis. Three algorithms are proposed for the carrier fringe pattern demodulation. In the first algorithm, the extended complex Kalman filter is used for the phase estimation which requires background intensity removal as a pre-processing step. An adaptive extended complex Kalman filter is considered in the second algorithm for the adaptive estimation of measurement noise covariance at each pixel to improve noise robustness. In the third algorithm, the background intensity is simultaneously estimated along with the quadrature signals which avoids the fringe pre-processing operation. Simulation and experimental examples are provided to substantiate the practical applicability of the proposed method.

- **Chapter 6 Closed Fringe Pattern Demodulation**: This chapter discusses an algorithm for closed fringe demodulation for an absolute phase estimation. In this work, the phase is represented as a weighted linear combination of a certain number of Zernike polynomials (ZPs). The ZP coefficient estimation is performed based on an extended Kalman filtering method. Here, a pseudo-measurement model is considered based on the state vector sparsity constraint to improve the convergence performance of the EKF. Simulation and experimental results validate the practical applicability of the proposed algorithm.

- **Chapter 7 Phase Aberration Compensation**: An unwanted phase with an object phase inherently affects the phase measurement accuracy. In this chapter, we will discuss an effective method for phase aberration compensation in digital holographic microscopy based on the Kalman filter. Aberration compensation can be performed by first scanning the phase image in a zigzag manner starting at its top left corner and later starting at its top right corner. Subsequently, the maximum of these two estimates is considered as the aberration component estimate. The practical ability of the proposed method are demonstrated using the simulation and experimental results.

- **Thesis Summary and Future Scope**: In the last chapter, thesis summary, the main contributions of the research work, and future scope of research work have been discussed.

Chapter 3

Fringe Pattern Denoising

The importance of fringe pattern denoising has been outlined in the Section 2.1.1. The main aim of any denoising technique is to remove the noise while preserving the details of the fringe pattern or phase pattern. In this chapter, the proposed *real fringe pattern* and *phase pattern* are reported.

3.1 Real Fringe Pattern Denoising

In general, the fringe patterns are corrupted by speckle noise because of use of the coherent light source in the interferometric measurement systems. This high frequency spatially varying noise is multiplicative in nature, that is, the strength of speckle noise varies with fringe density [115, 116]. The presence of speckle noise severely affects the phase extraction accuracy and reduces the quality of the fringe pattern by degrading fine fringe details [8]. Fringe denoising is essential and sometimes imperative preprocessing operation in the fringe analysis procedure [117]. It is of prime importance in the phase demodulation, especially from a single fringe pattern in speckle interferometry. In this chapter, a fringe speckle noise removal algorithm is proposed using the conventional Kalman filter (CKF) and adaptive Kalman filter (AKF). The CKF based fringe denoising is implemented with a constant user-defined process and measurement noise covariance matrices, whereas the AKF based implementation adaptively estimates the process and measurement noise covariance matrices.

3.1.1 Methodology

Let us consider a fringe pattern of size $\mathrm{L} \times \mathrm{K}$ as described in Eq. (1.1). The fringe signal in a given row y can be represented as

$$\mathrm{I(x)} = \mathrm{a(x)} + \mathrm{b(x)} \cos \phi(\mathrm{x}). \tag{3.1}$$

At first, we define a state space model to describe the spatial intensity variation. The process and the measurement equation given in Eq. (1.8) and Eq. (1.9), respectively, can be represented as

$$\mathbf{s}_\mathrm{x} = \mathbf{F}_\mathrm{x}\mathbf{s}_{\mathrm{x}-1} + \mathbf{w}_\mathrm{x}, \qquad \mathbf{w}_\mathrm{x} = \mathcal{N}(0, \mathbf{Q}_\mathrm{x}), \tag{3.2}$$

$$\mathbf{z}_\mathrm{x} = \mathbf{H}_\mathrm{x}\mathbf{s}_\mathrm{x} + \mathbf{v}_\mathrm{x}, \qquad \mathbf{v}_\mathrm{x} = \mathcal{N}(0, \mathbf{R}_\mathrm{x}). \tag{3.3}$$

where, $\mathbf{s}_\mathrm{x}$ represents the state variable at the xth step. The process and measurement updates of the state $\mathbf{s}_\mathrm{x}$ are governed by the state-transition matrix $\mathbf{F}_\mathrm{x}$ and observation-matrix $\mathbf{H}_\mathrm{x}$, respectively. $\mathbf{w}_\mathrm{x}$ and $\mathbf{v}_\mathrm{x}$ represent process noise and measurement noise with covariances $\mathbf{Q}_\mathrm{x}$ and $\mathbf{R}_\mathrm{x}$, respectively. In the present case, the state $\mathbf{s}_\mathrm{x}$ represents the estimate of the noise-free fringe intensity. The process Eq, (3.2) represents a random walk model for the fringe intensity driven by a random noise process with covariance $\mathbf{Q}_\mathrm{x}$ [118, 119]. $\mathbf{z}_\mathrm{x}$ represents the measured fringe intensity I(x) which is assumed to be corrupted by zero mean white Gaussian noise with covariance $\mathbf{R}_\mathrm{x}$. Accordingly, we set $\mathbf{F}_\mathrm{x} = 1$ and $\mathbf{H}_\mathrm{x} = 1$. The CKF-based and AKF-based procedures described in Algorithm 1 are implemented for all $\mathrm{y} = [0, \mathrm{L} - 1]$ to obtain two-dimensional denoised fringe pattern. The row-wise denoised fringe pattern is further denoised by implementing the above described procedure in a column-wise manner.

3.1.2 Results

Simulation

Two fringe patterns of size 400×400 pixels were simulated using a continuous and a discontinuous phase profiles as shown in Figs. 3.1(a) and 3.1(b), respectively. The

Algorithm 1 Fringe Denoising using Kalman filter

Conventional Kalman filter

1: The state and its error covariance matrix are initialized at $x = 0$ as

$\hat{\mathbf{s}}_0^+ = \mathbb{E}(\mathbf{s}_0)$,

$\mathbf{P}_0^+ = \mathbb{E}[(\mathbf{s}_0 - \hat{\mathbf{s}}_0^+)(\mathbf{s}_0 - \hat{\mathbf{s}}_0^+)^T]$,

where, $\mathbb{E}$ represents the expectation operator, the superscript $(\cdot)^+$ indicates the *a posterior* estimate and $\mathbf{P}$ is the state error covariance matrix. we set $\hat{\mathbf{s}}_0^+ = I(0)$ and $\mathbf{P}_0^+ = 10$.

2: For $x = 1, 2, \cdots$, the state and its error covariance matrix are predicted based on the process Eq. (3.2) as

$\hat{\mathbf{s}}_x^- = \mathbf{F}_x \hat{\mathbf{s}}_{x-1}^+$,

$\mathbf{P}_x^- = \mathbf{F}_x \mathbf{P}_{x-1}^+ \mathbf{F}_x^T + \mathbf{Q}_{x-1}$,

where, $(\cdot)^-$ represents *a priori* estimate.

3: The measurement update of the state and its error covariance matrices are computed as

$K_x = \mathbf{P}_x^- \mathbf{H}_x^T \left(\mathbf{H}_x \mathbf{P}_x^- \mathbf{H}_x^T + \mathbf{R}_x\right)^{-1}$,

$\hat{\mathbf{s}}_x^+ = \hat{\mathbf{s}}_x^- + K_x \left(\mathbf{z}_x - \mathbf{H}_x \hat{\mathbf{s}}_x^-\right)$,

$P_x^+ = \left(1 - K_x \mathbf{H}_x\right) P_x^- \left(1 - K_x \mathbf{H}_x\right)^T + K_x \mathbf{R}_x K_x^T$,

where, K_x represents the Kalman gain.

Adaptive Kalman filter

In order to estimate $\mathbf{Q}_x$ and $\mathbf{R}_x$ adaptively, two variables, innovation d_x and residual e_x, are defined as

$d_x = \mathbf{z}_x - \mathbf{H}_x \hat{\mathbf{s}}_x^-$,

$e_x = \mathbf{z}_x - \mathbf{H}_x \hat{\mathbf{s}}_x^+$,

Utilizing these terms, $\mathbf{Q}_x$ and $\mathbf{R}_x$ are estimated as [120]

$\mathbf{Q}_x = \alpha \mathbf{Q}_{x-1} + (1 - \alpha)\left(K_x d_x d_x^T K_x^T\right)$,

$\mathbf{R}_x = \alpha \mathbf{R}_{x-1} + (1 - \alpha)\left(e_x e_x^T + \mathbf{H}_x P_x^- \mathbf{H}_x^T\right)$,

Forgetting factor α is used in the computation of $\mathbf{Q}_x$ and $\mathbf{R}_x$ to assign appropriate weights to their previous estimates in the computation of their current estimates and we set $\alpha = 0.8$ in this algorithm. At $x = 0$, we need to select the initial values $\mathbf{Q}_0$ and $\mathbf{R}_0$ and we set the value of $\mathbf{R}_0 = 1$. The residual value e_x is required to evaluate the value of $\mathbf{R}_x$. However, the computation of e_x needs the estimate $\mathbf{s}_x^+$ which is not available at this stage of computation. Therefore, at first the value of e_x is set to zero and $\mathbf{R}_x$ is evaluated. Subsequently, K_x and $\mathbf{s}_x^+$ are evaluated. Thus, the estimate of $\mathbf{s}_x^+$ is available for the computation of residual e_x. Further, $\mathbf{R}_x$, K_x and $\mathbf{s}_x^+$ are reevaluated using e_x. These steps can be iterated for a given number of times.

RTS smoother algorithm

In order to achieve better fringe denoising performance, we propose to utilize a computationally efficient Rauch–Tung–Striebel (RTS) Kalman smoother algorithm [121]. In this algorithm, the forward and backward filtering is performed on a finite-sized signal to obtain improved filtering performance. The forward filtering for $\mathrm{x} = 1, 2, \cdots, \mathrm{K}-1$ is implemented using any one of the previously described Kalman filter algorithms. In the backward filtering, the RTS smoother algorithm is initialized at $\mathrm{x} = \mathrm{K}-1$ as

$$\hat{\mathbf{s}}^{(\mathrm{b})}_{\mathrm{K}-1} = \hat{\mathbf{s}}^{+}_{\mathrm{K}-1}, \qquad \mathbf{P}^{(\mathrm{b})}_{\mathrm{K}-1} = \mathbf{P}^{+}_{\mathrm{K}-1},$$

Following steps are implemented for $\mathrm{x} = \mathrm{K}-2, \cdots, 0$

$$\mathbf{G}^{(\mathrm{b})}_{\mathrm{x}} = \mathbf{P}^{+}_{\mathrm{x}} \mathbf{F}^{\mathrm{T}}_{\mathrm{x}+1} \left(\mathbf{P}^{-}_{\mathrm{x}+1}\right)^{-1},$$

$$\mathbf{P}^{(\mathrm{b})}_{\mathrm{x}} = \mathbf{P}^{+}_{\mathrm{x}} - \mathbf{G}^{(\mathrm{b})}_{\mathrm{x}} \left(\mathbf{P}^{-}_{\mathrm{x}+1} - \mathbf{P}^{(\mathrm{b})}_{\mathrm{x}+1}\right) \left(\mathbf{G}^{(\mathrm{b})}_{\mathrm{x}}\right)^{\mathrm{T}},$$

$$\hat{\mathbf{s}}^{(\mathrm{b})}_{\mathrm{x}} = \hat{\mathbf{s}}^{+}_{\mathrm{x}} + \mathbf{G}^{(\mathrm{b})}_{\mathrm{x}} \left(\hat{\mathbf{s}}^{(\mathrm{b})}_{\mathrm{x}+1} - \hat{\mathbf{s}}^{-}_{\mathrm{x}+1}\right).$$

Finally, the state $\hat{\mathbf{s}}^{(\mathrm{b})}_{\mathrm{x}}$ is considered to be denoised fringe intensity at the xth position.

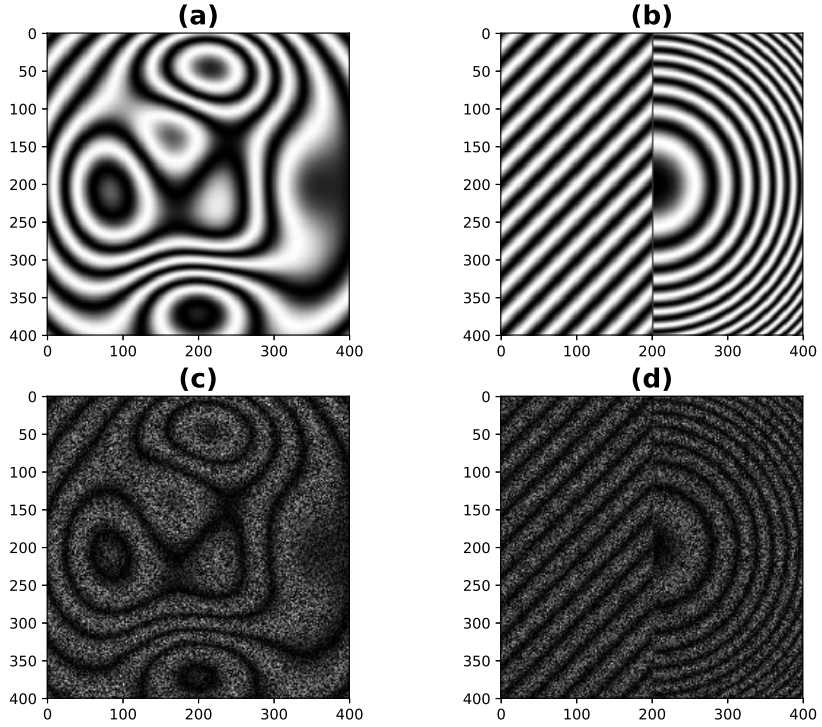

FIGURE 3.1: Simulated fringe patterns obtained using (a) continuous and (b) discontinuous phase profiles. (c) and (d) represent respective speckle noise corrupted fringe patterns [1].

corresponding speckle noise corrupted fringe patterns are shown in Figs. 3.1(c) and 3.1(d), respectively. For the purpose of evaluating denoising performance, the gray-scale intensity of fringe images are scaled between 0 and 1. The proposed CKF denoising method was applied to the simulated fringe patterns in Figs. 3.1(c) and 3.1(d). First

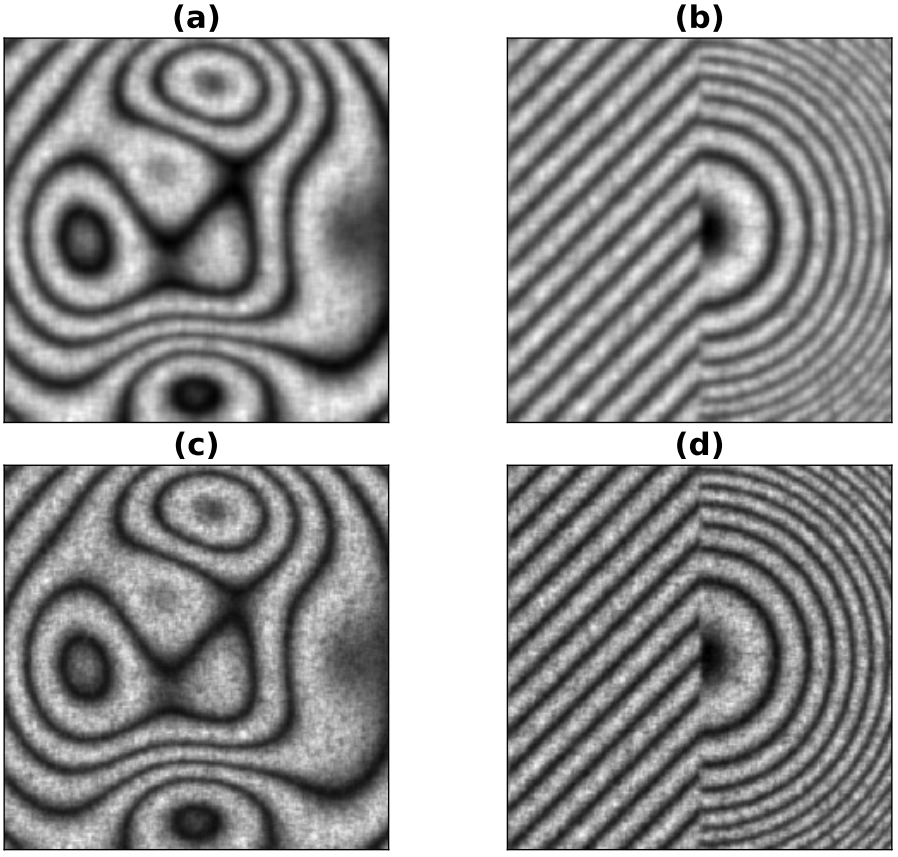

FIGURE 3.2: Denoised fringe pattern obtained on filtering fringe pattern shown in Figs. 3.1(c) and 3.1(d) using the CKF based method with (a), (b) $Q_x = 0.3$ and (c),(d) $Q_x = 0.6$, respectively [1].

and second row in Fig. 3.2 show the denoising results obtained with $\mathbf{Q}_x = 0.3$ and $\mathbf{Q}_x = 0.6$, respectively. It can be noted that low and high density fringes are effectively denoised with low and high $\mathbf{Q}_x$ values, respectively. It is because, in the region with low fringe density, the spatial variation in the fringe intensity is slower whereas, it is higher in the region with high fringe density. Figure 3.3 shows the denoising results for the same simulation example obtained using the proposed AKF, PDE [34], WFT [122] and DRT [123] methods.

Table 3.1 shows the algorithm parameters used in the implementation of fringe denoising algorithms. The proposed CKF and AKF methods are found to provide good denoising

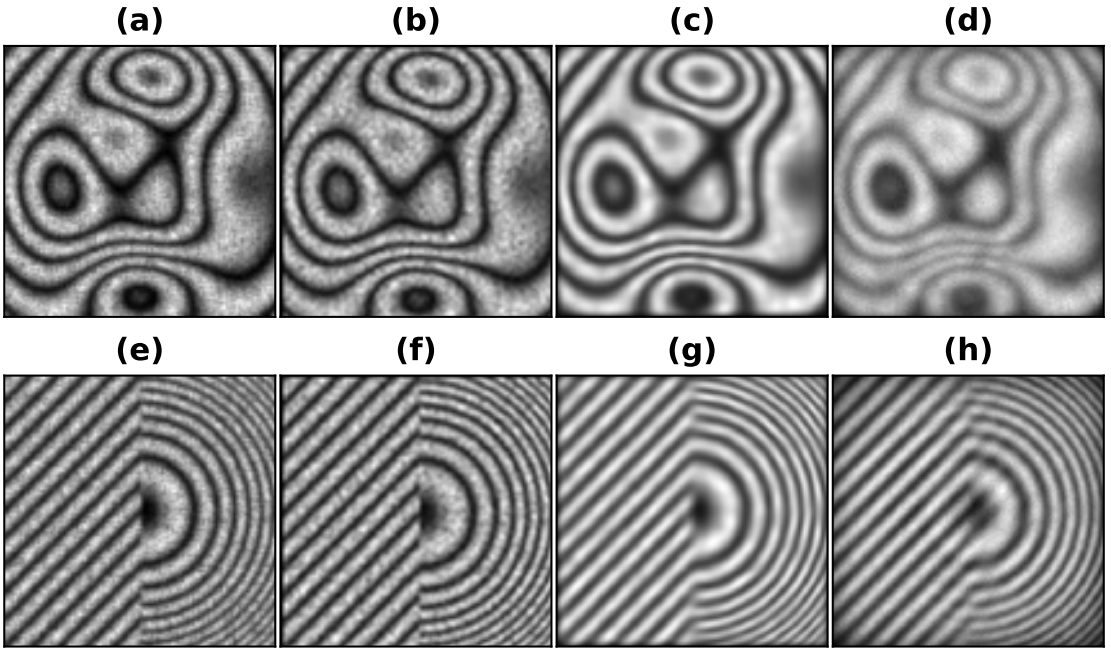

FIGURE 3.3: Denoised fringe patterns obtained on filtering the fringe pattern shown in Fig. 3.1(c) and 3.1(d) using (a),(e) AKF, (b),(f) PDE, (c),(g) WFT and (d),(h) DR [1]

.

performance. Especially, for the example in Fig. 3.1(d), the AKF method maintains the fringe discontinuity without blurring it, whereas the WFT method, although effective in fringe denoising, introduces blur at the fringe discontinuities and image boundaries. Figures 3.4(a) and (b) show the one-dimensional plot of denoised results obtained by using different methods at y = 220 of the fringe patterns shown in Figs. 3.1(c) and (d), respectively. It can be noted that the proposed method is suitable to denoise both the continuous and discontinuous type fringe patterns.

Quantitative comparison among fringe denoising algorithms is performed using two performance metrics, quality index [125] and peak signal-to-noise ratio [126]. The quality index (QI) can be described as below.

$$\mathrm{QI} = \frac{\sigma_{\mathrm{I}\tilde{\mathrm{I}}}}{\sigma_{\mathrm{I}}\sigma_{\tilde{\mathrm{I}}}} \frac{2\mu_{\mathrm{I}}\mu_{\tilde{\mathrm{I}}}}{\mu_{\mathrm{I}}^2 + \mu_{\tilde{\mathrm{I}}}^2} \frac{2\sigma_{\mathrm{I}}\sigma_{\tilde{\mathrm{I}}}}{\sigma_{\mathrm{I}}^2 + \sigma_{\tilde{\mathrm{I}}}^2}, \tag{3.4}$$

where, I and $\tilde{\mathrm{I}}$ represent noise-free and denoised fringe patterns, respectively; $\mu_{\mathrm{I}}, \mu_{\tilde{\mathrm{I}}}$ and $\sigma_{\mathrm{I}}, \sigma_{\tilde{\mathrm{I}}}$ represent the mean and variance of I and $\tilde{\mathrm{I}}$, respectively; $\sigma_{\mathrm{I}\tilde{\mathrm{I}}}$ represents co-variance

TABLE 3.1: Fringe denoising algorithm parameters used in obtaining simulation and experimental results.

Methods	**Fringe Pattern**	**Algorithm parameters**
CKF	Fig. 3.2(a),(b)	$\mathbf{Q}_x = 0.3, \mathbf{R} = 1.$
	Fig. 3.2(c),(d)	$\mathbf{Q}_x = 0.6, \mathbf{R} = 1.$
	Fig. 3.6(a),(b)	$\mathbf{Q}_x = 0.08, \mathbf{R} = 1.$
	Fig. 3.6(c),(d)	$\mathbf{Q}_x = 0.2, \mathbf{R} = 1.$
AKF	Fig. 3.3(a),(e)	$\mathbf{Q}_0 = 0.2, \mathbf{R}_0 = 1, \alpha = 0.8.$
	Fig. 3.7(a),(e)	$\mathbf{Q}_0 = 0.01, \mathbf{R}_0 = 1, \alpha = 0.8.$
PDE[34]	Fig. 3.3(b),(f)	iterations=100, k = 10^{-5}, Δt = 0.02.
	Fig. 3.7(b),(f)	iterations=100, k = 10^{-5}, Δt = 0.02.
WFT[124]	Fig. 3.3(c),(g)	u=[-0.5,0.5], v= [-0.5,0.5], du=0.1, dv=0.1, Thr = 1.
	Fig. 3.7(c),(g)	u=[-0.5,0.5], v= [-0.5,0.5], du=0.1, dv=0.1, Thr = 1.
DR[123]	Fig. 3.3(d),(h)	number of rotation=25, dimension=5.
	Fig. 3.7(d),(h)	number of rotation=35, dimension=5.

between I and $\tilde{\text{I}}$. The dynamic range of QI is [–1, 1], where –1 and 1 corresponds to lowest and highest similarity among two fringe patterns, respectively. The peak signal-to-noise ratio (PSNR) can be described as below.

$$\text{PSNR} = 10 \log \frac{\text{A}^2}{\text{MSE}}, \tag{3.5}$$

where A stands for the maximum possible pixel intensity in a fringe pattern which is equal to $2^{\text{p}} - 1$ with p as the pixel depth. The mean square error (MSE) is defined as

$$\text{MSE} = \frac{1}{\text{KL}} \sum_{\text{x}=0}^{\text{K}-1} \sum_{\text{y}=0}^{\text{L}-1} \left(\text{I}(\text{x}, \text{y}) - \tilde{\text{I}}(\text{x}, \text{y})\right)^2. \tag{3.6}$$

Thus, MSE represents the difference of intensities between the noise-free and denoised fringe patterns. The PSNR is a ratio of maximum possible power of the noise-free fringe pattern to the power of fidelity noise. High value of PSNR represents high denoising performance.

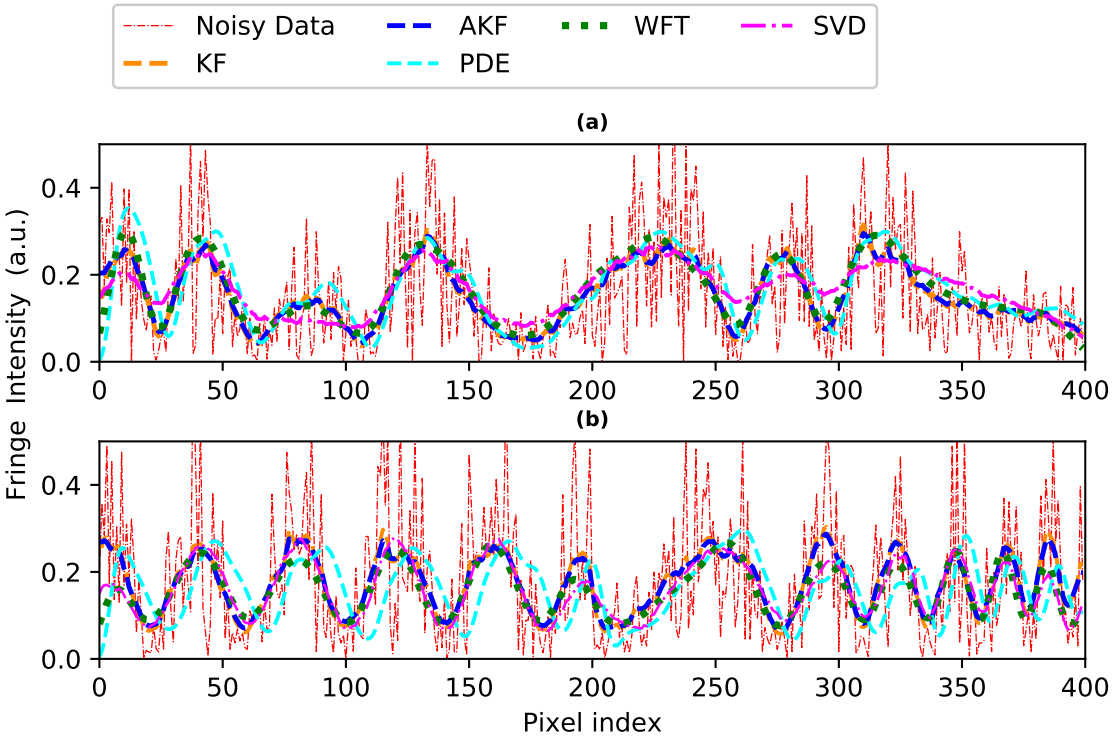

FIGURE 3.4: Denoising results obtained using different methods in row y = 220 of fringe pattern shown in (a) Fig. 3.1(c) and (b) Fig. 3.1(d) [1].

Table 3.2 shows the performance metrics evaluated for the results shown in Fig. 3.2 and Fig. 3.3. It can be noted from the results given in table 3.2 that the CKF method provides good denoising performance at low and high value of $\mathbf{Q}_x$ in the case of low and high density fringe patterns, respectively. On the other hand, the AKF method provides good performance for fringe patterns with arbitrary density since it estimates the value of $\mathbf{Q}_x$ and $\mathbf{R}_x$ at each pixel in an adaptive manner. It can be noted that the proposed CKF and AKF provide better denoising performance compared to other methods.

Experiment

The experimental validation of the proposed method is performed using the fringe patterns recorded in a classical phase shifting holographic interferometry (Fig. 3.5(a)) and electronic speckle pattern interferometry (Fig. 3.5(b)) setups. The fringe patterns in Figs. 3.5(a) and 3.5(b) are of sizes 560×560 and 930×930 pixels corresponding to out-of-plane and in-plane displacement of an aluminium plate, respectively. These fringe patterns were denoised using the proposed CKF method with $\mathbf{Q}_x = 0.08$ and $\mathbf{Q}_x = 0.2$

TABLE 3.2: Quality index (QI) and peak signal-to-noise-ratio (PSNR) (in dB) values evaluated for denoised fringe patterns shown in Figs. 3.2 and 3.3. Speckle index (SI) values evaluated for denoised fringe patterns shown in Figs. 3.6 and 3.7.

Fringe pattern	**Denoising Methods**					
	CKF		**AKF**	**PDE**	**WFT**	**DR**
	$\mathbf{Q}_x = 0.3$	$\mathbf{Q}_x = 0.6$	$\mathbf{Q}_0 = 0.2$			
	QI					
Fig. 3.1(c)	**0.80**	0.79	**0.83**	0.73	0.78	0.70
Fig. 3.1(d)	0.78	**0.84**	**0.835**	0.63	0.78	0.78
	PSNR (in dB)					
Fig. 3.1(c)	**38.5**	30.06	**38.47**	29.02	37.13	27.37
Fig. 3.1(d)	31.94	**33.22**	**33.73**	21.23	32.05	30.80
	SI($\times 10^{-3}$)					
	$\mathbf{Q}_x = 0.08$	$\mathbf{Q}_x = 0.2$	$\mathbf{Q}_0 = 0.01$			
Fig. 3.5(a)	**0.4**	0.91	**0.5**	1.73	1.43	0.69
Fig. 3.5(b)	**0.85**	1.36	**1.0**	2.52	1.48	1.41

and the results are shown in Fig. 3.6. The denoised fringe patterns obtained using the proposed AKF, PDE, WFT and DRT algorithms are shown in Fig. 3.7. The algorithm paramaters are given in Table 3.1. As the ground truth noise-free fringe patterns are not available for quantitative performance evaluation in the case of experimental fringe patterns, we have used speckle index (SI) [127] as the performance metric. It is defined as

$$\mathrm{SI} = \frac{1}{\mathrm{KL}} \sum \frac{\sigma_{\tilde{\mathrm{I}}}(\mathrm{x},\mathrm{y})}{\mu_{\tilde{\mathrm{I}}}(\mathrm{x},\mathrm{y})}, \tag{3.7}$$

where $\mu_{\tilde{\mathrm{I}}}(\mathrm{x},\mathrm{y})$ and $\sigma_{\tilde{\mathrm{I}}}(\mathrm{x},\mathrm{y})$ represent mean and standard deviation of denoised fringe intensity computed within 5×5 sized window around each pixel. A low value of SI indicates high noise suppression. The values of SI obtained for the fringe denoising results in Figs. 3.6 and 3.7 are given in Table 3.2. Although the value of SI is low for the CKF algorithm with $\mathbf{Q}_x = 0.08$, the excessive filtering resulted in blurring of the fringe pattern in Fig. 3.6(a). It can be noted that the proposed algorithm provided better

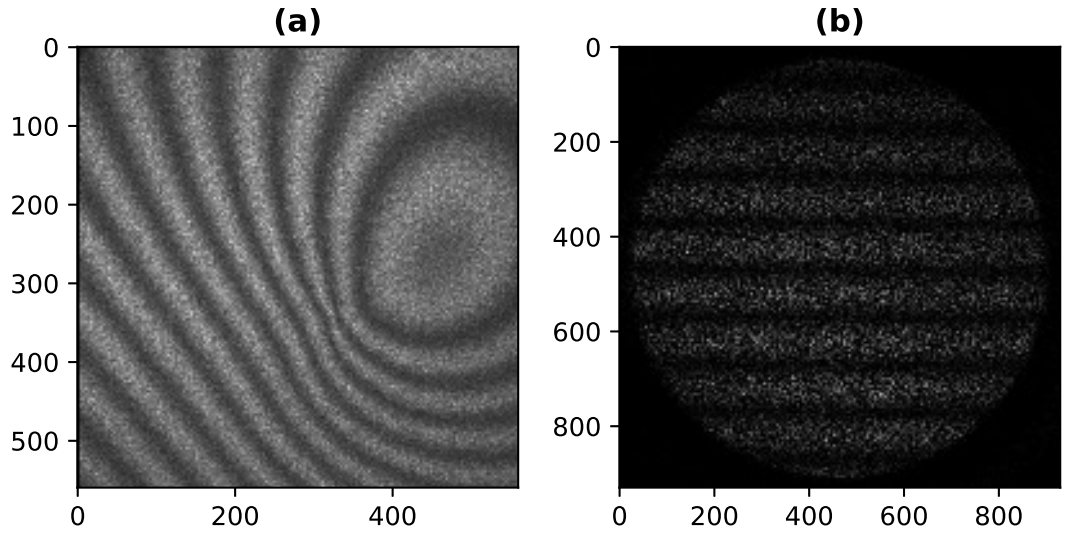

FIGURE 3.5: Experimentally recorded fringe patterns in (a) a classical holographic interferometric setup corresponding to out-of-plane displacement of an aluminum plate and in (b) an ESPI setup for measuring in-plane displacement of an aluminum plate [1].

denoising performance compared to other methods.

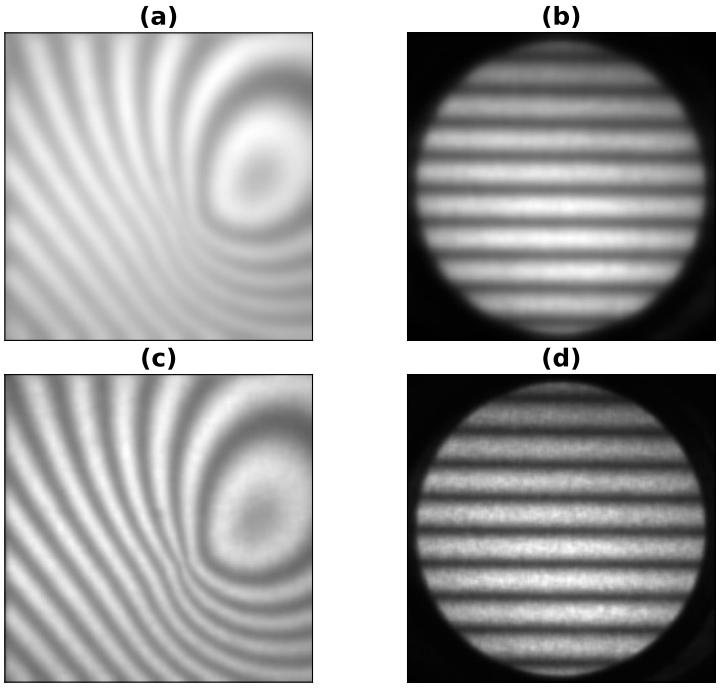

FIGURE 3.6: Denoised fringe patterns obtained on filtering the fringe pattern shown in Fig. 3.5 using CKF with (a,b) $\mathbf{Q}_x = 0.08$ and (c,d) $\mathbf{Q}_x = 0.2$ [1].

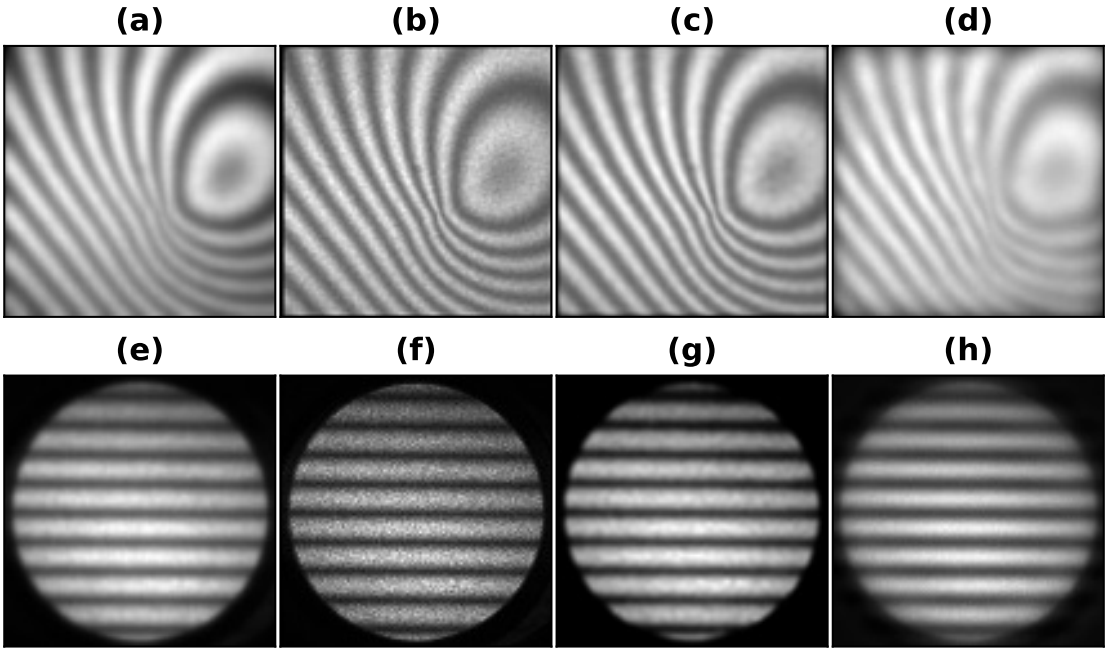

FIGURE 3.7: Denoised fringe patterns obtained on filtering the fringe pattern shown in Fig. 3.5 using (a,e) AKF, (b,f) PDE, (c,g) WFT and (d,h) DR [1].

3.1.3 Discussion and Conclusion

A robust method for fringe denoising using the conventional and adaptive Kalman filter is described in this chapter. Kalman filter implementation involves empirical selection of process modeling error and measurement error covariance matrices, $\mathbf{Q}_x$ and $\mathbf{R}_x$, respectively. Similarly in the proposed method of fringe denoising based on conventional Kalman filter, a proper selection of values of $\mathbf{Q}_x$ and $\mathbf{R}_x$ is essential at each pixel location. The value of $\mathbf{Q}_x$ is chosen based on fringe density. Accordingly, a modified Kalman filtering technique is used in the proposed method which involves adaptive evaluation of the values of $\mathbf{Q}_x$ and $\mathbf{R}_x$ at each pixel. This feature allows to preserve the details and discontinuities of fringe patterns in the process of denoising. The initial values of $\mathbf{Q}_0$ and $\mathbf{R}_0$ need to be set at the first pixel. The values of $\mathbf{Q}_0$ depend on the size of fringe pattern. For large size fringe pattern, a lower value of $\mathbf{Q}_0$ should be selected and vice versa. The proper selection of $\mathbf{Q}_x$ helps to balance noise suppression with the preservation of fringe pattern features. On the other hand, $\mathbf{R}_x$ determines the relation between observed measurements and the state prediction. Optimizing the value of $\mathbf{R}_x$ ensures

accurate estimation of fringe patterns while minimizing estimation errors.

Additional parameters, such as the forgetting factor (α) controls the influence of past observations on the current state estimate, which facilitates adaptability to varying noise levels encountered during fringe pattern acquisition. The value of α can be selected in the range $[0, 1]$. A large value of α puts more weight on the previous state estimate. Accordingly, for the purpose of fringe denoising, the value of α is set to 0.8. Simulation and experimental results indicated that the proposed method provides better denoising performance in comparison with some of the existing methods.

3.2 Complex Fringe Pattern Denoising

As mentioned in the previous section, the complex fringe pattern or wrapped phase is obtained in the setups such as PSI and digital holographic interferometry. The reliability of the subsequent phase unwrapping [51, 128, 129] depends heavily on the quality of the phase pattern. The speckle noise in the wrapped phase makes phase unwrapping a difficult task and may lead to inaccuracy. Hence, it is required to filter the phase pattern. However, at the same time, it is important to maintain the 2π phase discontinuity associated with the wrapped phase intact after denoising. Therefore, the main aim of any denoising technique is to remove the noise by preserving the details of the phase pattern. A wrapped phase denoising algorithm is developed based on the adaptive Kalman filtering method. The exponential phase field (EPF) corresponding to the phase pattern given in Eq. (1.2) is again provided below

$$\mathrm{I}(\mathrm{x}, \mathrm{y}) = \exp[\mathrm{j}\phi(\mathrm{x}, \mathrm{y})], \tag{3.8}$$

where, $\mathrm{I}(\mathrm{x}, \mathrm{y})$ represent complex interference field; $\mathrm{j} = \sqrt{-1}$; $\mathrm{x} \in [0, \mathrm{K}-1]$ and $\mathrm{y} \in [0, \mathrm{L}-1]$ represent pixels along rows and column respectively; $\phi(\mathrm{x}, \mathrm{y})$ is the phase.

3.2.1 Methodology

The EPF in a given row y can be expressed as

$$\mathrm{I(x)} = \exp[\mathrm{j}\phi(\mathrm{x})]. \tag{3.9}$$

The denoised EPF can be expressed as

$$\hat{\mathrm{I}}(\mathrm{x}) = \exp[\mathrm{j}\hat{\phi}(\mathrm{x})]. \tag{3.10}$$

The denoised wrapped phase $\hat{\phi}(\mathrm{x})$ can be calculated as

$$\hat{\phi}(\mathrm{x}) = \angle\hat{\mathrm{I}}(\mathrm{x}). \tag{3.11}$$

In the Kalman filter implementation for phase denoising, a state space model can be described as follows

$$\mathbf{s}_\mathrm{x} = \mathrm{F}_\mathrm{x}\mathbf{s}_{\mathrm{x}-1} + \mathbf{w}_\mathrm{x}, \qquad \mathbf{w}_\mathrm{x} = \mathcal{N}(0, \mathbf{Q}_\mathrm{x}). \tag{3.12}$$

$$\mathbf{z}_\mathrm{x} = \mathrm{H}_\mathrm{x}\mathbf{s}_\mathrm{x} + \mathbf{v}_\mathrm{x}, \qquad \mathbf{v}_\mathrm{x} = \mathcal{N}(0, \mathbf{R}_\mathrm{x}). \tag{3.13}$$

where, $\mathbf{s}_\mathrm{x}$ represents the state vector, which in this case is the estimate of $\hat{\mathrm{I}}(\mathrm{x})$; $\mathbf{F}_\mathrm{x}$ represents state transition matrix; the system modeling noise $\mathbf{w}_\mathrm{x}$ is considered to be of white Gaussian type with zero mean and covariance $\mathbf{Q}_\mathrm{x}$; The measurement vector $\mathbf{z}_\mathrm{x}$ consists of the noisy EPF measurement I(x). The measurement matrix and measurement noise are represented with $\mathbf{H}_\mathrm{x}$ and $\mathbf{v}_\mathrm{x}$, respectively. The measurement noise is considered to be of white Gaussian type with zero mean and covariance $\mathbf{R}_\mathrm{x}$. As indicated in Eq. (3.12), the spatial variation of phase is considered to be stochastic in nature governed by the covariance matrix $\mathbf{Q}_\mathrm{x}$. Since the state estimation is performed for the purpose of denoising, $\mathbf{F}_\mathrm{x}$ and $\mathbf{H}_\mathrm{x}$ are considered to be identity matrices. The phase denoising can be performed in multiple rows simultaneously by considering a state vector $\mathbf{s}_\mathrm{x}$ of size $\mathrm{D} \times 1$ consisting of $\hat{\mathrm{I}}(\mathrm{x})$ as its elements for D rows. Accordingly, $\mathbf{z}_\mathrm{x}$ becomes a vector of size $\mathrm{D} \times 1$ consisting of I(x) as its elements from the same rows; $\mathbf{F}_\mathrm{x}$ and $\mathbf{H}_\mathrm{x}$ are identity matrices of size $\mathrm{D} \times \mathrm{D}$; and $\mathbf{Q}_\mathrm{x}$ and $\mathbf{R}_\mathrm{x}$ are $\mathrm{D} \times \mathrm{D}$ sized diagonal matrices. In general,

for implementing the Kalman filter, fixed values of Q_x and D_x are selected empirically depending on the application. In the case of wrapped phase denoising, the value of $\mathbf{Q}_x$ and $\mathbf{R}_x$ should be chosen depending on the fringe density and phase noise, respectively. We propose to utilize the algorithm described in Ref. [130] for the adaptive estimation of $\mathbf{Q}_x$ and $\mathbf{R}_x$. Even though the initial values of $\mathbf{Q}_x$ and $\mathbf{R}_x$ need to be set at $x = 0$, the AKF is found to be less sensitive to the selection of these values.

The steps involved in the row-wise phase denoising have been described in Algorithm 2 and the same procedure is repeated for each column in the same manner. The time complexity of the proposed algorithm is reduced by increasing the value of D in the algorithm.

3.2.2 Results

Simulation

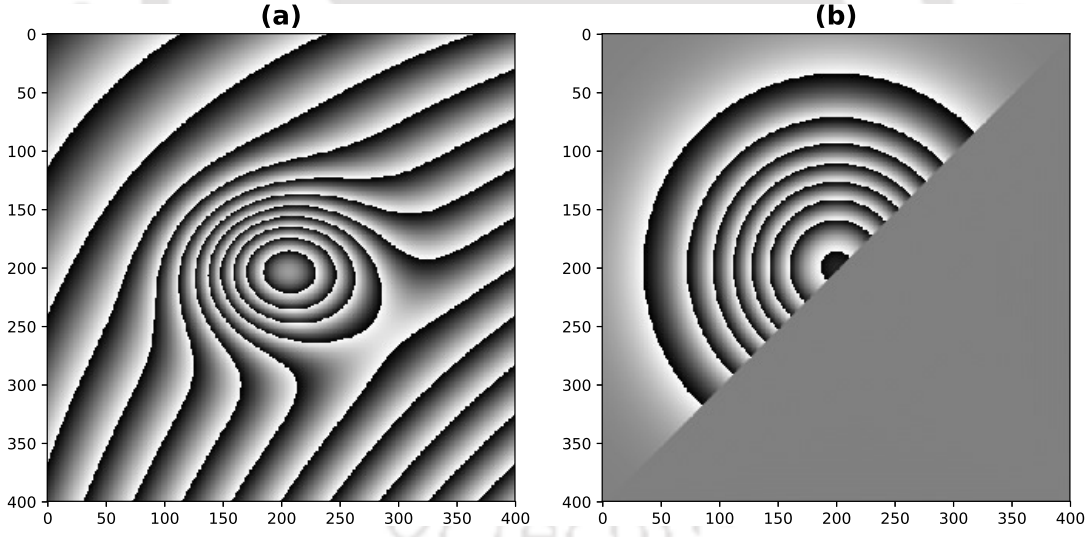

FIGURE 3.8: Simulated wrapped phase patterns associated with (a) continuous and (b) discontinuous absolute phase [2].

Figures 3.8(a) and 3.8(b) show the simulated wrapped phase fringe patterns of size 400×400 pixels. The wrapped phase patterns in Figs. 3.8(a) and 3.8(b) correspond to continuous and discontinuous absolute phase distributions, respectively. Considering the phase example in Fig. 3.8(a), speckle noise corrupted wrapped phase patterns were simulated as shown in Figs. 3.9(a), 3.9(b), and 3.9(c) corresponding to the speckle sizes

Algorithm 2 Denoising using adaptive Kalman filter

1: The initial guess of state and its error covariance at $x = 0$ are represented as

$\mathbf{s}_0^+ = \mathbb{E}(\mathbf{s}_0)$,

$P_0^+ = \mathbb{E}[(\mathbf{s}_0 - \mathbf{s}_0^+)(\mathbf{s}_0 - \mathbf{s}_0^+)^T]$,

where $\mathbb{E}(\cdot)$ represents the expected value. In the proposed method, we set all the elements of $\mathbf{s}_0^+$ equal to $1 + 1j$; the value of $D = 1, 2, \cdots, K-1$ and for quicker convergence, the value of P_0^+ is set to be $10I_D$, where I_D represents identity matrix of $D \times D$.

2: The predicted state estimation and its covariance at $x = 1, 2, 3.....$ are found using the Eq.. (3.12) as

$\mathbf{s}_x^- = \mathbf{F}_x \mathbf{s}_{x-1}^+$,

$P_x^- = \mathbf{F}_x P_{x-1}^+ \mathbf{F}_x^T + \mathbf{Q}_{x-1}$,

The subscript $(\cdot)^+$ and $(\cdot)^-$ indicate the posterior and prior estimates, respectively.

3: The prior estimates are used to compare the actual measurement with the predicted state measurement and the difference are corrected by using posterior estimate as

$g_x = \mathbf{z}_x - \mathbf{H}_x \mathbf{s}_x^-$,

$\mathbf{s}_x^+ = \mathbf{s}_x^- + K_x g_x$,

$c_x = \mathbf{z}_x - \mathbf{H}_x \mathbf{s}_x^+$,

$\mathbf{R}_x = \alpha \mathbf{R}_{x-1} + (1-\alpha)\left(c_x \bar{c}_x^T \mathbf{H}_x P_x^- \mathbf{H}_x^T\right)$,

$K_x = P_x^- \mathbf{H}_x^T [\mathbf{H}_x P_x^- \mathbf{H}_x^T + \mathbf{R}_x]^{-1}$,

$P_x^+ = (I_D - K_x \mathbf{H}_x) P_x^-$,

$\mathbf{Q}_x = \alpha \mathbf{Q}_{x-1} + (1-\alpha)\left(K_x g_x \bar{g}_x^T K_x^T\right)$,

where $\mathbf{K}_x$, $\bar{c}_x^T$, and $\bar{g}_x^T$ represent the Kalman gain, transpose of residual and and innovation, respectively. $\mathbf{F}_x$ and $\mathbf{H}_x$ are $(D \times D)$ sized identity matrix. $\mathbf{P}_x$, $\mathbf{Q}_x$, and $\mathbf{R}_x$ are defined as $(D \times D)$ sized matrix. The initial value of $\mathbf{Q}_x$ and $\mathbf{R}_x$ at $x = 0$ need to be selected. Subsequent values of $\mathbf{Q}_x$ and $\mathbf{R}_x$ are estimated and updated adaptively during each update. The initial value of α and $\mathbf{R}_0$ are set to be 0.8 and 1, respectively. In general, the α value varies in the range $[0, 1]$ and a high α value gives more weight to the previous state estimate.

4: Rauch–Tung–Striebel (RTS) smoother algorithm is used for effective denoising which has been described in Algorithm 1.

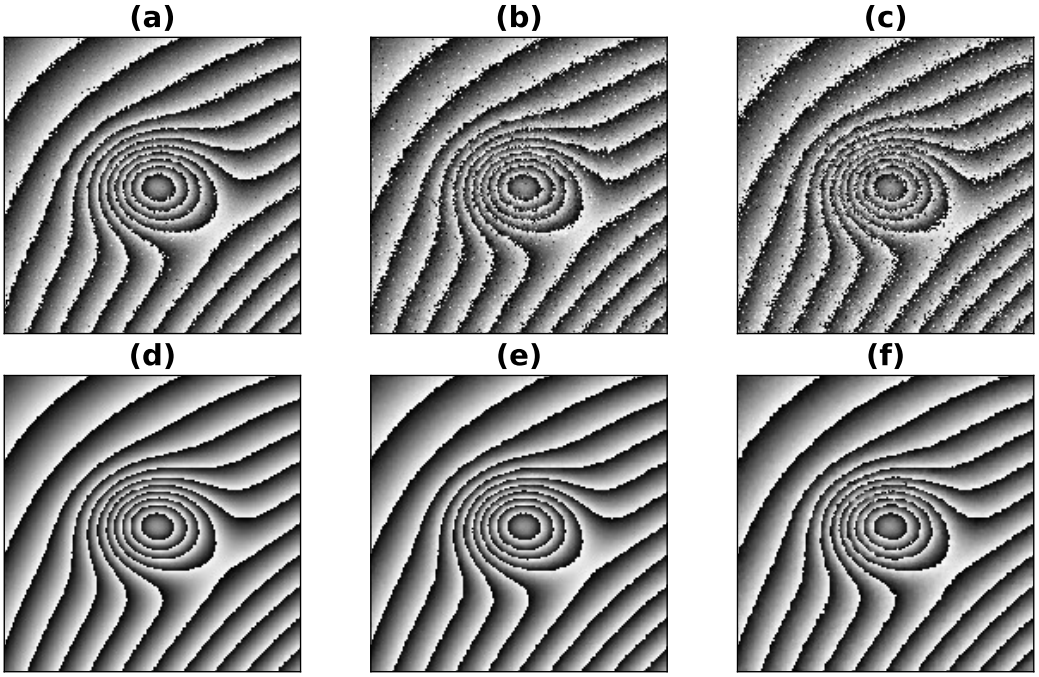

FIGURE 3.9: Simulated wrapped phase pattern corrupted by speckle decorrelation noise with speckle size of (a) 1, (b) 1.5, and (c) 2 pixels. (d),(e), and (f) Denoised phase patterns obtained using AKF with $\mathbf{Q}_0 = 0.5$ [2].

of 1, 1.5, and 2, respectively. It is quite evident from these phase patterns that high-density fringe regions are more corrupted with noise in comparison to low fringe density regions due to multiplicative nature of the speckle noise. The speckle noise simulation was performed based on the procedure described in Ref. [131]. The AKF denoising algorithm was implemented with $\mathbf{Q}_0 = 0.5$ to obtain the denoised wrapped phases shown in Figs. 3.9(d), 3.9(e), and 3.9(f). The results indicate that the AKF is capable of providing good denoising performance for different speckle sizes.

As mentioned previously, the performance of Kalman filter based denoising depends on the selection of values of system noise covariance ($\mathbf{Q}_x$). A small change in the value of $\mathbf{Q}_x$ may cause significant change in the denoising performance. The adaptive estimation of system and measurement noise covariances allows the AKF to provide good denoising performance independent of the manual adjustment of algorithm parameters. In addition, the AKF allows simultaneous processing of multiple rows to reduce the computational cost of the implementation without significant change in the denoising performance. Figure 3.10 shows the denoised results obtained for the noisy wrapped phase shown in Fig. 3.9(c) using the AKF for different values of D and $\mathbf{Q}_0$. It can be

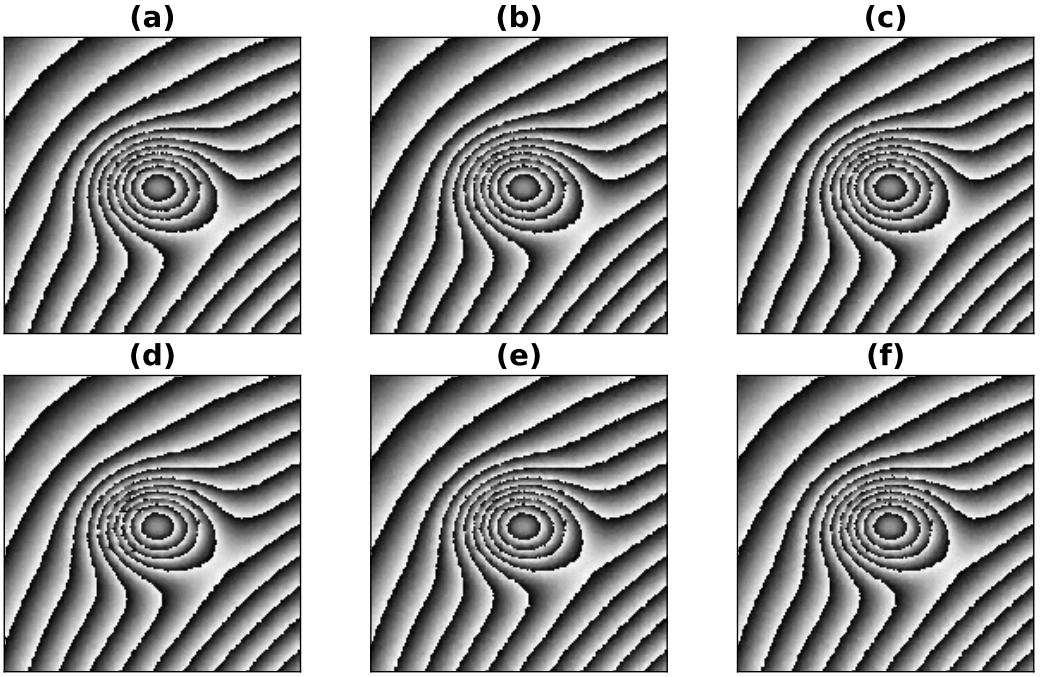

FIGURE 3.10: Denoising results obtained for the noisy wrapped phase shown in Fig. 3.9(c) using the AKF with (a) D = 1 (b) D = 10 (c) D = 20 and $\mathbf{Q}_0 = 0.5$; (d) $\mathbf{Q}_0 = 0.1$ (e) $\mathbf{Q}_0 = 0.6$ (f) $\mathbf{Q}_0 = 1$ and D = 10 [2].

qualitatively deduced from this result that the denoising performance does not change with the variations in the algorithm parameters. The quantitative performance evaluation is performed using the quality index (QI) [132], normalized-mean-square-error (NMSE) [133], and standard deviation (SD) [134], as performance metrics. The quality index is defined as

$$\mathrm{QI} = \frac{\mathrm{cov}(\phi, \hat{\phi})}{\sigma(\phi)\sigma(\hat{\phi})} \cdot \frac{2\mathrm{E}(\phi)\mathrm{E}(\hat{\phi})}{\mathrm{E}^2(\phi) + \mathrm{E}^2(\hat{\phi})} \cdot \frac{2\sigma(\phi)\sigma(\hat{\phi})}{\sigma^2(\phi) + \sigma^2(\hat{\phi})}, \tag{3.14}$$

where $\mathrm{cov}(\cdot)$, $\mathrm{E}(\cdot)$ and $\sigma(\cdot)$ represent the covariance, mean and standard deviation, respectively. In Eq. (3.14), the first, second, and third term is used to measure the degree of linear correlation, the closeness of the mean value and contrast index between noise-free (ϕ), and the denoise wrapped phase pattern ($\hat{\phi}$). The dynamic range of QI varies from –1 and 1, which corresponds to the lowest and highest similarity between ϕ and $\hat{\phi}$, respectively. The normalized mean square error (NMSE) is defined as

$$\mathrm{NMSE} = \frac{\sum |\phi - \hat{\phi}|^2}{\sum |\phi|^2}. \tag{3.15}$$

The standard deviation (SD) is defined as

$$\sigma_\theta = \sqrt{\mathrm{E}[\theta^2] - \mathrm{E}[\theta]^2}, \tag{3.16}$$

where $\theta = \phi$ - $\hat{\phi}$. Low values of NMSE and SD indicate good denoising performance.

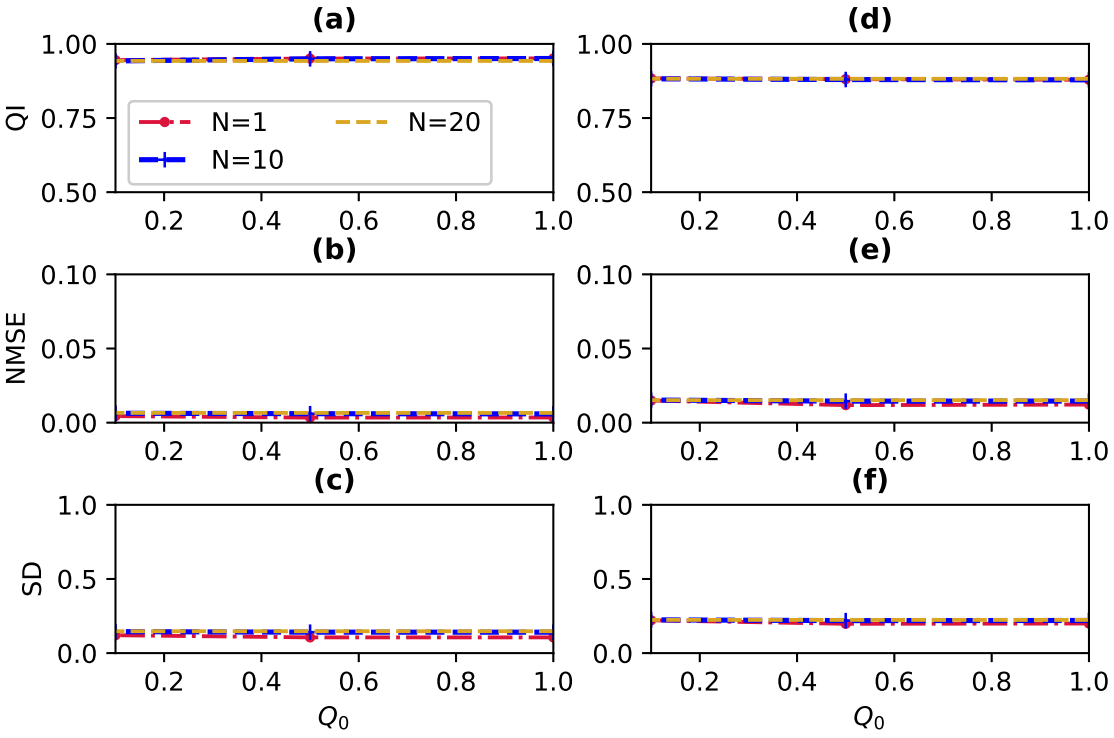

FIGURE 3.11: The plots of denoising performance metrics QI, NMSE and SD evaluated considering different values of $\mathbf{Q}_0$ and D with speckle size of 1 and 2 pixels in the first and second column, respectively. The plot legends in Fig. 3.11(a) are applicable in all the remaining sub-figures [2].

Figure 3.11 show the plots of QI, NMSE and SD evaluated in function of algorithm parameters $\mathbf{Q}_0$ and D. The first and second columns indicate the results obtained for the noisy wrapped phases in Figs. 3.9(a) and 3.9(c), respectively. It is quite evident that the performance of AKF is almost independent of algorithm parameters. On the other hand, for the purpose of comparison, the noisy wrapped phase in Fig. 3.9(c) was denoised using the WFF method [75] for different values of its algorithm parameters. The denoising results are plotted in Fig. 3.12. The fixed algorithm parameters were selected as $\sigma_\mathrm{x} = \sigma_\mathrm{y} = 10$, ωxi = ωyi = 0.1. The results in the first row were obtained by setting thr=1 (a) ωxl = ωyl = –0.2, ωxh = ωyh = 0.2, (b) ωxl = ωyl = –0.4, ωxh = ωyh = 0.4, and (c) ωxl = ωyl = –0.6, ωxh = ωyh = 0.6. The results in the second row are obtained

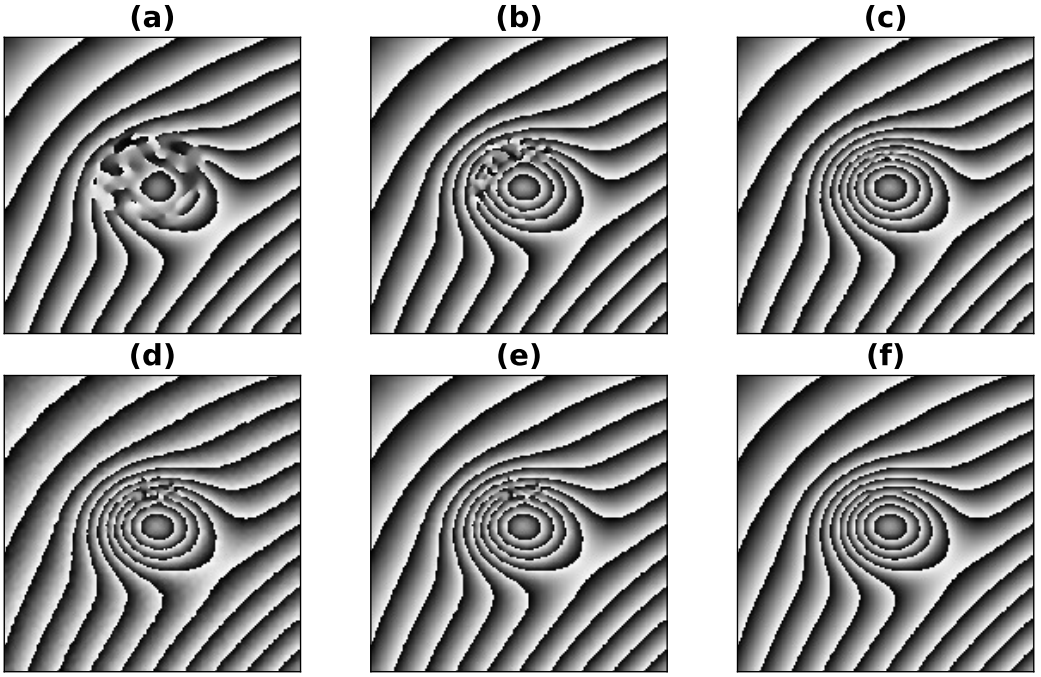

FIGURE 3.12: Denoised phase results using the WFF method for the noisy phase pattern shown in Fig. 3.9(c) with $\sigma_x = \sigma_y = 10$, ωxi = ωyi = 0.1. For the first row, the parameter were selected as thr=1, (a) ωxl = ωyl = –0.2, ωxh = ωyh = 0.2, (b) ωxl = ωyl = –0.4, ωxh = ωyh = 0.4, (c) ωxl = ωyl = –0.6, ωxh = ωyh = 0.6. For the second row, the parameter were selected as ωxl = ωyl = –0.5, ωxh = ωyh = 0.5, (d) thr = 0.1, (e) thr = 1 and (f) thr = 5 [2].

by setting ωxl = ωyl = –0.5, ωxh = ωyh = 0.5, (d) thr = 0.1, (e) thr = 1 and (f) thr = 5. It can be observed that the denoising performance of WFF method is highly sensitive to parameter selection. Apart from this qualitative comparison between the AKF and WFF, a quantitative comparison is performed in terms of the performance metrics. Table 3.3 shows the performance metrics evaluated for the AKF and the WFF in the case of results obtained in Fig. 3.10(b) and Fig. 3.12. This quantitative comparison also indicates the parameter dependency of the WFF algorithm for phase denoising. It is further verified in Fig. 3.13 wherein the residual maps of denoised phase results obtained using the AKF and WFF methods are provided.

Basically, the AKF provides a denoised EPF estimate from which the denoised phase is obtained as its argument. The absolute value of the denosied EPF can also be used as the denoised phase quality metric. Accordingly, a phase quality metric can be defined as

$$q(x, y) = |\hat{I}(x, y)|. \tag{3.17}$$

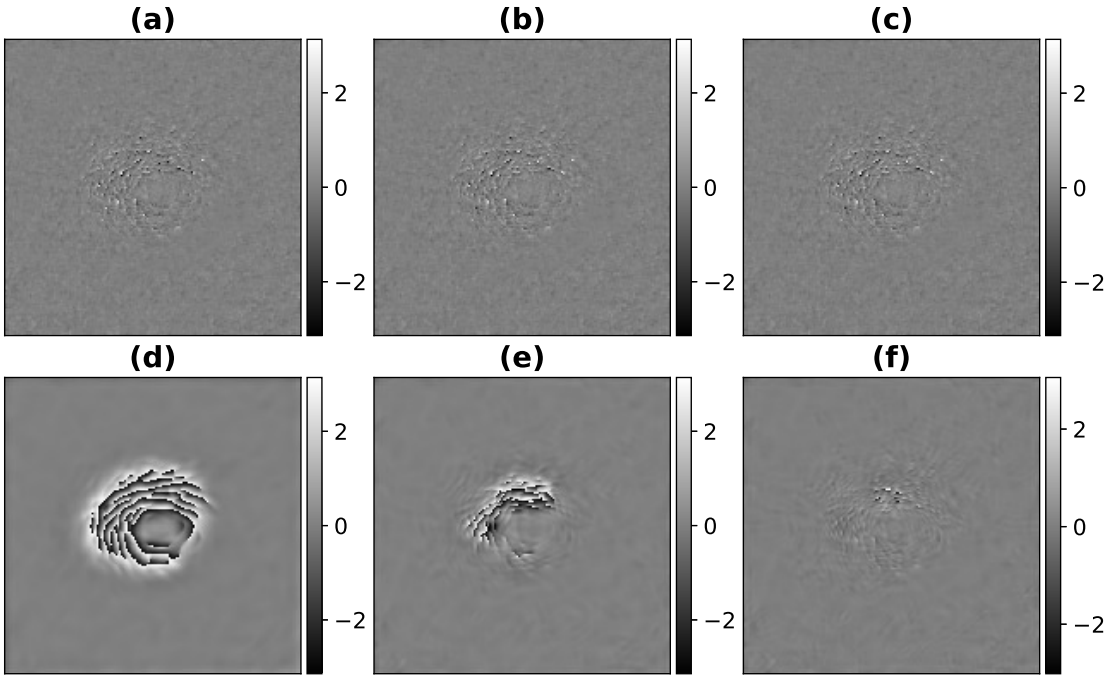

FIGURE 3.13: First row: residual maps of the denoised phase results shown in Figs. 3.10(a), 3.10(b), 3.10(c); Second row: residual maps of the denoised phase results shown in Figs. 3.12(a), 3.12(b), 3.12(c). All phase values are in radians [2].

	AKF	**WFF**					
	3.10(b)	**3.12(a)**	**3.12(b)**	**3.12(c)**	**3.12(d)**	**3.12(e)**	**3.12(f)**
QI	0.88	0.83	0.89	0.92	0.88	0.91	0.94
NMSE	0.014	0.112	0.030	0.004	0.014	0.012	0.008
SD	0.21	0.60	0.31	0.12	0.22	0.19	0.16

TABLE 3.3: Quantitative performance comparison of the AKF and WFF methods in denoising simulated phase pattern corrupted with speckle noise.

The values of q lies in the range $[0, 1]$. A low/high value of q indicates low/high phase quality at any given pixel. The first and second row of Fig. 3.14 show the phase quality map obtained using the AKF and WFF methods, respectively, for the phase examples given in Figs. 3.9(a)-(c). It can be observed from the zoom-in part of the phase quality maps that the AKF provides denoised fringe pattern without any blurring at boundary pixels. On the other hand, the WFF method introduces significant blurring effect at the image boundary due to windowing involved in the fringe processing.

Apart from the speckle noise, the performance comparison of the AKF and WFF method

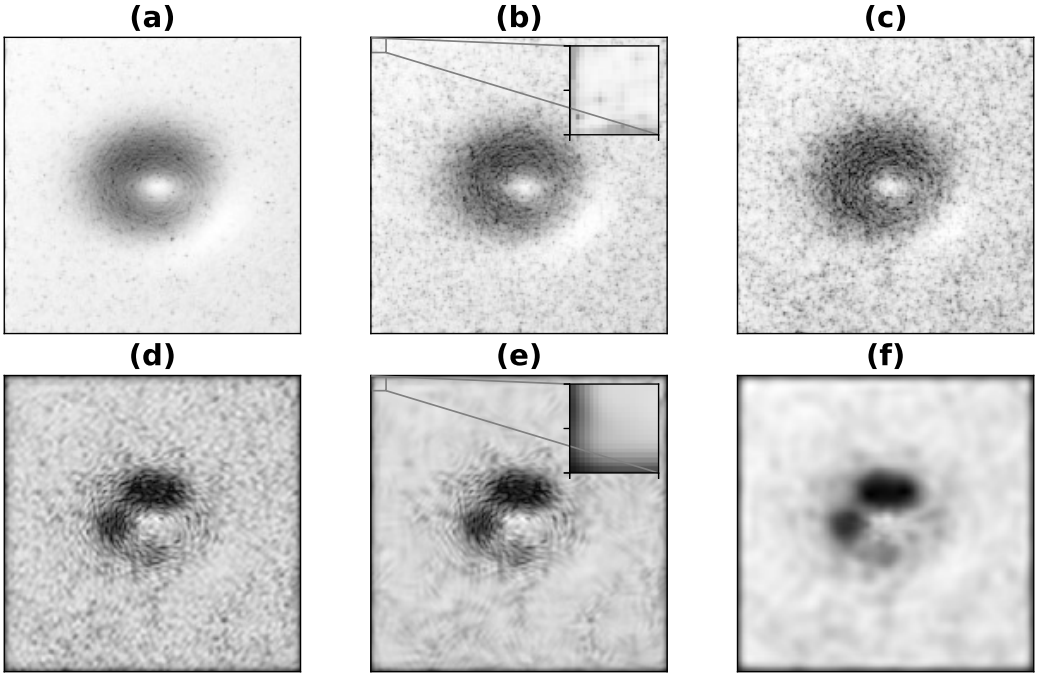

FIGURE 3.14: Quality map of above denoised results shown in Figs. 3.9(d),(e) and (f) using (a),(b) and (c) AKF method, respectively; and the above denoised results shown in Figs. 3.12(d),(e) and (f) using (d),(e) and (f) WFF method [2].

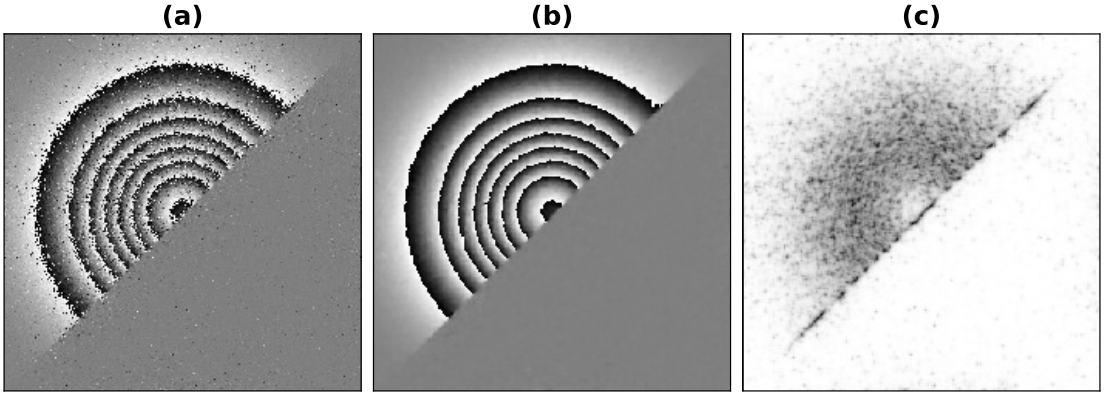

FIGURE 3.15: (a) Noisy phase pattern associated with the simulated wrapped phase shown in Fig. 3.8(b), (b) denoised phase pattern obtained using AKF, and (c) phase quality map [2].

is evaluated in function of additive complex white Gaussian noise with the wrapped phase example given in Fig. 3.8(a). Table 3.4 shows the QI, NMSE, and SD evaluated in function of signal-to-noise ratio (SNR) (in dB). It is evident that the AKF methods provided better denoising performance in the case of additive noise as well. The capability of AKF to denoise a wrapped phase consisting of inherent absolute phase discontinuities is demonstrated with the example given in Fig. 3.8(b). The wrapped phase corrupted

SNR	QI		NMSE		SD	
(dB)	**AKF**	**WFF**	**AKF**	**WFF**	**AKF**	**WFF**
2	0.87	0.93	0.0076	0.0083	0.158	0.166
5	0.92	0.94	0.0049	0.0080	0.128	0.162
10	0.95	0.95	0.0033	0.0076	0.105	0.159
15	0.97	0.96	0.0028	0.0078	0.097	0.161
20	0.98	0.96	0.0027	0.0077	0.094	0.159
25	0.98	0.97	0.0026	0.0078	0.094	0.160

TABLE 3.4: Quantitative performance comparison of the AKF and WFF methods in denoising simulated phase pattern corrupted with additive complex white Gaussian noise.

		Time (seconds)	
Methods	**Parameters**	400×400	250×350
AKF	D = 1	14.71	8.11
	D = 5	9.56	5.51
	D = 10	6.29	3.48
	D = 15	7.42	3.04
	D = 20	8.16	4.48
WFF[75]	ωxi = 0.05, ωyi = 0.05	18.29	13.45
	ωxi = 0.1, ωyi = 0.1	5.02	3.48
	ωxi = 0.2, ωyi = 0.2	1.47	1.04

TABLE 3.5: Computational time (in seconds) taken by AKF and WFF in wrapped phase denoising.

by speckle noise with speckle size of 2 pixels is shown in Fig. 3.15(a). Figure 3.15(b) shows the denoised phase pattern obtained using AKF. It can be noted that the AKF does not distort the inherent discontinuities during the denoising operation. The phase quality map is shown in Fig. 3.15(c) for the purpose of illustration.

A comparison of computational efficiency offered the AKF and WFF is provided in Table 3.5. While the computation time was evaluated in function of D in the case of AKF, for WFF method it was evaluated in function of ωxi and ωyi with $\sigma_x = \sigma_y = 10$, ωxl = ωyl = –0.5, ωxh = ωyh = 0.5, and thr = 1. The computation time of the AKF depends on D. It has been empirically observed that up to D $\approx$ 15 the computation time decreases with increase in D beyond which the computation time increases. Although the computation time required for WFF decreases with increase in ωxi and ωyi, the denoising performance deteriorates. The AKF and WFF based phase denoising algorithms were implemented using Python 3.8 on a standard computer with AMD Ryzen 3 PRO 1300 Quad-core processor at 3.50 GHz and 8 GB RAM.

Experiment

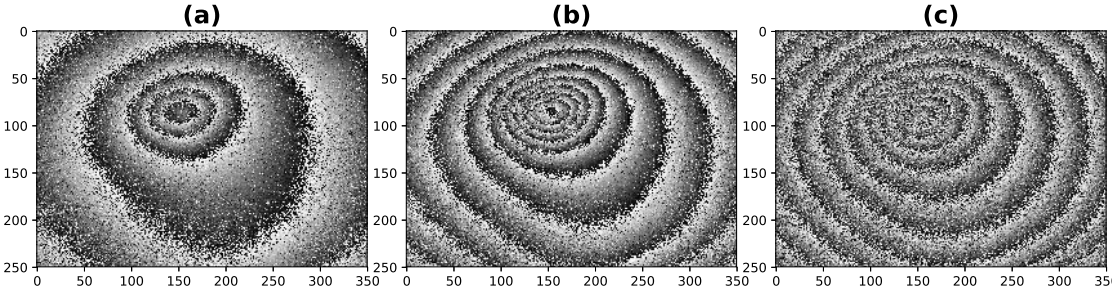

FIGURE 3.16: Experimentally recorded wrapped phase patterns in a digital holographic interferometry setup by successive increase in a point load using a rotating screw mechanism to induce out-of-plane deformation in an aluminum disk [2].

The experimental validation of the AKF is performed using the wrapped phase patterns of size 250 × 350 pixels obtained in a digital holographic interferometry setup [135]. A circular aluminum disk of diameter 25 mm and thickness 2 mm was used as an object. The disk was subjected to out-of-plane deformation using a rotating screw mechanism. A temporally varying deformation is induced in the disk by the progressive increase in the point load. Figures 3.16(a), 3.16(b), and 3.16(c) show the corresponding wrapped phases. It can be seen that the decorrelation speckle noise increases significantly with the increase in the load. Figure 3.17 shows the denoising results and its phase quality map obtained for the experimental recorded wrapped phase fringe patterns shown in

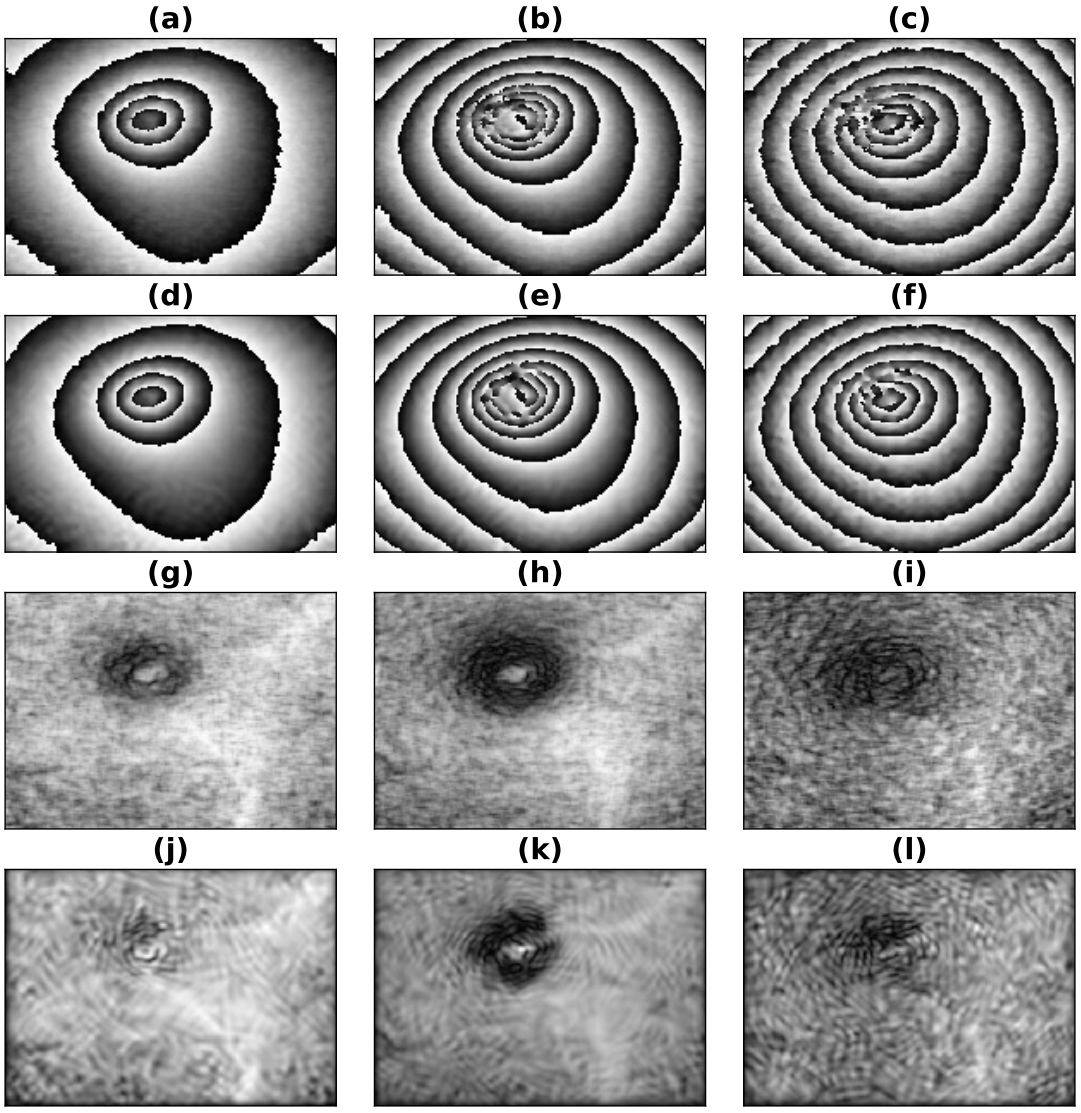

FIGURE 3.17: Denoised wrapped phases (first row) and phase quality maps (third row) obtained using the AKF method; denoised wrapped phases (second row) and phase quality maps (fourth row) obtained using the WFF method for the experimentally recorded noisy phase patterns shown in Fig. 3.16 [2].

Fig. 3.16. The first and third row of Fig. 3.17 show the denoising result, and corresponding quality map obtained using the AKF method, respectively. Similarly, the denoising results and corresponding quality map obtained using the WFF method are shown in the second and fourth row of Fig. 3.17, respectively. It can be observed that the AKF provided reliable denoised phase in each case without any manual parameter adjustments. Subsequently, these results are used to obtain unwrapped phases corresponding to the object deformation. The first row of Fig. 3.18 show the unwrapped phases obtained using the method described in [136, 137] for the wrapped phase measurements shown in Fig. 3.16. It can be observed that unreliable unwrapping results

are obtained consisting of number of undesirable phase jumps caused due to the heavy speckle noise. On the other hand, unwrapping results shown in the second and third rows of Fig. 3.18 are obtained with denoised phases and quality maps obtained using the AKF and WFF methods, respectively. It can be observed that smooth unwrapped phase maps are obtained corresponding to the continuous surface deformation.

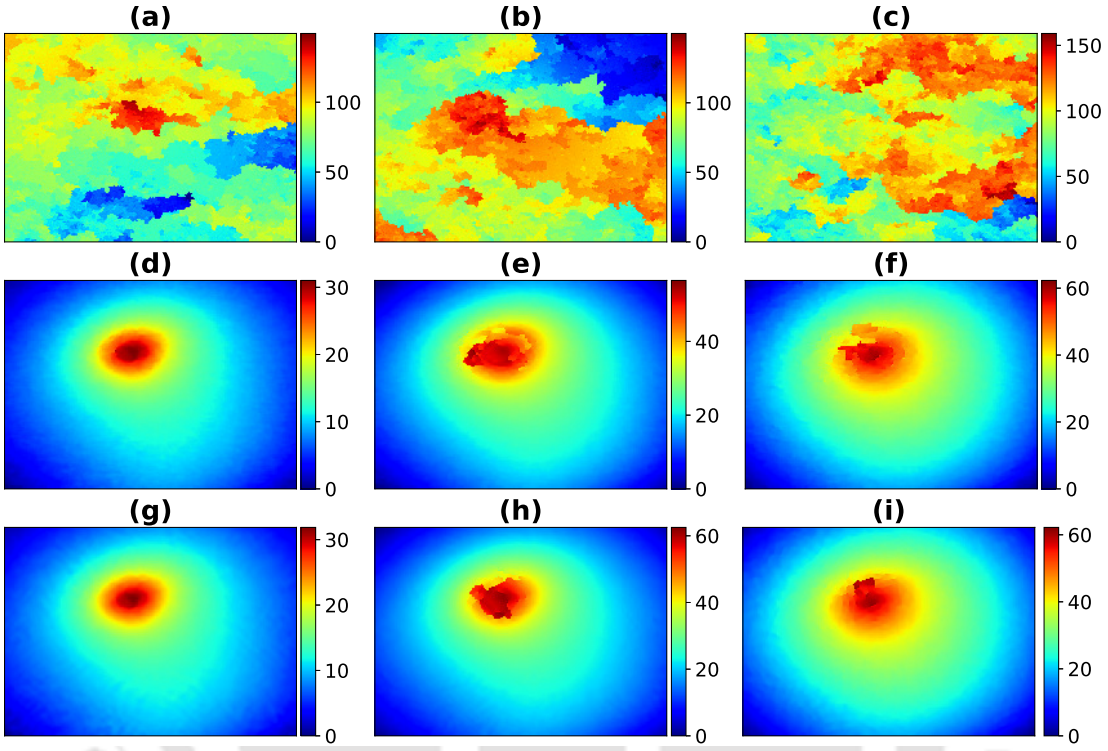

FIGURE 3.18: Unwrapped phase distributions computed with noisy phase patterns in Fig. 3.16 (first row); denoised phases and quality maps obtained using the AKF (second row) and the WFF methods (third row). All phase values are in radians [2].

3.2.3 Conclusion

In this work, the adaptive Kalman filter method is used for phase denoising, which can easily denoise continuous and discontinuous wrapped phases. The exponential phase field (EPF) generated with the noisy wrapped phase is denoised by the AKF which does not alter the desirable phase discontinuities during its operation. At the same time, the amplitude of the denoised EPF provides a phase quality map to guide the subsequent phase unwrapping process. The proposed method is robust against change in speckle noise, where the speckle noise increases with increased speckle size. The denoised results of the proposed method are extensively compared with the WFF method,

which shows that the proposed method provides outstanding performance, similar to the window Fourier filtering method without any manual parameter adjustments. Moreover, the computational efficiency of the AKF can be improved by processing multiple rows simultaneously, which can further be enhanced by using modern graphical processing units.

Chapter 4

Fringe Pattern Normalization

Fringe pattern normalization, as explained in Chapter 2, is a process of obtaining an amplitude normalized fringe pattern. In the phase-based interferometric measurements, the background intensity and fringe amplitude variations are redundant information. Therefore, it is desirable to remove these quantities during the phase demodulation as they may act as sources of errors. In fact, it is imperative to perform fringe pattern normalization in most of the closed fringe pattern demodulation and the two-frame based phase shifting techniques.

A typical non-normalized fringe pattern given in Eq. (1.1) can be represented as

$$\mathrm{I(x,y)} = \mathrm{a(x,y)} + \mathrm{b(x,y)}\cos[\phi(\mathrm{x,y})]. \tag{4.1}$$

Normalization is a process through which we can suppress the background intensity and make fringe amplitude equal to 1. Thus, the normalized fringe pattern can be represented as

$$\mathrm{I_n(x,y)} = \cos(\phi(\mathrm{x,y})) \tag{4.2}$$

The aim of a typical normalization algorithm is to obtain the normalized fringe pattern described in Eq. (4.2) from the non-normalized fringe pattern described in Eq. (4.1). We propose two strategies for the fringe pattern normalization, considering 1) row-column-wise and 2) zigzag scanning of the fringe image depending on the presence or absence of carrier fringes. If the carrier fringes are present along x-direction or y-direction, the fringe normalization can be performed in a row-wise or column-wise manner, respectively. On the other hand, if carrier fringes are present in both x-direction and y-direction or carrier fringes are not present, i.e., the case of closed fringe pattern, the fringe normalization can be performed in a zigzag manner. In practice, the zigzag scanning based strategy has been found to work in each case of fringe patterns described above.

4.1 Methodology

The fringe intensity in a given row y can be represented as

$$\mathrm{I(x)} = \mathrm{a(x)} + \mathrm{b(x)}\cos[\phi(\mathrm{x})]. \tag{4.3}$$

In general, the background intensity a(x) and fringe amplitude b(x) are slowly varying functions compared to the phase ϕ(x). Accordingly, we propose a technique using the Kalman filter to estimate a(x) and b(x) and obtain the normalized fringe signal using these estimates. At first, we define the state space model as follows. The system equation described in Eq. (1.8) is considered as

$$\mathbf{s}_\mathrm{x} = \mathbf{F}_\mathrm{x}\mathbf{s}_{\mathrm{x}-1} + \mathbf{w}_\mathrm{x}, \quad \mathbf{w}_\mathrm{x} = \mathcal{N}(0, \mathbf{Q}_\mathrm{x}), \tag{4.4}$$

and the measurement equation given in Eq. (1.9) is considered as

$$\mathbf{z}_\mathrm{x} = \mathbf{H}_\mathrm{x}\mathbf{s}_\mathrm{x} + \mathbf{v}_\mathrm{x}, \quad \mathbf{v}_\mathrm{x} = \mathcal{N}(0, \mathbf{R}_\mathrm{x}). \tag{4.5}$$

The system and measurement updates of the state $\mathbf{s}_\mathrm{x}$ are governed by the state-transition matrix $\mathbf{F}_\mathrm{x}$ and observation-matrix $\mathbf{H}_\mathrm{x}$, respectively. In the proposed method, the state $\mathbf{s}_\mathrm{x}$ represents the estimate of a(x). The system equation (Eq.(4.4)) represents a random walk model driven by the random noise process with zero mean and covariance $\mathbf{Q}_\mathrm{x}$. The measurement $\mathbf{I}_\mathrm{x}$, which basically represents the fringe intensity I(x), is considered to be corrupted by a noise process with zero mean and covariance $\mathbf{R}_\mathrm{x}$. In order to extract the slowly varying signal a(x) from I(x), we set $\mathbf{F}_\mathrm{x} = 1$ and $\mathbf{H}_\mathrm{x} = 1$ [118, 119]. For the accurate state estimation, we propose to use the computationally efficient Rauch–Tung–Striebel (RTS) smoother algorithm. The steps in the implementation of RTS algorithm [121] are described in Algorithm 3.

The state $\hat{\mathbf{s}}_\mathrm{x}^{(\mathrm{r})}$ estimated using the Algorithm 3 represents an estimate â(x) of a(x). This background intensity estimate is subtracted from the fringe intensity as

$$\begin{aligned} \mathrm{I_1(x)} &= \mathrm{I(x)} - \hat{\mathrm{a}}(\mathrm{x}) && (4.6)\\ &= \mathrm{b(x)}\cos(\phi(\mathrm{x})) && (4.7) \end{aligned}$$

The next step in the fringe normalization process is the estimation of b(x). To do this, the signal $\mathrm{I_1(x)}$ is squared to obtain

$$\begin{aligned} \mathrm{I_2(x)} &= \mathrm{I_1^2(x)} && (4.8)\\ &= \frac{\mathrm{b^2(x)}}{2}[1 + \cos(2\phi(\mathrm{x}))] && (4.9) \end{aligned}$$

It can be seen that $\mathrm{b^2(x)}/2$ represents the background intensity of the fringe signal $\mathrm{I_2(x)}$. The above described Algorithm 3 based background estimation procedure is implemented with $\mathrm{I_2(x)}$. Let $\mathrm{b_1(x)}$ represent the corresponding background intensity estimate. Based on Eq. (4.9), the fringe amplitude estimate of I(x) can be obtained as

$$\hat{\mathrm{b}}(\mathrm{x}) = \sqrt{2\mathrm{b_1(x)}} \tag{4.10}$$

Algorithm 3 Normalization using RTS smoother Kalman filter

Prediction and Update

1: The state and its associated error covariance matrix P_x are initialized at $x = 0$ as
$\hat{\mathbf{s}}_0^+ = \mathbb{E}(\mathbf{s}_0)$,
$P_0^+ = \mathbb{E}[(\mathbf{s}_0 - \hat{\mathbf{s}}_0^+)(\mathbf{s}_0 - \hat{\mathbf{s}}_0^+)^T]$,
where, $\mathbb{E}$ represents the expectation operator.

2: The forward Kalman filter is implemented for $x = 1, \cdots, K-1$ as follows
$\hat{\mathbf{s}}_x^- = \mathbf{F}_x \hat{\mathbf{s}}_{x-1}^+$,
$P_x^- = \mathbf{F}_x P_{x-1}^+ \mathbf{F}_x^T + G_x \mathbf{Q}_x G_x^T$,
$K_x = P_x^- \mathbf{H}_x^T \left(\mathbf{H}_x P_x^- \mathbf{H}_x^T + \mathbf{R}_x\right)^{-1}$,
$\hat{\mathbf{s}}_x^+ = \hat{\mathbf{s}}_x^- + K_x (\mathbf{z}_x - \mathbf{H}_x \hat{\mathbf{s}}_x^-)$,
$P_x^+ = (1 - K_x \mathbf{H}_x) P_x^- (1 - K_x \mathbf{H}_x)^T + K_x \mathbf{R}_x K_x^T$,
where, superscripts $-$ and $+$ are used to represent the *a prior* and *a posterior* estimates; $G_x = 1$; K_x is the Kalman gain.

RTS smoother algorithm

3: In the backward filtering process, the RTS smoother algorithm is initialized at $x = K-1$ as
$\hat{\mathbf{s}}_{K-1}^{(r)} = \hat{\mathbf{s}}_{K-1}^+$,
$P_{K-1}^{(r)} = P_{K-1}^+$,

4: Following steps are implemented for $x = K-2, \cdots, 0$
$B_{x+1}^- = \left(P_{x+1}^-\right)^{-1}$,
$K_x^{(r)} = P_x^+ \mathbf{F}_{x+1}^T B_{x+1}^-$,
$P_x^{(r)} = P_x^+ - K_x^{(r)} \left(P_{x+1}^- - P_{x+1}^{(r)}\right) (K_x^{(r)})^T$,
$\hat{\mathbf{s}}_x^{(r)} = \hat{\mathbf{s}}_x^+ + K_x^{(r)} \left(\hat{\mathbf{s}}_{x+1}^{(r)} - \hat{\mathbf{s}}_{x+1}^-\right)$.

Finally, the normalized fringe estimate is computed as

$$\hat{I}_n(x) = \frac{I_1(x)}{\hat{b}(x)} \tag{4.11}$$

The above described procedure is repeated in each row to obtain the two-dimensional normalized fringe pattern. Note that this procedure for the row-wise fringe pattern normalization is followed in the case of column-wise fringe pattern normalization in the exactly similar way. In the zigzag scanning strategy, the forward Kalman filter will run for all the pixel in the fringe image followed by the background filtering process.

4.2 Results

4.2.1 Simulation

Two fringe patterns each of size 256×256 were simulated as shown in Figs. 4.1(a) and 4.1(b). It can be observed that carrier fringes are present in Fig. 4.1(a), whereas Fig. 4.1(b) represents a closed fringe pattern. The colorbar indicates the gray-scale intensity (in arbitrary units (a.u.)) of the fringe image. The values of the process covariance $\mathbf{Q}_x$ used in the estimation of $a(x, y)$ $\left(\mathbf{Q}_x^{(a)}\right)$ and $b(x, y)$ $\left(\mathbf{Q}_x^{(b)}\right)$ are given in Table 4.1. Empirically, it has been observed that the proposed algorithm is not sensitive to the variations in $\mathbf{Q}_x$ around the set values.

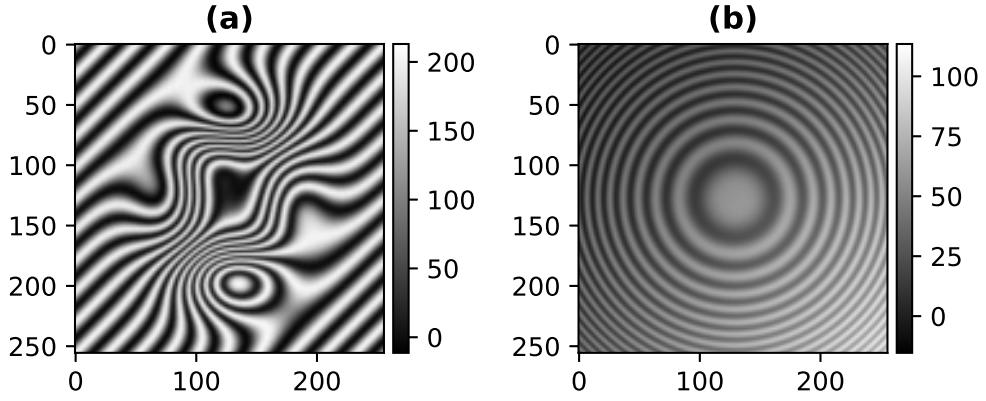

FIGURE 4.1: Simulation examples: (a) carrier-modulated fringe pattern and (b) closed fringe pattern [3].

Figures 4.2(a) and 4.2(c) show the normalized fringe patterns obtained from Fig. 4.1(a) using the zigzag and row-column scan, respectively. Similarly, Figs. 4.2(b) and 4.2(d) show the normalized fringe patterns obtained from Fig. 4.1(b) using the zigzag and row-column scan, respectively.

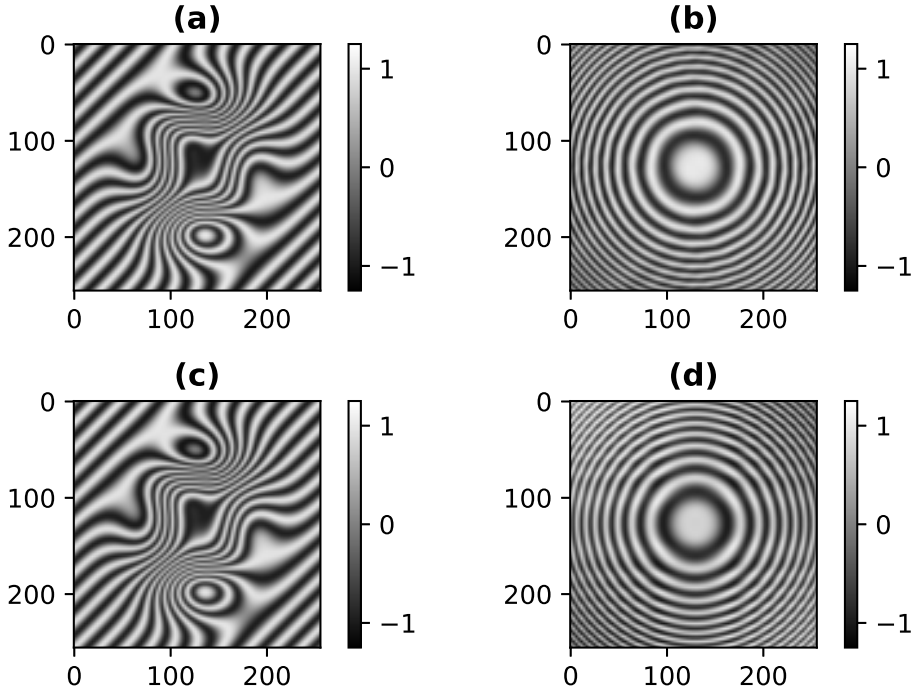

FIGURE 4.2: Normalized fringe patterns obtained using the (a),(b) zigzag scan and (c),(d) row-column scan from the fringe patterns shown in Figs. 4.1(a) and 4.1(b), respectively [3].

Qualitatively, it can be observed that the proposed algorithm successfully performed the fringe normalization for both examples. For the purpose of comparison, the one

Scan Method	Fig. 4.2(a),(c)		Fig. 4.2(b),(d)		Fig. 4.3		Fig. 4.5	
	$\mathbf{Q}_x^{(a)}$	$\mathbf{Q}_x^{(b)}$	$\mathbf{Q}_x^{(a)}$	$\mathbf{Q}_x^{(b)}$	$\mathbf{Q}_x^{(a)}$	$\mathbf{Q}_x^{(b)}$	$\mathbf{Q}_x^{(a)}$	$\mathbf{Q}_x^{(b)}$
zigzag	10^{-7}	10^{-5}	0.005	0.005	0.01	0.01	0.05	0.08
row-column	10^{-7}	10^{-5}	0.007	0.007	-	-	-	-

TABLE 4.1: Process covariance $\mathbf{Q}_x$ values selected for the fringe pattern normalization.

dimensional plot of non-normalized and normalized fringe signal at y = 128 are shown in Figs. 4.3(a) and 4.3(b), corresponding to the fringe images in Figs. 4.1(a) and 4.1(b), respectively.

The performance of the fringe normalization algorithm is quantified using the quality index (QI) defined as [138]

$$\mathrm{QI} = \frac{\sigma_{\mathrm{II_n}}}{\sigma_{\mathrm{I}}\sigma_{\mathrm{I_n}}} \frac{2\mu_{\mathrm{I}}\mu_{\mathrm{I_n}}}{\mu_{\mathrm{I}}^2 + \mu_{\mathrm{I_n}}^2} \frac{2\sigma_{\mathrm{I}}\sigma_{\mathrm{I_n}}}{\sigma_{\mathrm{I}}^2 + \sigma_{\mathrm{I_n}}^2} \tag{4.12}$$

where, μ_{I} and $\mu_{\mathrm{I_n}}$ represent mean of I and $\mathrm{I_n}$, respectively; σ_{I} and $\sigma_{\mathrm{I_n}}$ represent standard deviations of I and $\mathrm{I_n}$, respectively; $\sigma_{\mathrm{II_n}}$ represents their covariance. The quality index values evaluated for the normalized results obtained for simulated fringe patterns in Fig. 4.2 are provided in Table 4.2. It can be noted that in the case of closed fringe pattern, the zigzag scanning provides better fringe normalization performance compared to the row-column-wise scanning method.

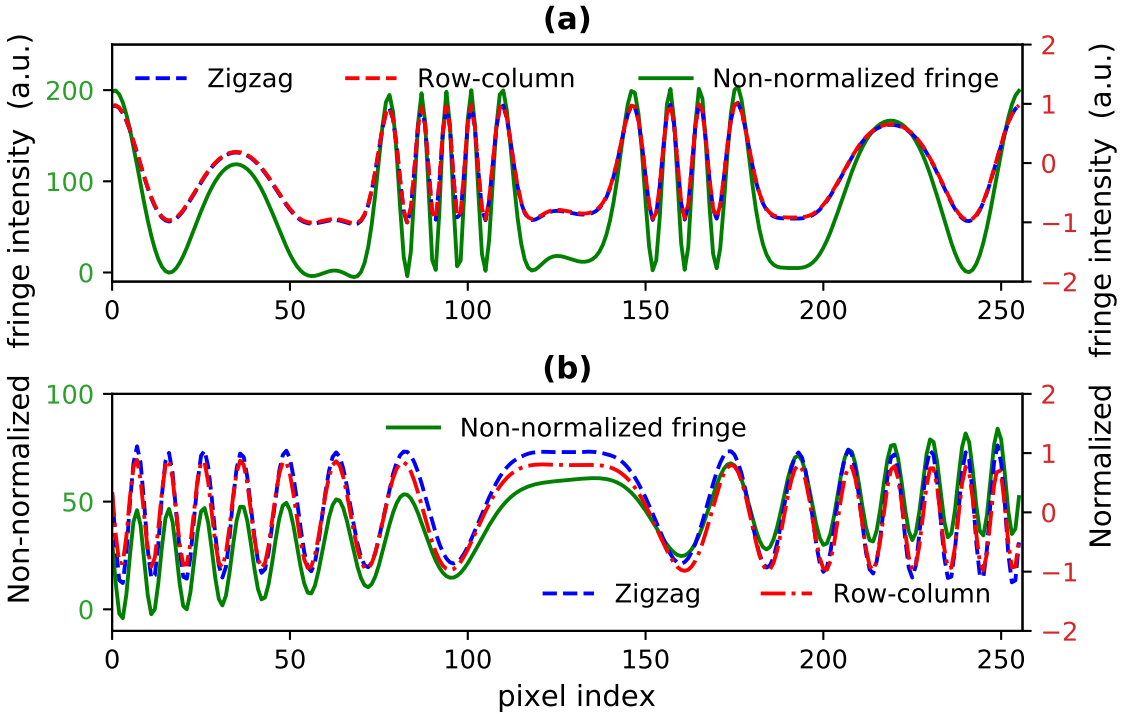

FIGURE 4.3: One-dimensional plots for (a) carrier modulated fringe pattern and (b) closed fringe pattern [3].

	Fig. 4.2(a)	Fig. 4.2(b)	Fig. 4.2(c)	Fig. 4.2(d)
QI	0.9032	0.7535	0.9035	0.5913

TABLE 4.2: Quality index values evaluated for the normalized results obtained for simulated fringe patterns.

4.2.2 Experiment

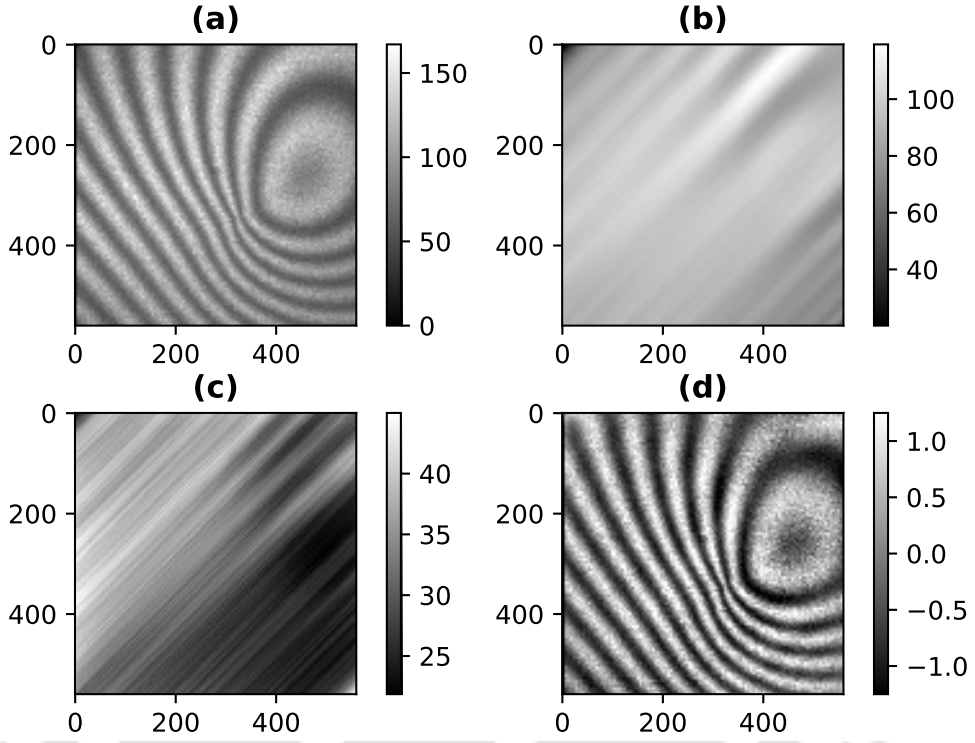

FIGURE 4.4: (a) Experimentally recorded fringe pattern in a classical holographic interferometric setup corresponding to out-of-plane displacement of an aluminum plate (b) background intensity estimate (c) fringe amplitude estimate and (d) normalized fringe pattern [3].

The experimental validation of the proposed algorithm is performed using the fringe pattern examples given in Figs. 4.4 and 4.5. The fringe pattern of size 560×560 shown in Fig. 4.4(a) was recorded in a classical holographic interferometric setup corresponding to out-of-plane displacement of an aluminum plate [139]. The fringe pattern of size 1900×2500 shown in Fig. 4.5(a) was recorded in a surface topography measurement experiment using diffraction phase microscopy [140, 141]. The zigzag scan based proposed algorithm was used to obtain the normalized fringe patterns. Figures 4.4(b) and 4.5(b) show the estimated background intensities, whereas Figs. 4.4(c) and 4.5(c) show the estimated fringe amplitudes, respectively. Finally, Figs. 4.4(d) and 4.5(d) show the normalized fringe patterns. The normalized fringe pattern intensity varies in the range of $[-1, 1]$. It can be noted that the fringe contrast value varies in the range of $[0, 1]$ wherein 0 and 1 indicates lowest and highest contrast, respectively. The contrast value calculated for Figs. 4.2 (a), Figs. 4.2 (b), Figs. 4.2 (c), Figs. 4.2 (d), Figs. 4.4 (d), and Figs. 4.5 (d) were 0.9939, 0.9612, 0.9816, 0.9198, 0.897, and 0.876, respectively.

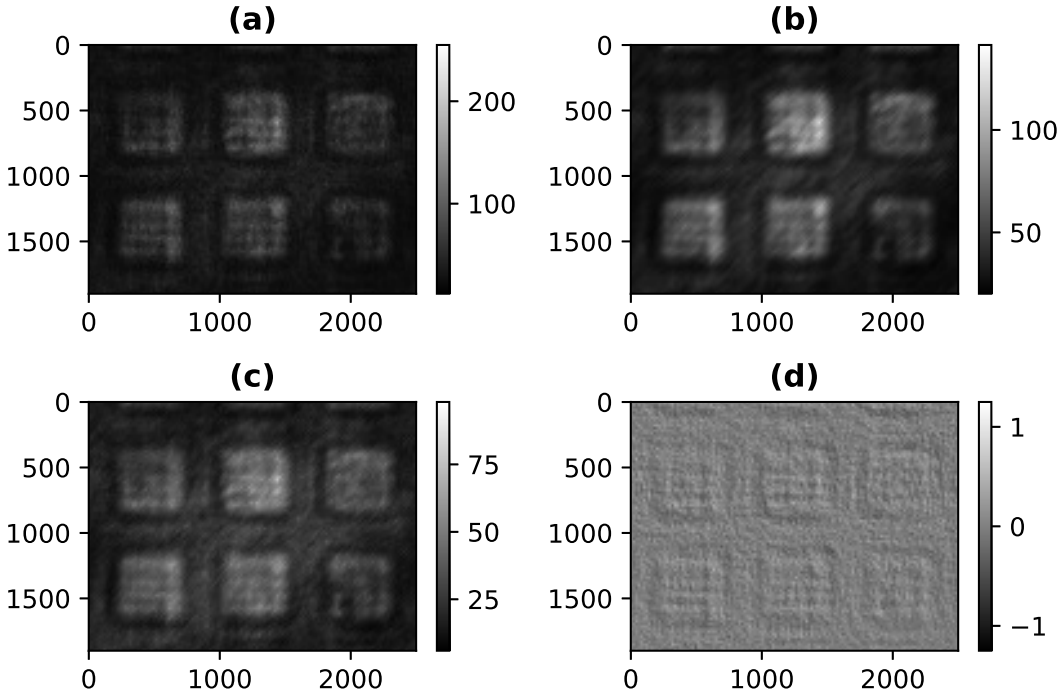

FIGURE 4.5: (a) Fringe pattern recorded in a diffraction phase microscopy setup (b) background intensity estimate (c) fringe amplitude estimate and (d) normalized fringe pattern [3].

In this normalization work, a scalar measurement variable is considered as the fringe processing is performed in a row-wise and column-wise manner. At the same time, the state, representing the background intensity estimate, is also a scalar variable. Empirically, we have observed that implementing the proposed algorithm by considering a state vector with elements representing intensity estimates from a set of rows or columns increases the computation time without significant improvement in the fringe normalization results. Moreover, implementation of the proposed zigzag scheme is not feasible with state vector with more than one element. Therefore, we have considered the Kalman filter implementation with scalar state variable. The computation time taken by the proposed method based on zigzag scheme in the normalization of fringe patterns of sizes 256×256, 560×560 and 1900×2500 was 1.4, 7.9 and 110 seconds, respectively. The use of graphical processing units may further improve the computational efficiency of the proposed method especially for real-time fringe processing application.

4.3 Conclusion

In this chapter, a new method for fringe normalization is proposed using Kalman filter. The random walk modeling of the fringe intensity allows to accurately capture the fringe intensity variations. The proposed algorithm was found to effectively perform the normalization of both carrier-modulated and closed fringe patterns. The simulation and experimental results demonstrate the fringe normalization capability of the proposed algorithm. We conclude that in case of closed fringe pattern, the zigzag scanning perform better fringe normalization compared to the row-column-wise scanning method.

Chapter 5

Spatial Carrier Fringe Pattern Demodulation

In optical interferometric measurement techniques, quantitative information of the measurand is encoded in the phase of a fringe pattern. Therefore, accurate estimation of phase from the fringe pattern is of prime importance. The phase estimation from a single carrier modulated fringe pattern allows for dynamic physical quantity measurements. The introduction of an appropriate amount of carrier fringes is essential for obtaining a sign-unambiguous phase estimate. Different phase demodulation technique have been previously discussed in Section 2.3.1.

In this chapter, different spatial carrier fringe pattern demodulation techniques are reported. In these techniques, the carrier fringe frequency is simultaneously estimated along with the required phase. This feature allows removal of the carrier phase contribution from the estimated phase.

5.1 Carrier Fringe Pattern Demodulation using Extended Complex Kalman Filter

5.1.1 Methodology

A spatial carrier fringe pattern can be represented as

$$\mathrm{I(x,y)} = \mathrm{a(x,y)} + \mathrm{b(x,y)}\cos[\phi(\mathrm{x,y}) + \omega_{\mathrm{x}}\mathrm{x}]. \tag{5.1}$$

In the proposed method, it is required to remove the background intensity a(x, y) prior to the phase demodulation. The background intensity can be removed either using the technique described in the previous chapter on fringe normalization or using a high pass filtering technique [142, 143]. The background removed fringe pattern can be represented as

$$\mathrm{I(x,y)} = \mathrm{b(x,y)}\cos[\phi(\mathrm{x,y}) + \omega_{\mathrm{x}}\mathrm{x}]. \tag{5.2}$$

Since the carrier fringes are introduced along x-direction, the phase demodulation is performed in a row-wise manner. Accordingly, one dimensional fringe pattern in a given row y can be represented as

$$\mathrm{I(x)} = \mathrm{b(x)}\cos[\phi(\mathrm{x}) + \omega_{\mathrm{x}}\mathrm{x}]. \tag{5.3}$$

One dimensional complex form of the above equation can also be represented as

$$\mathrm{I(x)} = \frac{\mathrm{b(x)}}{2}\exp[\mathrm{j}(\phi(\mathrm{x}) + \omega_{\mathrm{x}}\mathrm{x})] + \frac{\mathrm{b(x)}}{2}\exp[-\mathrm{j}(\phi(\mathrm{x}) + \omega_{\mathrm{x}}\mathrm{x})]. \tag{5.4}$$

where, $\mathrm{j} = \sqrt{-1}$. We consider $\Phi(\mathrm{x}) = \phi(\mathrm{x}) + \omega_{\mathrm{x}}\mathrm{x}$. Accordingly, we have

$$\mathrm{I(x)} = \frac{\mathrm{b(x)}}{2}\exp[\mathrm{j}\Phi(\mathrm{x})] + \frac{\mathrm{b(x)}}{2}\exp[-\mathrm{j}\Phi(\mathrm{x})]. \tag{5.5}$$

The fringe signal can be represented in an auto-regressive complex form as follows [144]

$$\begin{bmatrix} \alpha \\ \mathbf{S}_{\mathrm{x}} \\ \mathbf{S}^{*}_{\mathrm{x}} \end{bmatrix} = \begin{bmatrix} 1 & 0 & 0 \\ 0 & \alpha & 0 \\ 0 & 0 & \alpha \end{bmatrix} \begin{bmatrix} \alpha \\ \mathbf{S}_{\mathrm{x-1}} \\ \mathbf{S}^{*}_{\mathrm{x-1}} \end{bmatrix} \tag{5.6}$$

$$\mathrm{I(x)} = \begin{bmatrix} 0 & 0.5 & 0.5 \end{bmatrix} \begin{bmatrix} \alpha \\ \mathbf{S}_{\mathrm{x}} \\ \mathbf{S}^{*}_{\mathrm{x}} \end{bmatrix} + \epsilon_{\mathrm{x}} \tag{5.7}$$

where ϵ_{x} is the measurement noise, and

$$\alpha = \exp(\mathrm{j}\omega_{\mathrm{x}}), \tag{5.8}$$

$$\mathbf{S}_{\mathrm{x}} = \mathrm{b(x)}\exp[\mathrm{j}\Phi(\mathrm{x})], \tag{5.9}$$

$$\mathbf{S}^{*}_{\mathrm{x}} = \mathrm{b(x)}\exp[-\mathrm{j}\Phi(\mathrm{x})]. \tag{5.10}$$

The state-space formulation of the above auto-regressive model can be represented as

$$\mathbf{s}_{\mathrm{x}} = \mathbf{f}(\mathbf{s}_{\mathrm{x-1}}). \tag{5.11}$$

$$\hat{\mathrm{I}}(\mathrm{x}) = \mathbf{H}\mathbf{s}_{\mathrm{x}}. \tag{5.12}$$

where,

$$\mathbf{s}_{\mathrm{x}} = \begin{bmatrix} \alpha \\ \mathbf{S}_{\mathrm{x}} \\ \mathbf{S}^{*}_{\mathrm{x}} \end{bmatrix}, \mathbf{f}(\mathbf{s}_{\mathrm{x}}) = \begin{bmatrix} \alpha \\ \alpha\mathbf{S}_{\mathrm{x}} \\ \frac{\mathbf{S}^{*}_{\mathrm{x}}}{\alpha} \end{bmatrix}, \mathbf{H} = \begin{bmatrix} 0 & 0.5 & 0.5 \end{bmatrix}. \tag{5.13}$$

Here, $\hat{\mathrm{I}}(\mathrm{x})$ represents the measurement estimates. Due to the involvement of non-linear process update model, the state estimation is performed using the extended complex Kalman filter (ECKF) as described in Algorithm 4 below [121].

The estimates of phase $\hat{\Phi}_{\mathrm{x}}$ and carrier frequency $\hat{\omega}_{\mathrm{x}}(\mathrm{x})$ are obtained using the Algorithm 4. The histogram of carrier frequency estimates is computed. The frequency value with the highest number of occurrences is considered for the carrier phase removal. The phase

Algorithm 4 Phase demodulation using extended complex Kalman filter

1: Initialize the state vector estimate and its error covariance matrix P as

$\hat{\mathbf{s}}_0^+ = \mathrm{E}(\mathbf{s}_0)$,

$\mathrm{P}_0^+ = \mathrm{E}[(\mathbf{s}_0 - \hat{\mathbf{s}}_0^+)(\mathbf{s}_0 - \hat{\mathbf{s}}_0^+)^{\mathrm{T}}]$,

where, E represents the expectation operator. The superscripts – and + indicate the a priori and a posteriori estimates of the associated variables.

2: The process update equation for a priori state estimation at x= 1,2, $\cdots$ is given as

$\hat{\mathbf{s}}_{\mathrm{x}}^- = \mathrm{f}(\hat{\mathbf{s}}_{\mathrm{x}-1}^+)$,

$\mathrm{P}_{\mathrm{x}}^- = \mathbf{F}_{\mathrm{x}}\mathrm{P}_{\mathrm{x}-1}^+\mathbf{F}_{\mathrm{x}}^{\mathrm{T}} + \mathbf{Q}_{\mathrm{x}}$,

where, $\mathbf{F}_{\mathrm{x}} = \frac{\partial \mathbf{f}(\mathbf{s}_{\mathrm{x}})}{\partial(\mathbf{s}_{\mathrm{x}})} = \begin{bmatrix} 1 & 0 & 0 \\ \hat{\mathbf{s}}_{\mathrm{x}}^-(2) & \hat{\mathbf{s}}_{\mathrm{x}}^-(1) & 0 \\ \frac{\hat{\mathbf{s}}_{\mathrm{x}}^-(3)}{\hat{\mathbf{s}}_{\mathrm{x}}^-(1)^2} & 0 & \frac{1}{\hat{\mathbf{s}}_{\mathrm{x}}^-(1)} \end{bmatrix}$ and $\mathbf{Q}_{\mathrm{x}}$ is the process covariance matrix.

3: The Kalman gain is computed as

$\mathrm{K}_{\mathrm{x}} = \mathrm{P}_{\mathrm{x}}^-\mathbf{H}^{\mathrm{T}}[\mathbf{H}\mathrm{P}_{\mathrm{x}}^-\mathbf{H}^{\mathrm{T}} + \mathbf{R}_{\mathrm{x}}]$,

Where $\mathbf{R}_{\mathrm{x}}$ is the measurement noise variance.

4: A posterior state estimates are obtained by taking the measurement of fringe intensity into account as follows:

$\hat{\mathbf{s}}_{\mathrm{x}}^+ = \hat{\mathbf{s}}_{\mathrm{x}}^- + \mathrm{K}_{\mathrm{x}}(\mathrm{I}(\mathrm{x}) - \mathbf{H}\hat{\mathbf{s}}_{\mathrm{x}}^-)$,

$\mathrm{P}_{\mathrm{x}}^+ = \mathrm{P}_{\mathrm{x}}^- - \mathrm{K}_{\mathrm{x}}\mathbf{H}\mathrm{P}_{\mathrm{x}}^-$,

5: The phase estimate at x with carrier fringe contribution is obtained as

$\hat{\Phi}_{\mathrm{x}} = \arg[\hat{\mathbf{s}}_{\mathrm{x}}^+(2)]$,

where arg(.) provides angle (in radians) associated with the complex valued input signal; $\hat{\Phi}_{\mathrm{x}} = \phi(\mathrm{x}) + \omega_{\mathrm{x}}\mathrm{x}$; The performance of the above described forward Kalman filtering approach $(\mathrm{x} = 1, 2, \cdots)$ of state estimation can be improved using fixed-lag Kalman smoother method. Accordingly, We utilize the RTS smoother algorithm for the state estimation.

6: Along with the phase estimate, the carrier frequency estimate $\hat{\omega}_{\mathrm{x}}$ is also computed at each pixel as

$\hat{\omega}_{\mathrm{x}}(\mathrm{x}) = \arg[\hat{\mathbf{s}}_{\mathrm{x}}^+(1)]$

estimate after removing the contribution of the carrier fringes can be obtained as

$$\hat{\phi}(\mathrm{x}) = \mathcal{W}[\hat{\Phi}(\mathrm{x}) - \hat{\omega}_{\mathrm{x}}(\mathrm{x}) \cdot \mathrm{x}] \tag{5.14}$$

where $\mathcal{W}(\cdot)$ is the phase wrapping operator defined as the four-quadrant inverse tangent

$$\mathcal{W}(\cdot) = \tan^{-1}\left[\frac{\sin(\cdot)}{\cos(\cdot)}\right] \tag{5.15}$$

5.1.2 Results

Simulation results

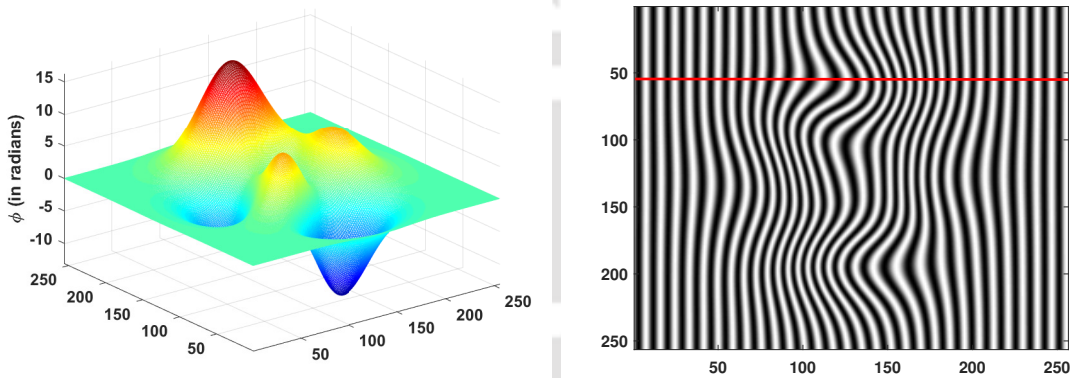

(a) (b)

FIGURE 5.1: Simulated (a) phase and (b) fringe pattern with k = 2 and m = 30. The phase values are in radians [4].

The simulation study was performed with the phase distribution and the carrier frequency simulated as

$$\phi = \mathrm{k} \times \mathrm{peaks(K)}, \tag{5.16}$$

$$\omega_{\mathrm{x}} = \mathrm{m} \times \frac{2\pi}{\mathrm{K}}. \tag{5.17}$$

The fringe patterns of size 256×256 were considered. The phase ϕ was simulated with peaks function available in MATLAB with the scaling parameter k. The carrier frequency (in radians/pixel) was generated with scaling parameters m. The phase ϕ and associated simulated fringe pattern with k = 2 and m = 30 are shown in Figure 5.1(a) and Figure 5.1(b) respectively. The performance comparison between the FT, WFT, RQF and ECKF methods was performed with different values of k and m in terms of the root-mean-square-error (RMSE) in the phase estimation. In the computation of RMSEs,

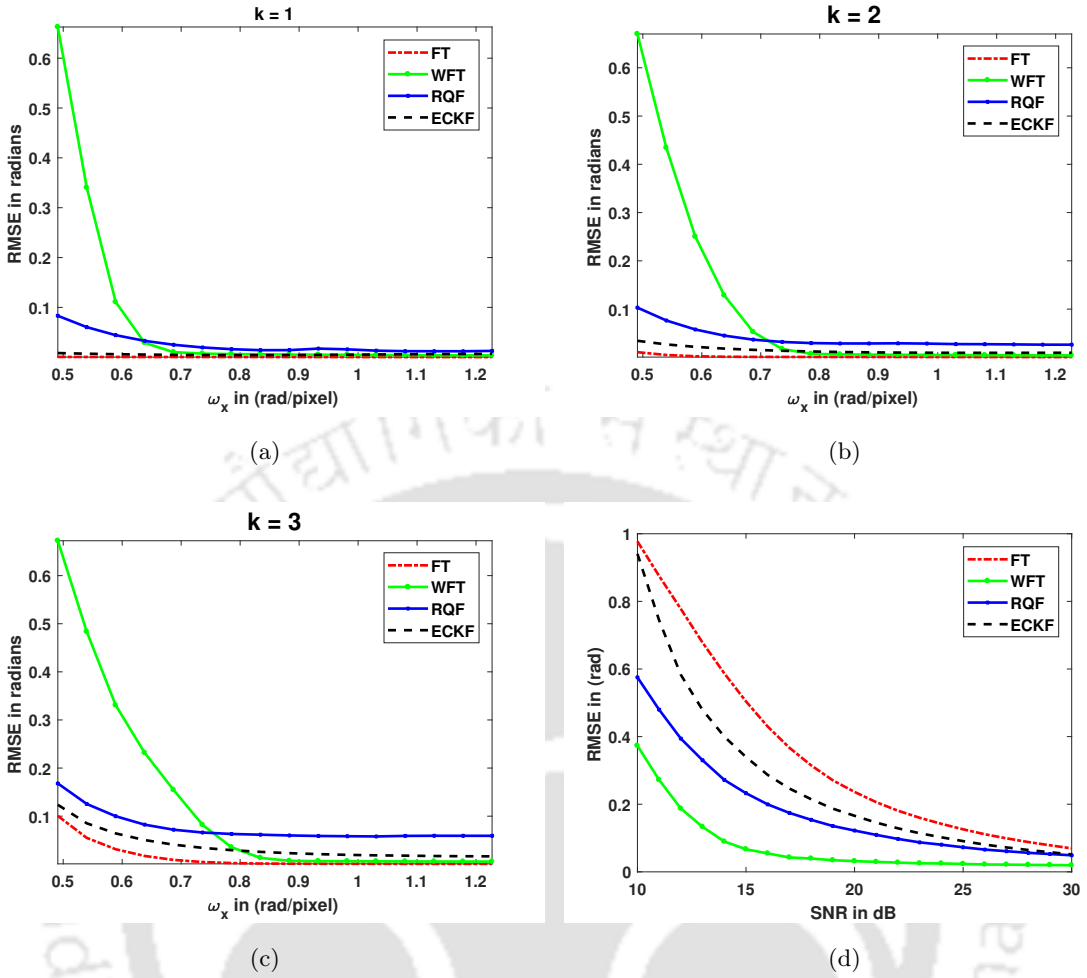

FIGURE 5.2: RMSEs in the phase estimation in function of carrier frequency with (a) k = 1 (b) k=2 and (c) k=3. (d) RMSEs in the phase estimation in function of SNR(in dB) with k = 2, m = 30 [4]

.

image border pixels are not taken into consideration. Table 5.1 provides the parameter settings considered in the algorithm implementations.

Figures 5.2(a), 5.2(b), and 5.2(c) show the plot of RMSEs in function of carrier frequencies for k=1, k=2 and k=3, respectively. The plot given in Fig. 5.2(d) shows the RMSEs computed in function of the signal-to-noise (SNR) ratio (in dB) for k = 2 and m = 30. At each SNR, the RMSE is computed as an average of 20 simulation runs. From these results, it can be noted that the performances of the FT and ECKF methods are independent of carrier frequency. On the other hand, the phase estimation accuracy of the WFT and RQF method depends on the carrier frequency selection for the given phase distribution. Moreover, carrier frequency need to be known to certain accuracy in the

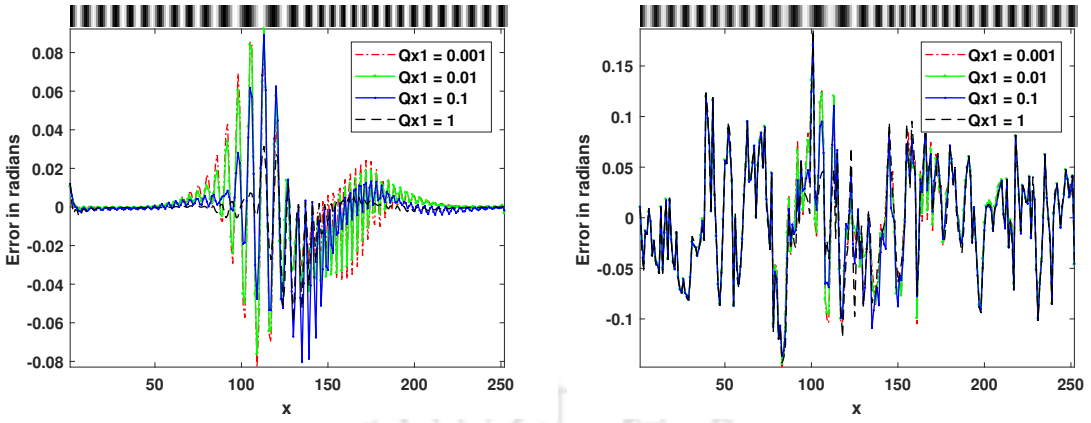

(a) (b)

FIGURE 5.3: Error in the phase estimation along the 54th row of the fringe pattern simulated with k = 2, m= 30 and (a) SNR = ∞ dB and (b) SNR = 20 dB in function of the process covariance values associated with α [4]

.

TABLE 5.1: Algorithm parameters for carrier fringe demodulation algorithms.

Methods	**Algorithm parameters**
FT[145]	Frequency domain masking half plane.
WFT[75]	$\alpha = 10, \omega_{\mathrm{xl}} = -1, \omega_{\mathrm{xt}} = 0.1, \omega_{\mathrm{xh}} = 1, \omega_{\mathrm{yl}} = -(\omega_{\mathrm{c}} + 1), \omega_{\mathrm{yt}} = 0.1, \omega_{\mathrm{yh}} = (\omega_{\mathrm{c}} + 1), \mathrm{thr} = 0.5.$
RQF[146]	$\lambda = 3, \tau = 0.1, \mathrm{iteration} = 5.$
ECKF	$\hat{\mathrm{s}}_0^+ = [\exp(\mathrm{j}\pi/5); \exp(\mathrm{j}\pi/5); \exp(\mathrm{j}\pi/5)], \mathrm{P}_0^+ = \mathrm{diag}([1; 100; 100]),$ $\mathbf{Q}_{\mathrm{x}} = \mathrm{diag}([0.01; 100; 100]), \mathbf{R}_{\mathrm{x}} = 10.$

implementation of the WFT and RQF methods. In addition, for the reliable phase estimation, the algorithm parameters need to be tuned depending on some prior knowledge of the underlying phase. It is not, however, the case with the proposed ECKF method wherein same algorithm parameters are used in each case. On the other hand, for a sufficiently high carrier frequency, the noise robustness of the WFT method is higher compared to other methods.

Figure 5.3(a) and 5.3(b) show the error in the estimated phase computed with the ECKF method along the 54th row of the fringe pattern (shown as red color line in Fig. 5.1(b) simulated with SNR = ∞ dB and SNR = 20 dB, respectively. The error plots are given for four different values $\mathrm{Q}_{\mathrm{x1}}(\mathbf{Q}_{\mathrm{x}}(1,1))$ = [0.001, 0.01, 0.1, 1] which represent the process

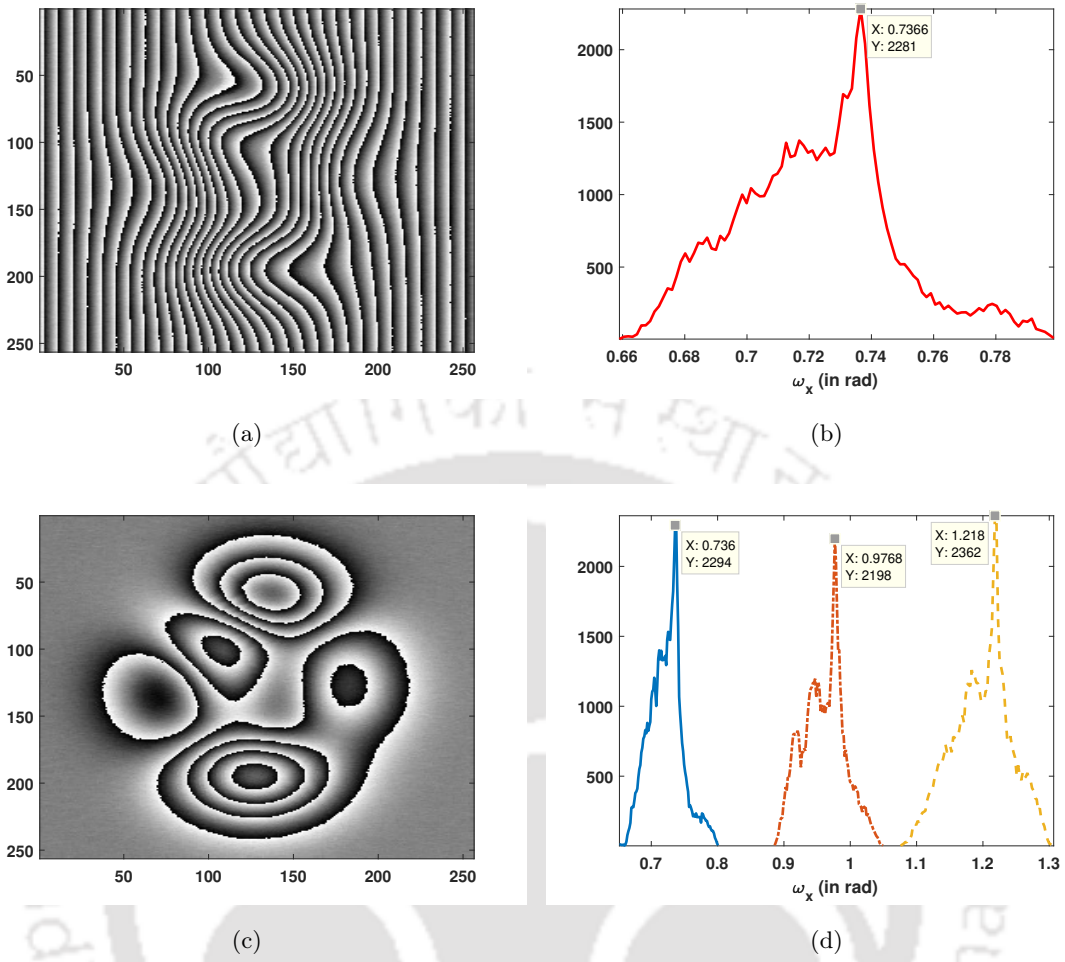

FIGURE 5.4: (a) Estimated phase (with carrier contribution) using the ECKF method from the fringe pattern simulated with k = 3, m = 30 and SNR = 20 dB (b) histogram counts of frequency estimates indicating peak at carrier fringe frequency (c) estimated phase without carrier using the ECKF method and (d) histogram counts of frequency estimates indicating peaks at different carrier fringe frequencies [4]

.

covariance associated with the state α. Since the proposed algorithm is performing the local phase demodulation, the fringe frequency is estimated at each pixel. The spatial variation of the phase ϕ(x) results in the change in the local fringe frequency. Higher the ϕ(x), higher will be the the local fringe frequency and vice a versa. Since the state space process model assumes spatially invariant carrier frequency, the deviation from this assumption due to ϕ(x) is incorporated in the state space model in the form of a finite process covariance Q_{x1}. Accordingly, high divergence in local frequency from the carrier frequency claim higher value of Q_{x1} and vice a versa. From the simulation results, it can be observed that, in the noiseless condition, a higher value of Q_{x1} grants higher

estimation accuracy with other parameter remaining constant but higher value of Q_{x1} makes algorithm more sensitive to noise. Accordingly, the differences between the error performance for different values of Q_{x1} are found to diminish in the presence of noise. In practice, we have observed that a selection of $Q_{x1} = 0.01$ provides acceptable phase estimation accuracy with different fringe pattern examples.

One of the key advantage of the proposed method is its carrier fringe removal capability. As described above, the proposed method allows to remove the contribution of carrier phase from the estimated phase based on the carrier frequency estimate (See Eq. (5.14)). Figure 5.4(a) shows the estimated phase from the fringe pattern simulated with k = 3, m = 30 and SNR = 20 dB. The frequency estimate is computed at each pixel along with the phase. The histogram counts of the frequency estimates is shown in Fig. 5.4(b). The frequency estimate with the highest count is selected as the carrier frequency estimate $\hat{\omega}_x$. The carrier phase contribution is removed using this estimate to obtain the required estimate of ϕ as shown in Fig. 5.4(c). It can be observed that the proposed method is able to remove the carrier phase contribution. The same experiment was performed using m = 30, m = 40 and m = 50 with other parameters remaining the same. Figure 5.4(d) shows that the proposed method could accurately estimate the carrier frequency in each case.

Experiment

The experimental validation of the proposed method was performed using spatial carrier fringe pattern shown in Figs. 5.5(a) and 5.6(a) which are recorded in an optical interferometry setup and fringe projection profilometry setup, respectively. Upon application of the proposed method to these fringe patterns, the phase estimates with carrier phase contribution were obtained as shown in Figs. 5.5(b) and 5.6(b), respectively. The carrier fringe frequency were also estimated simultaneously. Figs. 5.5(c) and 5.6(c) represent the phase estimates obtained after removal of carrier phase contribution. It can be clearly observed that the proposed method could successfully remove the auxiliary horizontal carrier fringe contribution to provide only the measurand related phase distribution (ϕ). Finally, the unwrapped phase estimates is shown in Figs. 5.5(d) and 5.6(d) obtained

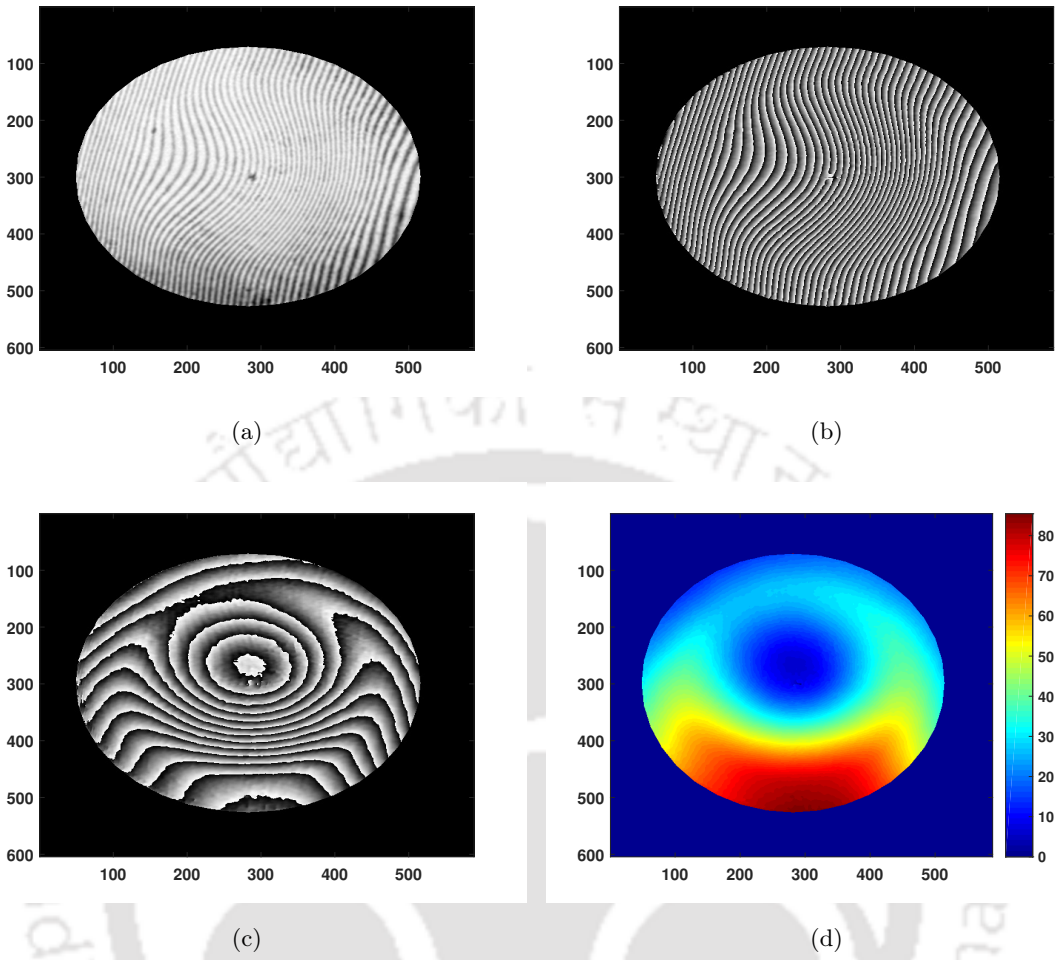

FIGURE 5.5: (a) Experimentally recorded spatial carrier fringe pattern in an optical interferometry setup (b) phase estimate (with carrier phase contribution) obtained using the ECKF method (c) phase estimate after removal of carrier phase contribution and (d) unwrapped phase estimate (in radians) [4].

using the method reported in [136, 137]. The phase estimate was also obtained using the PSI technique for the fringe pattern example given in 5.6(b). A very small difference was observed between the phase estimates obtained using proposed ECKF method and the PSI technique.

5.1.3 Discussion

One of the most important advantage of the ECKF method is its local fringe demodulation capability in which the phase estimation is performed pixel-wise. This local fringe modulation capability is useful in the condition where fringe data is available only within the certain portions of the image area, for example, circular region within a rectangular

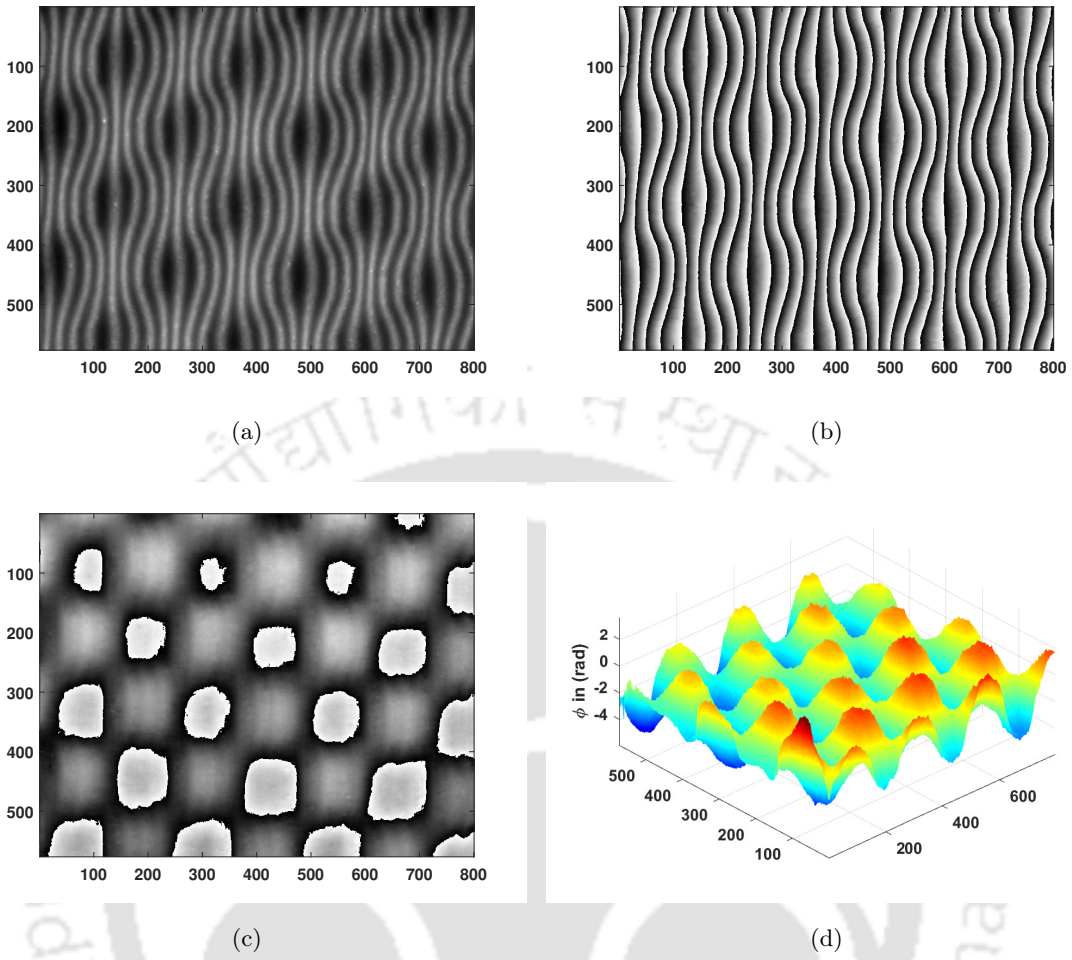

FIGURE 5.6: (a) Experimentally recorded spatial carrier fringe pattern in a fringe projection profilometry setup corresponding to a corrugated foam sheet. Phase estimate obtained using the ECKF method (b) with and (c) without carrier phase contribution and (d) unwrapped phase estimate (in radians) [4].

image. While the FT method utilizes the entire image in the demodulation process, the WFT performs local fringe demodulation operating with the fringe data available within a window which hampers phase estimation accuracy along the borders of valid and invalid fringe regions. The FT, WFT and RQF methods require the accurate knowledge of carrier frequency for the reliable phase estimation. On the other hand, the ECKF method does not require the accurate knowledge of carrier frequency. In fact, the state space model of fringe evolution allows simultaneous estimation carrier fringe frequency and phase which helps in removing carrier fringe contribution and automating the fringe analysis procedure. In the implementation of Kalman filter, the values of process and measurement noise covariance, $\mathbf{Q}_{\mathrm{X}}$ and $\mathbf{R}_{\mathrm{X}}$, are considered to be constant. However, their

values may vary with pixel location.

5.1.4 Conclusion

In this work, spatial carrier fringe analysis based on extended complex Kalman filter is found to provide satisfactory results in the phase demodulation. The state space model of fringe evolution allows simultaneous estimation carrier fringe frequency and phase which helps in removing carrier fringe contribution and automating the fringe analysis process.

5.2 Spatial Carrier Fringe Pattern Demodulation using Adaptive Extended Complex Kalman Filter

In the previous section, the author has discussed an extended complex Kalman filter (ECKF) based model for the demodulation of spatial carrier fringes. This method is implemented considering a fixed user-defined value of measurement noise covariance. However, since the noise strength varies spatially over the fringe pattern, the value of its covariance may vary at each pixel location. This section reports an adaptive extended complex Kalman filter (AECKF) method for the fringe demodulation wherein the measurement noise covariance is adaptively estimated at each pixel.

5.2.1 Methodology

A carrier modulated fringe pattern can be represented as below

$$\mathrm{I(x,y) = a(x,y) + b(x,y)\cos[\phi(x,y) + \omega_x x]}. \tag{5.18}$$

In general, fringe amplitude normalization and background intensity suppression [66, 67, 147] are performed before fringe demodulation for reliable phase estimation. In the proposed technique, it is essential to perform the background intensity suppression which can be accomplished by a simple high pass filtering of fringe pattern. The background

intensity filtered fringe pattern can be represented as

$$\mathrm{I(x,y)} = \mathrm{b(x,y)}\cos[\phi(\mathrm{x,y}) + \omega_{\mathrm{x}}\mathrm{x}]. \tag{5.19}$$

The proposed method can either be implemented in a row-wise or column-wise manner, depending on the direction of the carrier frequency. Considering the carrier fringes are added in the x-axis direction, the fringe signal in a given row y is expressed as

$$\mathrm{I(x)} = \mathrm{b(x)}\cos[\phi(\mathrm{x}) + \omega_{\mathrm{x}}\mathrm{x}]. \tag{5.20}$$

The complex form of Eq. (5.20) can be represented as

$$\mathrm{I(x)} = \frac{\mathrm{b(x)}}{2}\exp[\mathrm{j}(\phi(\mathrm{x})) + \omega_{\mathrm{x}}\mathrm{x}] + \frac{\mathrm{b(x)}}{2}\exp[-\mathrm{j}(\phi(\mathrm{x})) + \omega_{\mathrm{x}}\mathrm{x}]. \tag{5.21}$$

The autoregressive complex form of the above signal is described in Eqs. (5.6)-(5.10). The state-space representation of this fringe signal model is given in Eqs. (5.11)-(5.13). This state-space formulation allows the simultaneous estimation of phase and carrier frequency.

The state estimation procedure using the AECKF is described in detail in Algorithm 5 below. Here, $\mathbf{s}_{\mathrm{x}}$ is the state estimate; P_{x} is the state covariance matrix; $\mathbb{E}$ represents expectation operation. The superscripts + and – represent a posteriori and a priori estimates of the corresponding variables, respectively; α is the forgetting factor; $\mathbf{Q}_{\mathrm{x}}$ is the system noise covariance; $\mathbf{R}_{\mathrm{x}}$ is the measurement noise covariance; K_{x} is the Kalman gain; arg(·) is the angle of the complex valued argument in radians. We consider $\Phi(\mathrm{x}) = \omega_{\mathrm{x}}\mathrm{x} + \phi(\mathrm{x})$. Since the frequency of the carrier is estimated at the location of each pixel, hence the frequency value with the maximum number of occurrences is evaluated based on the histogram plot of $\hat{\omega}_{\mathrm{x}}(\mathrm{x})$. Subsequently, the sought phase is estimated by removing the carrier fringe contribution ($\hat{\omega}_{\mathrm{x}}(\mathrm{x}) \cdot \mathrm{x}$) from the estimated phase. In this method, the initial value of $\mathbf{R}_0$ is set at first pixel and $\mathbf{R}_{\mathrm{x}}$ is adaptively estimated for subsequent pixels. This is in contrast to the ECKF method wherein the value of $\mathbf{R}_{\mathrm{x}}$ is constant at each pixel. For the computation of current value of $\mathbf{R}_{\mathrm{x}}$, a forgetting factor (α) is used to assign weight to its previous estimate.

Algorithm 5 Phase demodulation using adaptive extended complex Kalman filter

1: Initialization:

$\hat{\mathbf{s}}_0^+ = \mathbb{E}(\mathbf{s}_0)$,

$\mathrm{P}_0^+ = \mathbb{E}[(\mathbf{s}_0 - \hat{\mathbf{s}}_0^+)(\mathbf{s}_0 - \hat{\mathbf{s}}_0^+)^{\mathrm{T}}]$,

2: Prediction:

$\hat{\mathbf{s}}_{\mathrm{x}}^- = \mathrm{f}(\hat{\mathbf{s}}_{\mathrm{x}-1}^+)$,

$\mathrm{P}_{\mathrm{x}}^- = \mathbf{F}_{\mathrm{x}}\mathrm{P}_{\mathrm{x}-1}^+\mathbf{F}_{\mathrm{x}}^{\mathrm{H}} + \mathbf{Q}_{\mathrm{x}}$,

where, $\mathbf{F}_{\mathrm{x}} = \frac{\partial \mathbf{f}(\mathbf{s}_{\mathrm{x}})}{\partial(\mathbf{s}_{\mathrm{x}})} = \begin{bmatrix} 1 & 0 & 0 \\ \hat{\mathbf{s}}_{\mathrm{x}}^-(2) & \hat{\mathbf{s}}_{\mathrm{x}}^-(1) & 0 \\ \frac{\hat{\mathbf{s}}_{\mathrm{x}}^-(3)}{\hat{\mathbf{s}}_{\mathrm{x}}^-(1)^2} & 0 & \frac{1}{\hat{\mathbf{s}}_{\mathrm{x}}^-(1)} \end{bmatrix}$

3: Update:

$\mathrm{d}_{\mathrm{x}} = \mathrm{I}(\mathrm{x}) - \mathbf{H}\hat{\mathbf{s}}_{\mathrm{x}}^-$,

$\mathbf{R}_{\mathrm{x}} = \alpha\mathbf{R}_{\mathrm{x}} + (1-\alpha)\mathbf{H}\mathrm{P}_{\mathrm{x}}^-\mathbf{H}^{\mathrm{T}}$,

$\mathrm{K}_{\mathrm{x}} = \mathrm{P}_{\mathrm{x}}^-\mathbf{H}^{\mathrm{T}}[\mathbf{H}\mathrm{P}_{\mathrm{x}}^-\mathbf{H}^{\mathrm{T}} + \mathbf{R}_{\mathrm{x}}]$,

$\hat{\mathbf{s}}_{\mathrm{x}}^+ = \hat{\mathbf{s}}_{\mathrm{x}}^- + \mathrm{K}_{\mathrm{x}}(\mathrm{d}_{\mathrm{x}})$,

$\mathrm{e}_{\mathrm{x}} = \mathrm{I}(\mathrm{x}) - \mathbf{H}\hat{\mathbf{s}}_{\mathrm{x}}^+$,

$\mathbf{R}_{\mathrm{x}} = \alpha\mathbf{R}_{\mathrm{x}} + (1-\alpha)(\mathrm{e}_{\mathrm{x}}\mathrm{e}_{\mathrm{x}}^{\mathrm{T}} + \mathbf{H}\mathrm{P}_{\mathrm{x}}^-\mathbf{H}^{\mathrm{T}})$,

$\mathrm{K}_{\mathrm{x}} = \mathrm{P}_{\mathrm{x}}^-\mathbf{H}^{\mathrm{T}}[\mathbf{H}\mathrm{P}_{\mathrm{x}}^-\mathbf{H}^{\mathrm{T}} + \mathbf{R}_{\mathrm{x}}]$,

$\hat{\mathbf{s}}_{\mathrm{x}}^+ = \hat{\mathbf{s}}_{\mathrm{x}}^- + \mathrm{K}_{\mathrm{x}}(\mathrm{d}_{\mathrm{x}})$,

$\mathrm{P}_{\mathrm{x}}^+ = \mathrm{P}_{\mathrm{x}}^- - \mathrm{K}_{\mathrm{x}}\mathbf{H}\mathrm{P}_{\mathrm{x}}^-$,

4: Estimated phase with carrier and the carrier frequency:

$\hat{\Phi}(\mathrm{x}) = \arg[\hat{\mathbf{s}}_{\mathrm{x}}^+(2)]$,

$\hat{\omega}_{\mathrm{x}}(\mathrm{x}) = \arg[\hat{\mathbf{s}}_{\mathrm{x}}^+(1)]$

5: Estimated phase after carrier removal:

$\hat{\phi}(\mathrm{x}) = \arg\{\exp[\mathrm{j}(\hat{\Phi}(\mathrm{x}) - \hat{\omega}_{\mathrm{x}}(\mathrm{x}).\mathrm{x}]\}$

5.2.2 Results

Simulation

A computer-generated fringe pattern of size 256×256 is used to demonstrate the performance of AECKF algorithm and its comparison with the ECKF method. The simulation

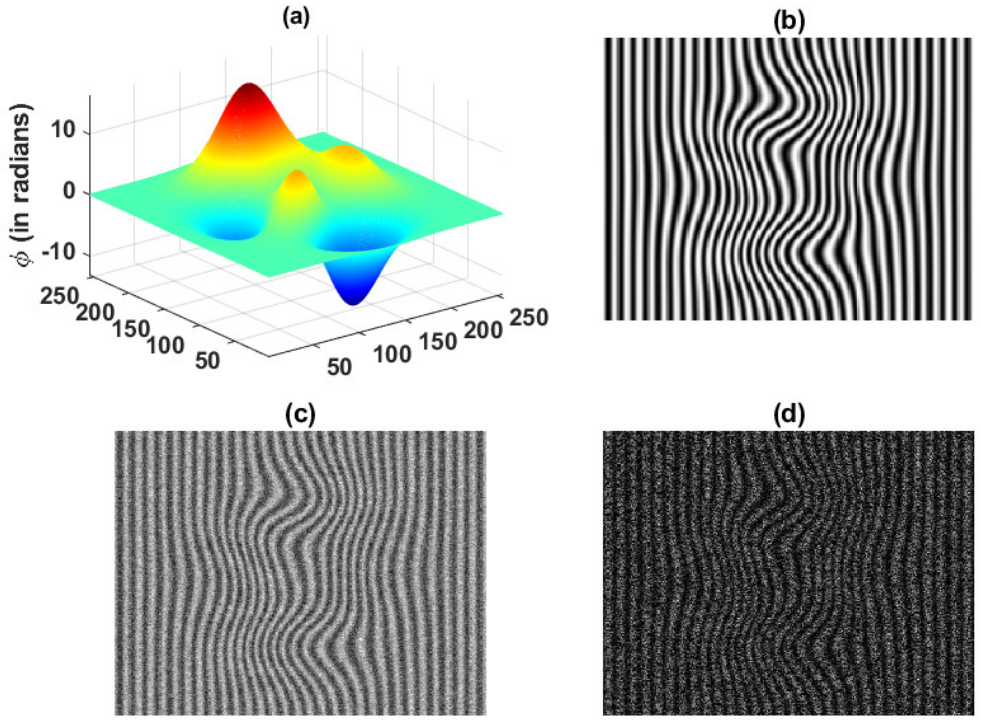

FIGURE 5.7: Simulation example: (a) phase (b) carrier fringe pattern modulated by the phase. Fringe patterns corrupted with (c) additive noise at SNR= 5 dB, and (d) speckle noise [5].

is carried out using the MATLAB software, with simulated phase and carrier fringe frequency given as

$$\phi = \mathrm{k} \times \mathrm{peaks(K)}, \tag{5.22}$$

$$\omega_{\mathrm{x}} = \mathrm{m} \times \frac{2\pi}{\mathrm{K}}, \tag{5.23}$$

where, 'peaks' is the inbuilt function in MATLAB; k is the scaling factor; Figure 5.7(a) shows the three-dimensional representation of simulated phase with k = 2. The carrier modulated fringe pattern with the frequency parameter m = 30 is exhibited in Fig. 5.7(b). Further, Figs. 5.7(c) and 5.7(d) represent the fringe patterns simulated with additive noise at SNR= 5 dB and speckle noise, respectively. The algorithm parameters used in the implementation of phase demodulation are shown in Table 5.2. The phase estimates including the carrier frequency contribution were computed using the ECKF and the AECKF method for the noisy fringe pattern in Fig. 5.7(c) as shown in Figs.

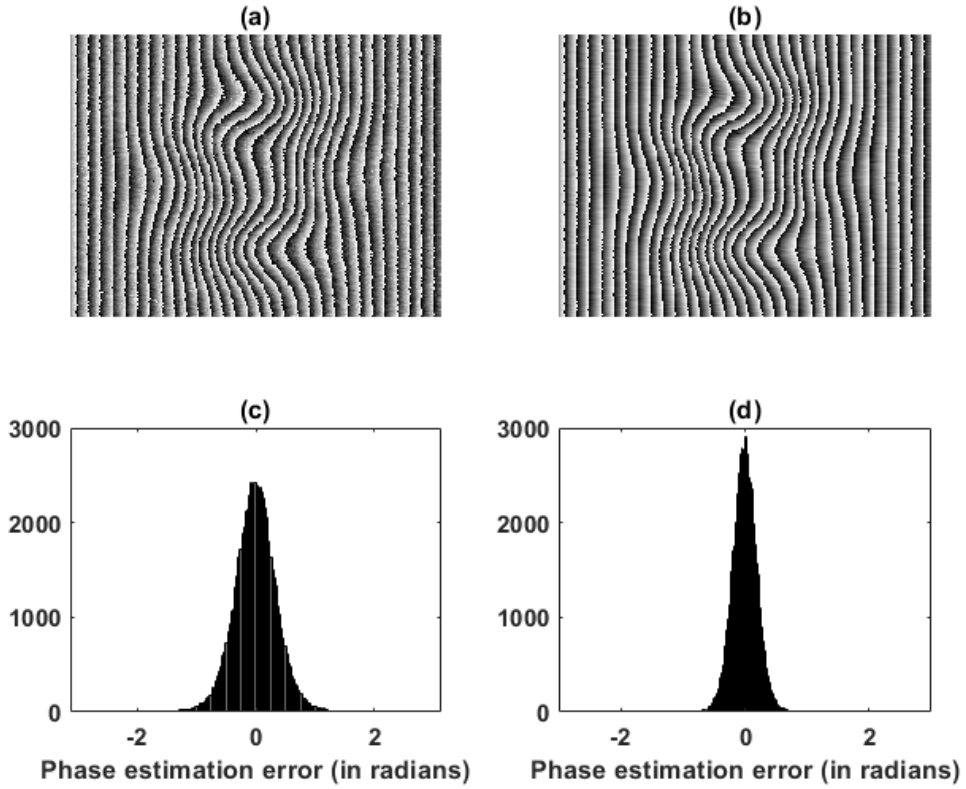

FIGURE 5.8: Estimated phase with carrier frequency for the noisy fringe pattern is shown in Fig. 5.7 (c) using the (a) ECKF, and (b) AECKF method; associated histogram plot of the phase error using the (c) ECKF, and (d) AECKF methods [5].

5.8(a) and 5.8(b), respectively. The histogram plots of corresponding phase error are shown in Figure 5.8(c) and 5.8(d), respectively.

TABLE 5.2: Algorithm parameters used in simulation and experimental results for the phase demodulation.

Methods	**Algorithm parameters**
FT[145]	Frequency domain masking half plane.
WFT[75]	$\alpha = 10, \omega_{\mathrm{xl}} = -1, \omega_{\mathrm{xt}} = 0.1, \omega_{\mathrm{xh}} = 1, \omega_{\mathrm{yl}} = -1, \omega_{\mathrm{yt}} = 0.1, \omega_{\mathrm{yh}} = 1, \mathrm{thr} = 0.5.$
ECKF[4]	$\hat{\mathbf{s}}_0^+ = [\exp(\mathrm{j}\pi/5); \exp(\mathrm{j}\pi/5); \exp(\mathrm{j}\pi/5)], \hat{\mathrm{P}}_0^+ = \mathrm{diag}([1; 100; 100]).$
	$\mathbf{Q}_{\mathrm{x}} = \mathrm{diag}([0.01; 100; 100]), \mathbf{R}_{\mathrm{x}} = 10.$
AECKF	$\hat{\mathbf{s}}_0^+ = [\exp(\mathrm{j}\pi/5); \exp(\mathrm{j}\pi/5); \exp(\mathrm{j}\pi/5)], \hat{\mathrm{P}}_0^+ = \mathrm{diag}([1; 100; 100]).$
	$\mathbf{Q}_{\mathrm{x}} = \mathrm{diag}([0.01; 100; 100]), \mathbf{R}_0 = 1, \alpha = 0.5.$

Similarly, Figs. 5.9(a) and 5.9(b) show the phase estimates obtained from the speckle

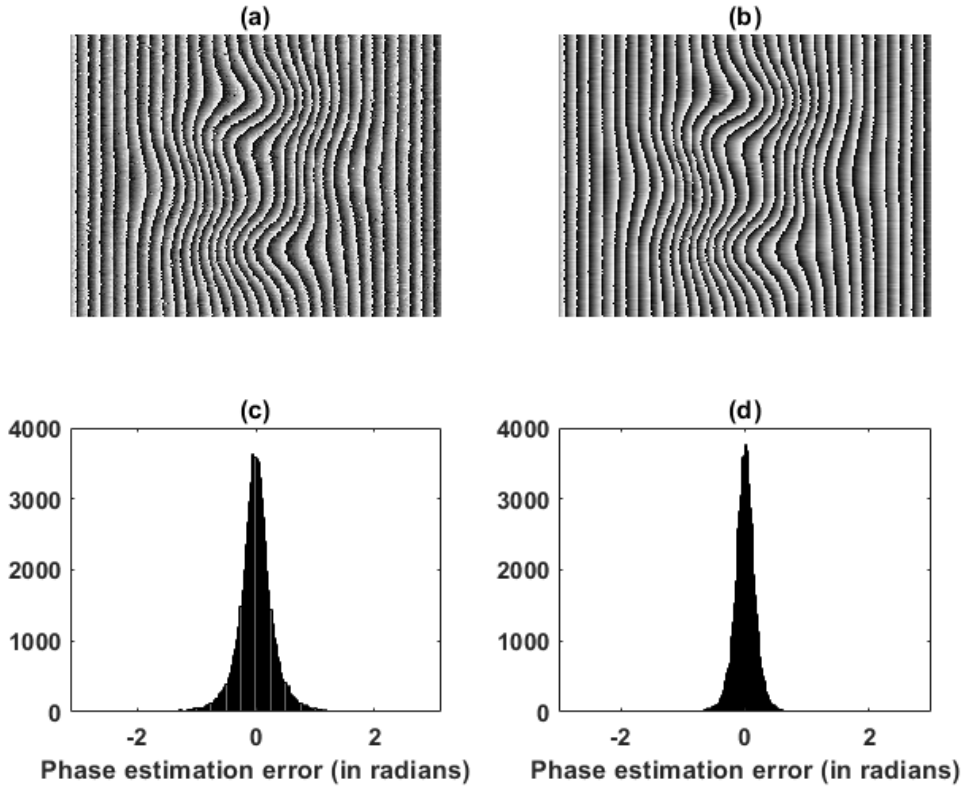

FIGURE 5.9: Estimated phase with carrier frequency for the noisy fringe pattern shown in Figure 5.7 (d) using (a) ECKF, and (b) AECKF method; associated histogram plot of the phase error using (c) ECKF, and (d) AECKF method [5].

noise corrupted fringe pattern given in Fig. 5.7(d) using the ECKF, and AECKF, respectively. The histogram plots of corresponding estimation errors are shown in Figs. 5.9(c) and 5.9(d), respectively, which clearly indicate the improved phase estimation performance of the AECKF method over the ECKF method in the presence of noise. Further for the purpose of illustration, the phase estimate errors computed with the AECKF and ECKF methods along the 128^{th} row of the fringe pattern corrupted with additive and speckle noise are shown in Figs. 5.10(a) and 5.10(b), respectively. It is evident from these error plots that the AECKF method is robust against the heavy noise sources. The quantitative performance comparison of the fringe demodulation techniques is provided based on RMSE analysis.

Figure 5.11(a) shows the RMSEs computed in function of signal-to-noise-ratio (SNR) (in dB) for $k = 2$ and $m = 30$. The plot in Figure 5.11(b), 5.11(c) and 5.11(d) corresponds to the RMSEs in the function of carrier frequency for different fringe density set as $k = 1, 2, 3$, respectively. From these results, it can be concluded that the proposed

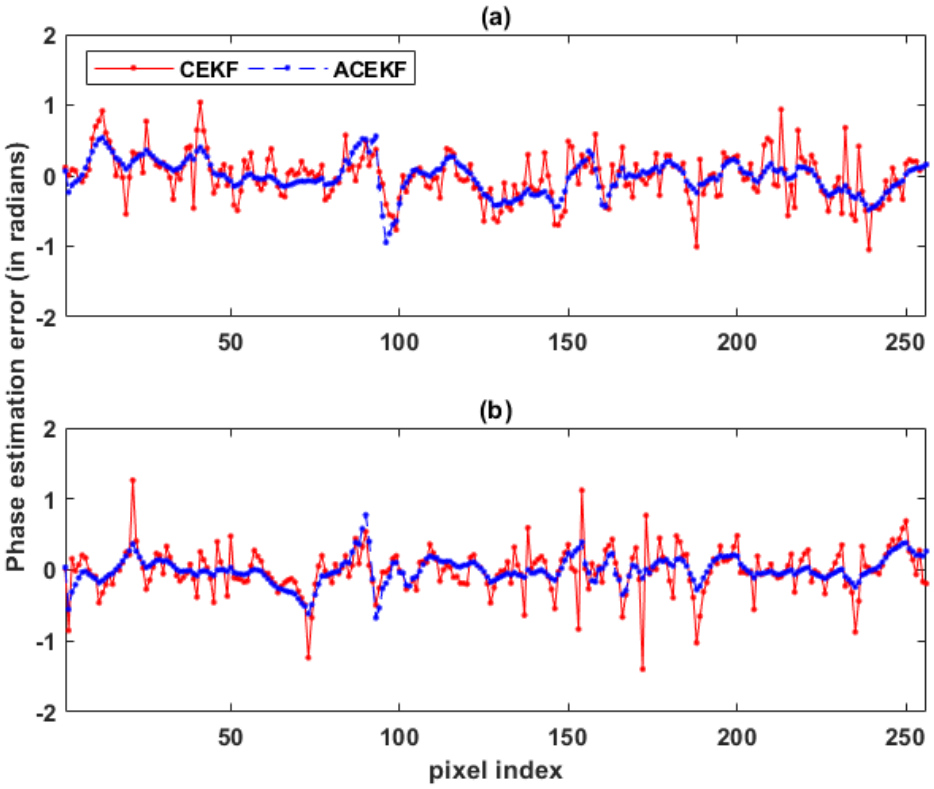

FIGURE 5.10: Phase estimation error plot at y= 128^{th} of the fringe pattern corrupted with (a) additive noise and (b) speckle noise [5].

algorithm provides good phase estimation performance at low SNR and is independent of carrier frequency. As mentioned earlier, since the proposed method can estimate the carrier frequency along with the phase, its contribution can be removed from the estimated phase. Figures 5.12(a) and 5.12(b) show the estimated phase without the carrier frequency contribution using the proposed AECKF method for the additive and speckle noise, respectively.

Experiment

The applicability of the proposed method was validated with an experimentally recorded carrier modulated fringe pattern of the size 768×576 pixels as exhibited in Fig. 5.13(a) recorded in a holographic interferometry setup. Figure 5.13(b) shows the denoised fringe pattern obtained with simple low pass filtering. The fringe pattern intensity is divided by its maximum value to limit the fringe intensity variations in the range of [-1,1]. Figures 5.13(c), 5.13(d), 5.13(e) and 5.13(f) show the estimated phase computed using FT,

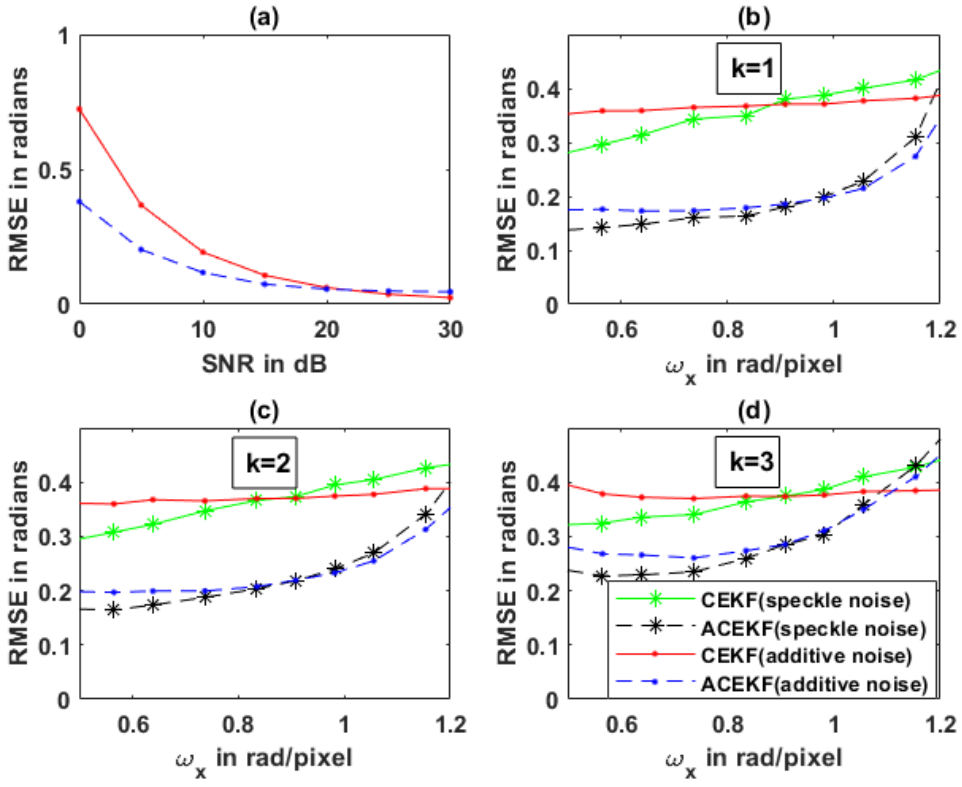

FIGURE 5.11: RMSEs plot of the estimated phase in respect of different (a) SNR with k=2 and m=30, (b) carrier frequency with k=1, (c) carrier frequency with k=2, and (d) carrier frequency with k=3 [5].

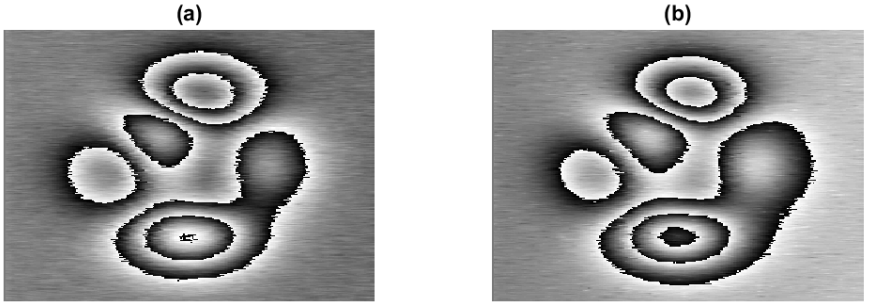

FIGURE 5.12: Extracted phase without carrier frequency contribution obtained using the proposed AECKF method for (a) additive noise and (b) speckle noise corrupted fringe pattern [5].

WFT, ECKF and the proposed AECKF method,respectively. Figures 5.13(g) shows the estimated phase computed using the proposed AECKF method without carrier frequency contribution. The algorithm parameters used in the implementation of phase demodulation are shown in Table 5.2.

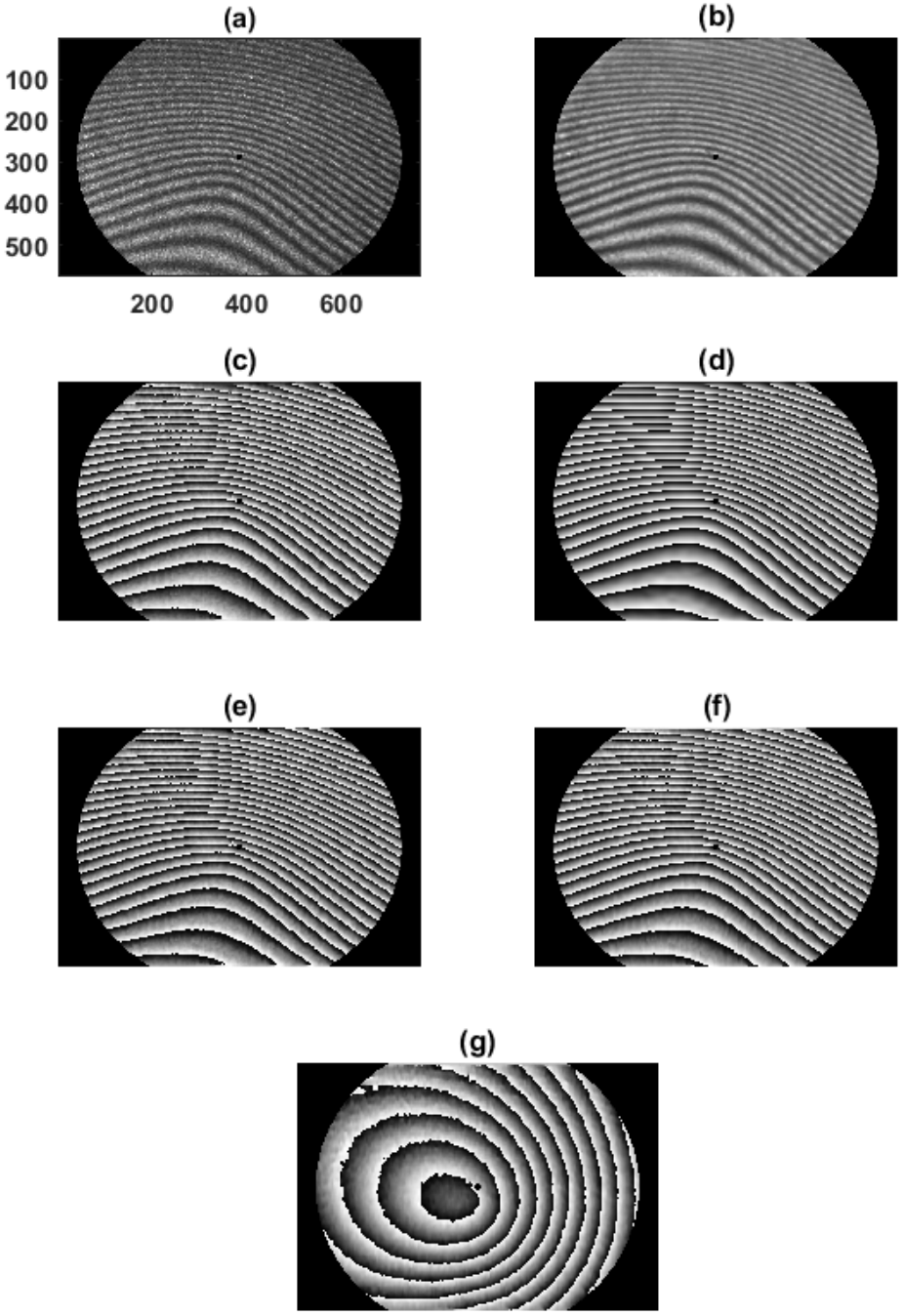

FIGURE 5.13: (a) Experimentally recorded carrier modulated fringe pattern, (b) amplitude normalized fringe pattern; estimated phase obtained using (c) FT, (d) WFT, and (e) ECKF; estimated phase obtained using proposed AECKF method (f) with and (g) without carrier frequency contribution. [5].

5.2.3 Conclusion

In this work, phase demodulation is performed using an adaptive extended complex Kalman filter algorithm. The simulated results qualitatively and quantitatively demonstrate the improved performance offered by the AECKF method over the ECKF. This

improvement is achieved by adaptively estimating the value of measurement noise covariance at each pixel. It makes the algorithm robust against the additive and speckle noise. The proposed algorithm can simultaneously estimate the phase and carrier frequency, which helps to extract the phase without the carrier fringe contribution. The feasibility of the proposed method is also validated with the experimental data.

5.3 Carrier Fringe Pattern Demodulation using Extended Kalman filter

In the previous work of phase demodulation using the ECKF and AECKF, a preprocessing step is performed prior to the phase demodulation. In this section, the extended Kalman filter based method is utilized for the fringe demodulation. This method does not require such preprocessing steps prior to demodulation. In this work a spatial carrier fringe demodulation technique is proposed based on state space modelling approach for the phase estimation. The fringe background intensity, the carrier frequency and phase quadrature components are considered to be the elements of state vector which are estimated simultaneously. The state estimation is performed using the extended Kalman filter.

5.3.1 Carrier Fringe Pattern Demodulation

The intensity distribution of carrier modulated fringe pattern in a given row y can be represented as

$$\mathrm{I(x)} = \mathrm{a(x)} + \mathrm{b(x)}\cos(\phi(\mathrm{x}) + \omega_{\mathrm{x}}\mathrm{x}) \tag{5.24}$$

where, ω_{x} represents the carrier fringe frequency along x-direction; ϕ represents the carrier modulating phase of interest. Let $\theta(\mathrm{x},\mathrm{y}) = \phi(\mathrm{x},\mathrm{y}) + \omega_{\mathrm{x}}\mathrm{x}$. Since the carrier is added along the x-direction, the fringe demodulation is performed in a row-wise manner. The state vector of size 4×1 at x of the proposed model is defined as [148]

$$\mathbf{s}_{\mathrm{x}} = \begin{bmatrix} \mathrm{a(x)} & \omega_{\mathrm{x}} & \mathrm{b(x)}\cos(\theta(\mathrm{x})) & \mathrm{b(x)}\sin(\theta(\mathrm{x})) \end{bmatrix}^{\mathrm{T}} \tag{5.25}$$

where, $(\cdot)^{\mathrm{T}}$ represents the transpose operation. The process and the measurement model is given as

$$\mathbf{s}_{\mathrm{x}} = \mathbf{f}(\mathbf{s}_{\mathrm{x}-1}) + \mathbf{w}_{\mathrm{x}} \tag{5.26}$$

$$\mathrm{I}(\mathrm{x}) = \mathbf{h}(\mathbf{s}_{\mathrm{x}}) + \mathbf{v}_{\mathrm{x}} \tag{5.27}$$

where, $\mathbf{w}_{\mathrm{x}}$ and $\mathbf{v}_{\mathrm{x}}$ represent the process noise and measurement noise vector of size 4×1 and 1×1, respectively. The $\mathbf{f}(\mathbf{s}_{\mathrm{x}})$ in Eq. (5.26) and $\mathbf{h}(\mathbf{s}_{\mathrm{x}})$ in Eq. (5.27) are

$$\mathbf{f}(\mathbf{s}_{\mathrm{x}}) = \begin{bmatrix} \mathbf{s}_{\mathrm{x}}(1) \\ \mathbf{s}_{\mathrm{x}}(2) \\ \mathbf{s}_{\mathrm{x}}(3)\cos[\mathbf{s}_{\mathrm{x}}(2)] - \mathbf{s}_{\mathrm{x}}(4)\sin[\mathbf{s}_{\mathrm{x}}(2)], \\ \mathbf{s}_{\mathrm{x}}(3)\sin[\mathbf{s}_{\mathrm{x}}(2)] + \mathbf{s}_{\mathrm{x}}(4)\cos[\mathbf{s}_{\mathrm{x}}(2)] \end{bmatrix} \tag{5.28}$$

$$\mathbf{h}(\mathbf{s}_{\mathrm{x}}) = \mathbf{s}_{\mathrm{x}}(1) + \mathbf{s}_{\mathrm{x}}(3) \tag{5.29}$$

The main objective of the proposed algorithm is to estimate the phase from the fringe intensity measurement. The state-space modeling described in Eqs. (5.25)-(5.29) allows the simultaneous estimation of background intensity, local carrier frequency and amplitude-modulated in-phase and quadrature components. The pixel-wise operation in the proposed method avoids the estimation errors at the valid fringe region boundaries. It can be noted from Eq. (5.26) that the process update is a nonlinear function of the state vector. Consequently, the EKF algorithm is employed for the state estimation. The EKF is a non-linear filter which updates the mean and covariance estimates of the state vector in two steps. The first step is called prediction wherein the state vector is updated using a process model (Eqs. (5.26) and (5.28)). In the second step, the state vector is updated using the available measurements through a measurement model (Eqs. (5.27) and (5.29)). Basically, the EKF linearizes the prediction and/or measurement models around the current mean and covariance estimates of the state vector. It can be noted that appropriate selection of the state vector and the process and measurement models is crucial for the fringe pattern demodulation. Based on the above model, the EKF-based for the state estimation procedure [121] is described in Algorithm 6.

Algorithm 6 Fringe demodulation using extended Kalman filter

1: Initialize the state vector estimate and its error covariance matrix P as

$\hat{\mathbf{s}}_0^+ = \mathbb{E}(\mathbf{s}_0)$,

$\mathbf{P}_0^+ = \mathbb{E}[(\mathbf{s}_0 - \hat{\mathbf{s}}_0^+)(\mathbf{s}_0 - \hat{\mathbf{s}}_0^+)^{\mathrm{T}}]$,

where, $\mathbb{E}$ represents the expectation operator. The superscripts – and + indicate the a priori and a posteriori estimates.

2: Update equation for a priori state estimation at x= 1,2, $\cdots$ is given as

$\hat{\mathbf{s}}_{\mathrm{x}}^- = \mathbf{F}_{\mathrm{x}}\hat{\mathbf{s}}_{\mathrm{x-1}}^+$,

$\mathbf{P}_{\mathrm{x}}^- = \mathbf{F}_{\mathrm{x}}\mathbf{P}_{\mathrm{x-1}}^+\mathbf{F}_{\mathrm{x}}^{\mathrm{T}} + \mathbf{Q}_{\mathrm{x}}$,

where $\mathbf{Q}_{\mathrm{x}}$ represents the process noise covariance of size 4×4 and the process state update matrix ($\mathbf{F}_{\mathrm{x}}$) of size 4×4 is evaluated as

$$\mathbf{F}_{\mathrm{x}} = \frac{\partial \mathrm{f}(\mathbf{s}_{\mathrm{x}})}{\partial \mathbf{s}_{\mathrm{x}}} = \begin{bmatrix} 1 & 0 & 0 & 0 \\ 0 & 1 & 0 & 0 \\ 0 & \mathrm{L}_0 & \cos[\hat{\mathbf{s}}_{\mathrm{x}}(2)] & -\sin[\hat{\mathbf{s}}_{\mathrm{x}}(2)] \\ 0 & \mathrm{L}_1 & \sin[\hat{\mathbf{s}}_{\mathrm{x}}(2) & \cos[\hat{\mathbf{s}}_{\mathrm{x}}(2)] \end{bmatrix}$$

where, $\mathrm{L}_0 = -\hat{\mathbf{s}}_{\mathrm{x}}(3)\sin[\hat{\mathbf{s}}_{\mathrm{x}}(2)] - \hat{\mathbf{s}}_{\mathrm{x}}(4)\cos[\hat{\mathbf{s}}_{\mathrm{x}}(2)]$, $\mathrm{L}_1 = \hat{\mathbf{s}}_{\mathrm{x}}(3)\cos[\hat{\mathbf{s}}_{\mathrm{x}}(2)] - \hat{\mathbf{s}}_{\mathrm{x}}(4)\sin[\hat{\mathbf{s}}_{\mathrm{x}}(2)]$.

3: The fringe intensity estimate can be calculated using the state estimate as

$\hat{\mathrm{I}}(\mathrm{x}) = \mathbf{E}_{\mathrm{x}}\hat{\mathbf{s}}_{\mathrm{x}}^-$,

where

$\mathbf{E}_{\mathbf{x}} = \frac{\partial \mathrm{h}(\mathbf{s}_{\mathrm{x}})}{\partial \mathbf{s}_{\mathrm{x}}} = \begin{bmatrix} 1 & 0 & 1 & 0 \end{bmatrix}$,

4: In this method, the measurement error variance R_{x} is adaptively estimated at each pixel [130]. Accordingly, the measurement updates of state and error covariance are evaluated as

$\mathbf{R}_{\mathrm{x}} = \alpha\mathbf{R}_{\mathrm{x-1}} + (1-\alpha)\mathbf{E}_{\mathrm{x}}\mathbf{P}_{\mathrm{x}}^-\mathbf{E}_{\mathrm{x}}^{\mathrm{T}}$

where the value of α is set to 0.5.

5: Kalman gain is calculated as

$\mathbf{K}_{\mathrm{x}} = \mathbf{P}_{\mathrm{x}}^-\mathbf{E}_{\mathrm{x}}^{\mathrm{T}}(\mathbf{E}_{\mathrm{x}}\mathbf{P}_{\mathrm{x}}^-\mathbf{E}_{\mathrm{x}}^{\mathrm{T}} + \mathbf{R}_{\mathrm{x}})^{-1}$,

6: A posterior state estimates are obtained by taking the measurement of fringe intensity into account as

$\hat{\mathbf{s}}_{\mathrm{x}}^+ = \hat{\mathbf{s}}_{\mathrm{x}}^- + \mathbf{K}_{\mathrm{x}}(\mathbf{I}(\mathrm{x}) - \hat{\mathbf{I}}(\mathrm{x}))$,

$\mathbf{P}_{\mathrm{x}}^+ = (\mathbf{I} - \mathbf{K}_{\mathrm{x}}\mathbf{E}_{\mathrm{x}})\mathbf{P}_{\mathrm{x}}^-(\mathbf{I} - \mathbf{K}_{\mathrm{x}}\mathbf{E}_{\mathrm{x}})^{\mathrm{T}} + \mathbf{K}_{\mathrm{x}}\mathrm{R}_{\mathrm{x}}\mathbf{K}_{\mathrm{x}}^{\mathrm{T}}$,

7: The performance of the state estimation can be further improved by utilizing Rauch–Tung–Striebel smoother algorithm which involves the backward filtering operation. Accordingly, the state and its error covariance estimates are initialized at $\mathrm{x} = \mathrm{K} - 1$ as

$\hat{\mathbf{s}}_{\mathrm{K-1}}^{(\mathrm{b})} = \hat{\mathbf{s}}_{\mathrm{K-1}}^+$, $\mathbf{P}_{\mathrm{K-1}}^{(\mathrm{b})} = \mathbf{P}_{\mathrm{K-1}}^+$,

8: Following steps are implemented for $\mathrm{x} = \mathrm{K} - 2, \cdots, 0$

$\mathbf{G}_{\mathrm{x}}^{(\mathrm{b})} = \mathbf{P}_{\mathrm{x}}^+\mathbf{F}_{\mathrm{x+1}}^{\mathrm{T}}\left(\mathbf{P}_{\mathrm{x+1}}^-\right)^{-1}$,

$\mathbf{P}_{\mathrm{x}}^{(\mathrm{b})} = \mathbf{P}_{\mathrm{x}}^+ - \mathbf{G}_{\mathrm{x}}^{(\mathrm{b})}\left(\mathbf{P}_{\mathrm{x+1}}^- - \mathbf{P}_{\mathrm{x+1}}^{(\mathrm{b})}\right)(\mathbf{G}_{\mathrm{x}}^{(\mathrm{b})})^{\mathrm{T}}$,

$\hat{\mathbf{s}}_{\mathrm{x}}^{(\mathrm{b})} = \hat{\mathbf{s}}_{\mathrm{x}}^+ + \mathbf{G}_{\mathrm{x}}^{(\mathrm{b})}\left(\hat{\mathbf{s}}_{\mathrm{x+1}}^{(\mathrm{b})} - \hat{\mathbf{s}}_{\mathrm{x+1}}^-\right)$.

9: The estimates are represented as

$\hat{a}(x) = \hat{s}_x^{(b)}(1)$,

$\hat{\omega}_x(x) = \hat{s}_x^{(b)}(2)$,

$\hat{b}\cos(\hat{\theta}(x)) = \hat{s}_x^{(b)}(3)$,

$\hat{b}\sin(\hat{\theta}(x)) = \hat{s}_x^{(b)}(4)$,

where, $\hat{a}$, $\hat{\omega}_x$ and $\hat{\theta}(x) = \hat{\phi}(x) + \hat{\omega}_x x$ represent the estimated background intensity, estimated frequency of carrier fringes and estimated phase with carrier frequency, respectively.

10: The phase estimate at x with and without carrier fringe contribution as

$\hat{\theta}(x) = \tan^{-1}\left[\frac{\hat{s}_x^{(b)}(4)}{\hat{s}_x^{(b)}(3)}\right]$,

$\hat{\phi}(x) = \mathcal{W}\{\hat{\theta}(x) - \hat{\omega}_x(x) \cdot x\}$,

The described procedure in the algorithm is repeated for all $y = [0, L-1]$ to obtain the two-dimensional phase estimate. The flow chart of the proposed algorithm is shown in Fig. 5.14.

5.3.2 Results

Simulation

The performance of the proposed method is numerically evaluated with a simulated fringe pattern of size 400×400. The phase ϕ is simulated using the '*peaks*' function available in MATLAB, scaled by a factor of m. Considering the carrier frequency as $\omega_x = 2\pi n/L$, the simulated phase with carrier (θ) can be given as

$$\theta(x, y) = m \cdot \phi(x, y) + \omega_x \cdot x, \tag{5.30}$$

Figure 5.15(a) shows the simulated phase (ϕ) with $m = 4$. The corresponding wrapped phase is shown in Fig. 5.15(b). A fringe pattern (I) was generated with the simulated phase and $n = 40$ as shown in Fig. 5.15(c). The background intensity and fringe

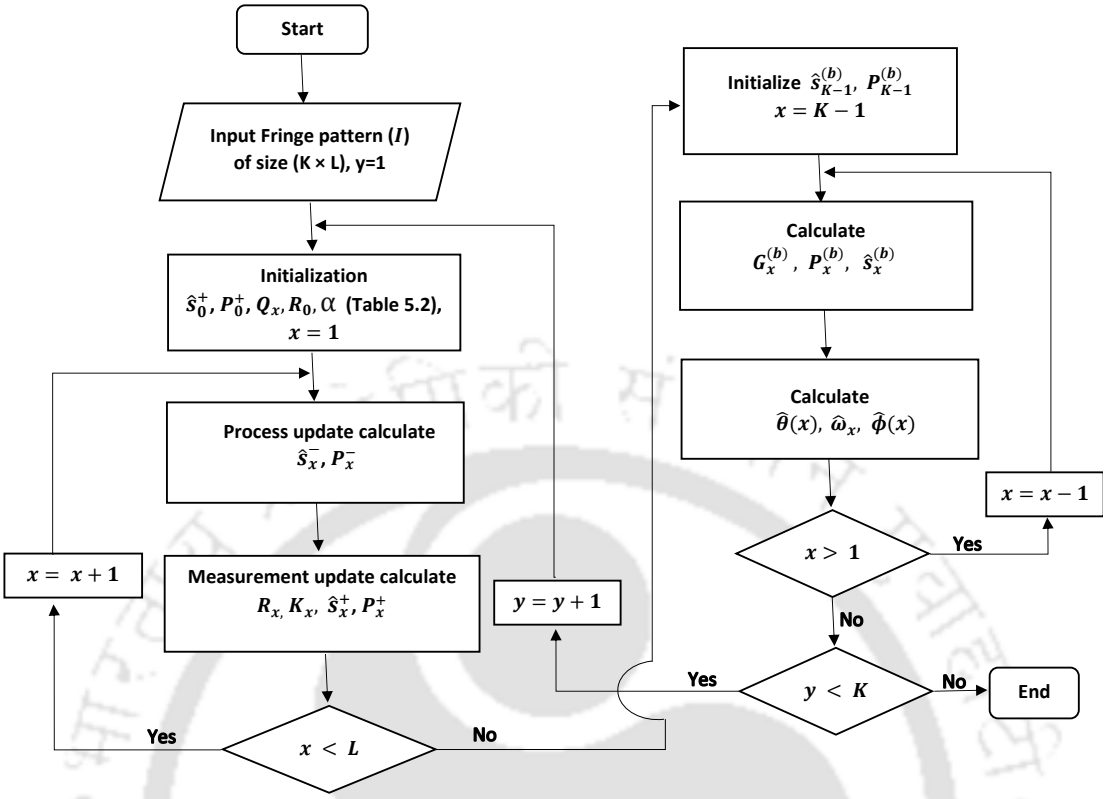

FIGURE 5.14: Flow Chart of the proposed EKF based algorithm for the fringe pattern demodulation [6].

amplitude were simulated as

$$a(x, y) = 0.9 \cdot \exp\{-30[(x-200)^2 + (y-200)^2]/400^2\}, \tag{5.31}$$

$$b(x, y) = \exp\{-30[(x-200)^2 + (y-200)^2]/400^2\}. \tag{5.32}$$

Figure 5.15(d) shows the phase (θ) in the wrapped form. Figures 5.16(a), 5.16(b), 5.16(c) and 5.16(d) show the wrapped phase estimates ($\hat{\theta}$) obtained at signal-to-noise ratio (SNR) of 20 dB using the FT, WFT, ECKF, and EKF methods, respectively. High pass filtering of the fringe pattern was performed to remove the background intensity as required in the implementation of ECKF method. The low fringe density regions within the dotted colored boxes in the first row of Fig. 5.16 are shown separately in the second row. It can be noted that phase estimation accuracy was affected in the low fringe density region in the case of WFT method. It was caused mainly due to the parameter values selected in its implementation. The algorithm parameters used in the implementation of fringe

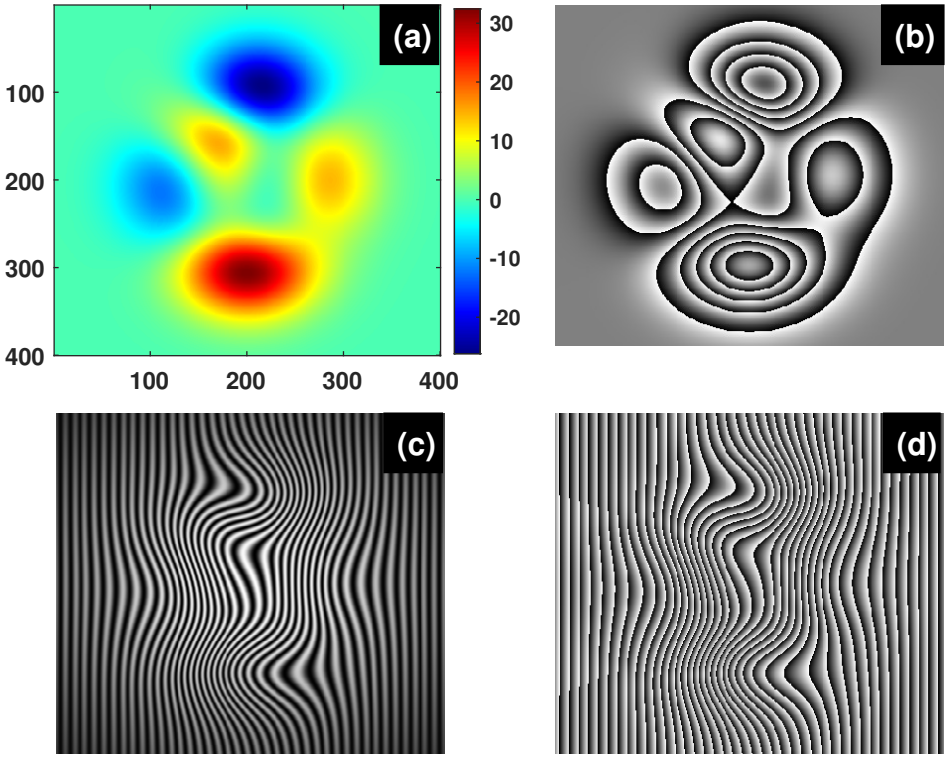

FIGURE 5.15: (a) Absolute and (b) wrapped forms of simulated phase (ϕ). (c) Carrier modulated fringe pattern (I) and (d) wrapped form of simulated phase with carrier phase contribution (θ). The phase values are in radians [6].

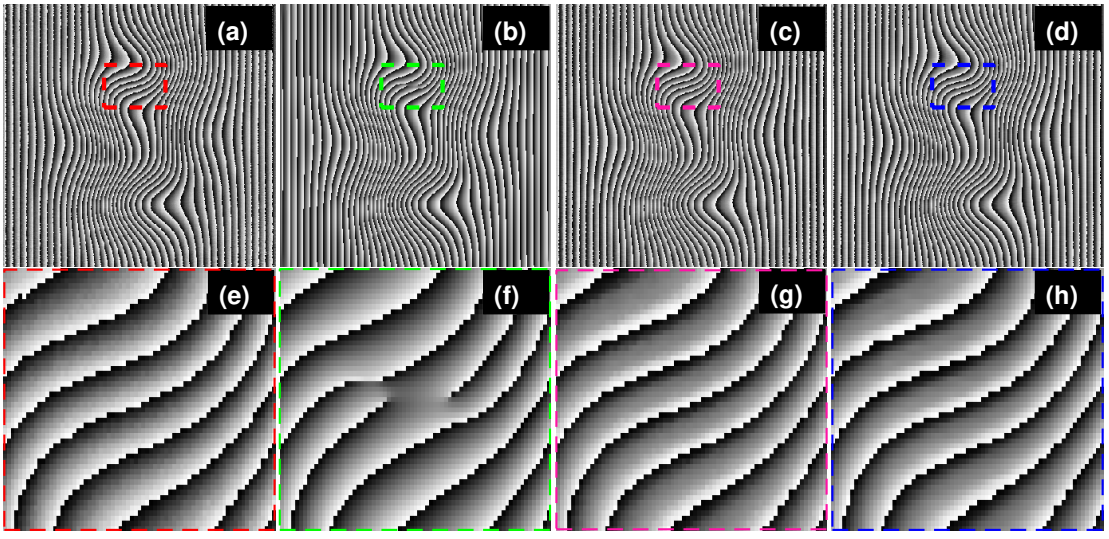

FIGURE 5.16: Estimated phase obtained from the simulated fringe pattern shown in Fig. 5.15(c) with SNR = 20 dB using the (a) FT, (b) WFT, (c) ECKF, and (d) EKF methods. Estimated phases over the region within the (e) red, (f) green, (g) pink, and (h) blue boxes [6].

demodulation algorithms are given in Table 5.3. The FT and WFT algorithm parameters in Table 5.3 affect the phase estimation accuracy. On the other hand, it is important to note that the proposed EKF method algorithm parameters are used for the purpose of initialization only. These values are chosen based on the knowledge of commonly recorded fringe patterns as priors to the proposed algorithm. Therefore, variation is the parameter values do not have significant impact on the performance of the phase estimation. Even if the state estimate prior is initialized away from its true values, the posterior estimate will eventually get closer to the true value. The convergence rate depends on the value of R_0 which is set depending on the noise strength. As a result, the state estimate at some of the initial pixels contains error which is effectively reduced during the backward filtering step. The histograms of phase estimation errors are shown in Fig. 5.17.

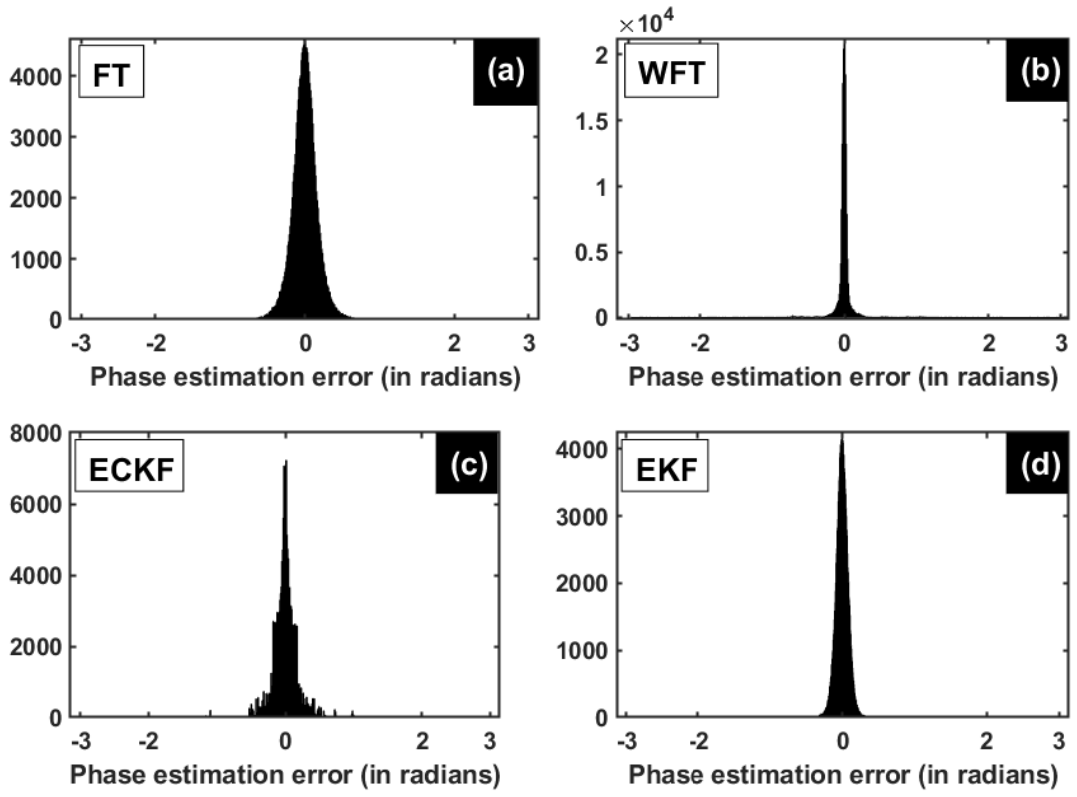

FIGURE 5.17: The histograms of errors in the phase estimation obtained using the (a) FT, (b) WFT, (c) ECKF, and (d) EKF methods [6].

A quantitative performance comparison between the fringe demodulation algorithms was performed using RMSEs and peak-to-valley (PV) errors as a function of m, n and SNR.

Methods	**Algorithm parameters**
FT[73]	Half plane filtering of Fourier spectrum of fringe pattern
WFT[75]	σ = 10 ,[ωxl, ωyl]=[-0.5,0.2], [ωxh, ωyh]=[0.5,1.8], ωxi=0.1, ωyi=0.1, Thr = 1.
ECKF[149]	$\hat{\mathbf{s}}_0^+ = [\exp[\mathrm{j}(\pi/5)]; \exp[\mathrm{j}(\pi/5)]; \exp[-\mathrm{j}(\pi/5)]]$, $\mathbf{P}_0^+ = \mathrm{diag}([1; 10^2; 10^2])$, $\mathbf{Q}_\mathrm{x} = \mathrm{diag}([0.01; 10^2; 10^2])$, $\mathrm{R_x} = 10$.
EKF	$\mathbf{P}_0^+ = \mathrm{diag}([10^{-2}; 10^{-2}; 10^2; 10^2])$, $\mathbf{Q}_\mathrm{x} = \mathrm{diag}([10; 10^{-4}; 10^3; 10^3])$, $\mathrm{R}_0 = 1; \alpha = 0.5$, $\mathrm{b} = (\max(\mathrm{I}) - \min(\mathrm{I}))/2$, $\hat{\mathbf{s}}_0^+ = [\mathrm{mean(I)}; \pi/5; \mathrm{b}\cos(\pi/6 + \pi/5); \mathrm{b}\sin(\pi/6 + \pi/5)]$.

TABLE 5.3: Fringe pattern demodulation algorithm parameters.

The RMSE and PV are defined as

$$\mathrm{RMSE} = \sqrt{\frac{1}{\mathrm{L}}\sum_{\mathrm{n}=1}^{\mathrm{L}}\left(\theta(\mathrm{n}) - \hat{\theta}(\mathrm{n})\right)^2}, \tag{5.33}$$

$$\mathrm{PV} = \max\left(\theta - \hat{\theta}\right) - \min(\theta - \hat{\theta}), \tag{5.34}$$

where, θ and $\hat{\theta}$ represent the true phase and the estimated phase, respectively; L represents number of pixels in the valid fringe region. The RMSEs evaluated as a function of carrier frequency are plotted in Figs. 5.18(a) and 5.18(b) for m = 2 and m = 4, respectively. In both cases, the phase estimation accuracy of the proposed EKF based method was found to be higher than the FT, WFT and ECKF methods. Figures 5.18(c-d) and 5.18(e-f) show the RMSEs and PVs plotted as function of SNR with n = 40 and m = 2 and m = 4, respectively. The error values were calculated as an average of ten simulation runs at each SNR. It can be noted that the proposed method is found to be more noise robust compared the FT, WFT and ECKF methods in both cases. The computation time taken by the fringe demodulation methods are reported in Table 5.4. The computational complexity of the proposed algorithm depends on the size of fringe pattern only. Since the phase estimation is performed row-wise/column-wise manner, the computational resource requirement is less. The computation time increases with the increase in the size of fringe pattern. On the other hand, the computation time required for the WFT method depends on the algorithm parameter values. In that case, the reduction in computation time may result in the deterioration of phase estimation accuracy.

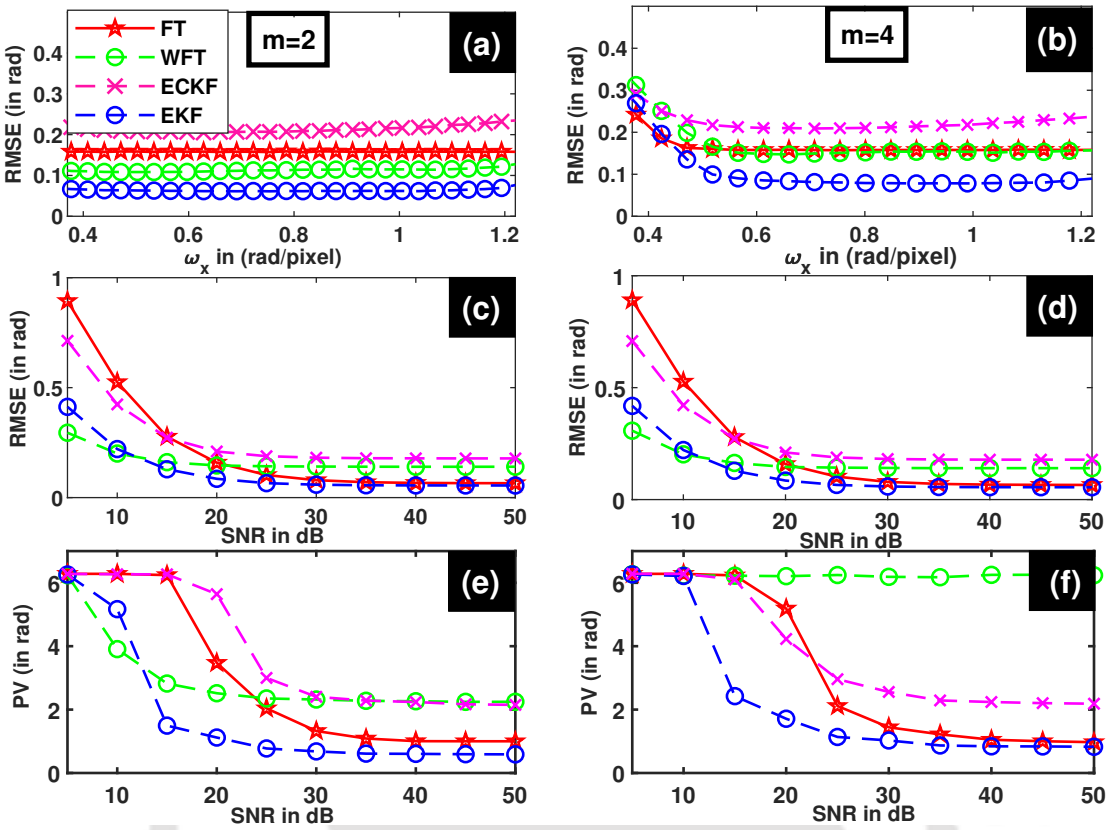

FIGURE 5.18: RMSEs in the phase estimation as function of carrier frequency with (a) m = 2 and (b) m = 4. RMSEs in the phase estimation as function of SNR (in dB) with (c) m = 2 and (d) m = 4; PVs in the phase estimation as function of SNR (in dB) with (e) m = 2 and (f) m = 4 [6].

Size (in pixels)	Computational time (in seconds)			
	FT	WFT	ECKF	EKF
400 × 400	0.011	2.28	3.51	1.314
576 × 768	0.0202	7.89	9.15	2.84
651 × 621	0.0186	9.06	8.76	3.09

TABLE 5.4: Computational time (in second) required by fringe pattern demodulation algorithms

Experiment

The performance of the proposed method was evaluated using the experimentally recorded fringe patterns. Figure 5.19(a) shows the fringe pattern of size 576 × 768 recorded in a holographic interferometry setup corresponding to the surface deformation of an aluminum plate subjected to point load, and Fig. 5.19(b) shows the fringe pattern of size

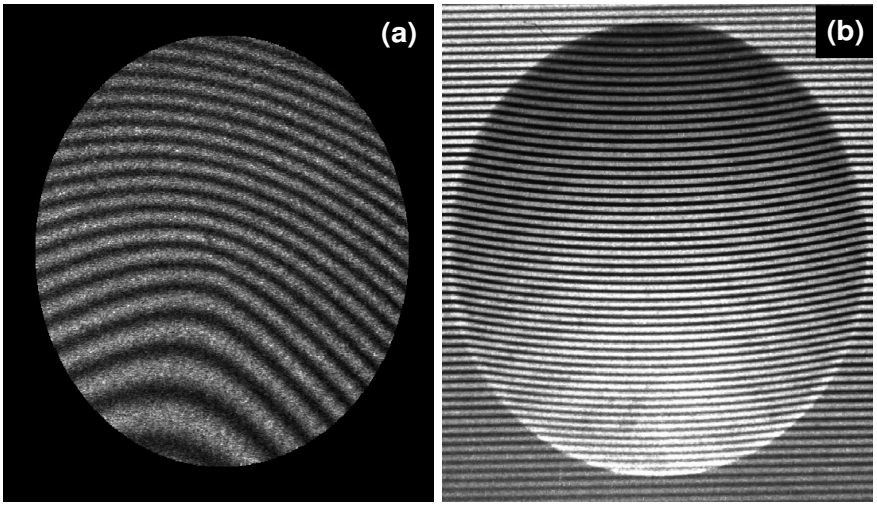

FIGURE 5.19: (a) Fringe pattern recorded in a holographic interferometry setup corresponding to the deformation of an aluminum plate and (b) fringe pattern recorded in a fringe projection profilometry setup corresponding to the dome-shaped object [6].

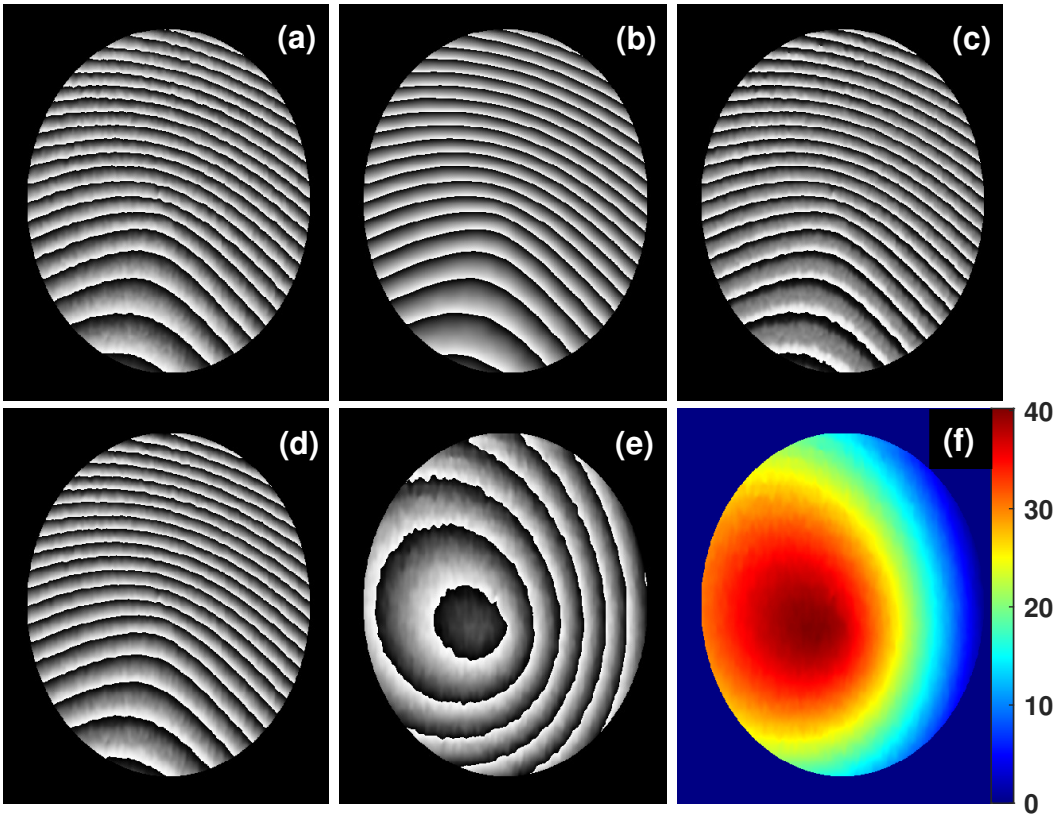

FIGURE 5.20: Estimated phase of the experimental fringe pattern shown in Fig. 5.19 (a) computed using the (a) FT, (b) WFT, (c) ECKF and (d) EKF methods; (e) phase estimate after carrier phase removal; (f) unwrapped phase. All phase values are in radians [6].

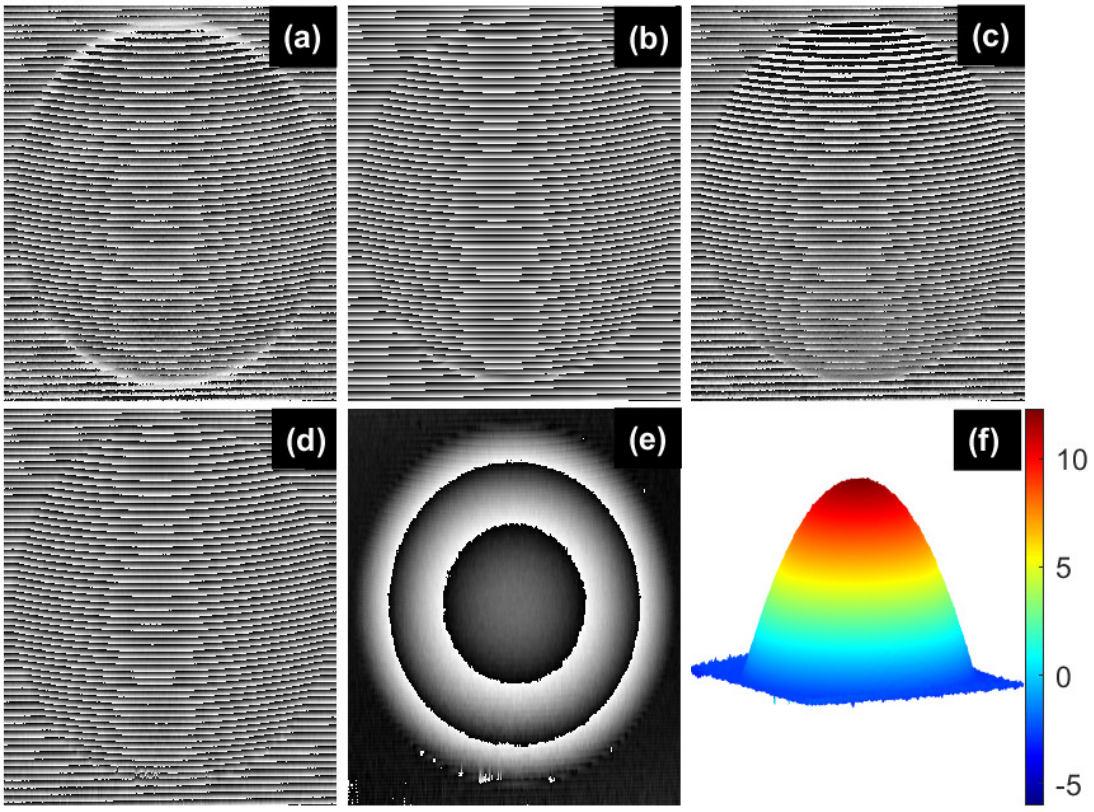

FIGURE 5.21: Estimated phase of the experimental recorded fringe pattern shown in Fig. 5.19 (b) computed using the (a) FT, (b) WFT, (c) ECKF and (d) EKF methods; (e) phase estimate after carrier phase and quadratic phase aberration removal; (f) unwrapped phase. All phase values are in radians [6].

651 × 621 recorded in a fringe projection profilometry setup corresponding to a dome-shaped object. The phase estimates ($\hat{\theta}$) obtained from the fringe pattern in Fig. 5.19(a) using the FT, WFT, ECKF and EKF methods are shown in Fig. 5.20(a), 5.20(b), 5.20(c), and 5.20(d), respectively. The carrier frequency estimated using the EKF based method was 0.2650 rad. Figure 5.20(e) shows the phase ($\hat{\phi}$) corresponding to the surface deformation obtained after removing the carrier phase contribution. It can be noted that the carrier phase contribution was reliably removed. Figure 5.20(f) shows the unwrapped phase obtained using the method reported in [136, 137]. Similarly, the phase estimates ($\hat{\theta}$) obtained from the fringe pattern in Fig. 5.19(b) using the FT, WFT, ECKF, and EKF methods are shown in Figs. 5.21(a), 5.21(b), 5.21(c), and 5.21(d), respectively. The carrier frequency estimated using the proposed method was 0.5890 rad. Figure 5.21(e) shows the phase ($\hat{\phi}$) corresponding to the object shape obtained after removing the carrier phase and quadratic phase aberration. Figure 5.21(f) shows the unwrapped

phase depicting the three-dimensional shape of the object. It can be noted from Figs. 5.21(a) and 5.21(c) that the performances of FT and ECKF deteriorates are the object boundaries. On the other hand, the WFT and EKF based methods provide reliable phase estimates.

5.3.3 Conclusion

In this chapter, an extended Kalman filter method is used to provide satisfactory results in phase demodulation. The proposed algorithm is noise robust and possesses inherent capability of carrier frequency estimation for the removal of carrier phase contribution. The proposed method doesn't require the pre-processing operation of background intensity removal before demodulation, which makes algorithm robust and reduces time complexity. In addition, the proposed method performs pixel-wise demodulation of fringe pattern as opposed to the FT and WFT methods, accurate phase estimates are obtained especially at the image or masked region boundaries.

Chapter 6

Closed Fringe Pattern Demodulation

The accurate phase retrieval is of prime importance as the information of the measured quantity is encoded in the phase of the optical wavefront. Although, single carrier modulated fringe pattern demodulation is advantageous especially in the measurement of dynamic events, the presence of carrier fringes limits the dynamic range of estimated phase. On the other hand, the PSI techniques provide high accuracy and high dynamic range in the phase estimation. However, high mechanical stability required during the fringe pattern recordings limit their application in practical scenarios. Therefore, it is desirable to obtain phase estimation from a single closed fringe pattern.

In this chapter, a closed fringe pattern demodulation technique based on the phase representation using a weighted linear combination of Zernike polynomials (ZPs) has been proposed. In this method, the two-dimensional phase is represented as a weighted linear combination of a certain number of Zernike polynomials (ZPs). Essentially, the problem of phase estimation is converted into the estimation of ZP coefficients. The l1-norm regularized EKF is employed for computing the ZP coefficients as an unwrapped phase estimate is obtained using these coefficients.

6.1 Fringe Demodulation with Zernike Polynomials Phase Fitting and $\ell 1$-norm Regularized Extended Kalman Filter

A closed fringe pattern can be represented as

$$\mathrm{I(x,y)} = \mathrm{a(x,y)} + \mathrm{b(x,y)}\cos[\phi(\mathrm{x,y})]. \tag{6.1}$$

The normalized fringe pattern can be represented as

$$\mathrm{I(x,y)} = \cos[\phi(\mathrm{x,y})]. \tag{6.2}$$

The normalized closed fringe pattern can be obtained using any one of the fringe normalization techniques [3, 68, 150, 151] . As mentioned previously, the phase is represented as a weighted linear combination of a given number of ZPs. Since ZPs are defined on a unit circle, the phase model is represented in a polar form as [152]

$$\hat{\phi}(\mathbf{r},\theta) = \sum_{\mathrm{q}=1}^{\mathrm{Q}} \mathbf{s}_{\mathrm{q}} \mathrm{Z}_{\mathrm{q}}(\mathbf{r},\theta), \tag{6.3}$$

where $\mathbf{r}$ and θ represent radial and angular coordinates, respectively; $\mathrm{Z_q}(\mathbf{r},\theta)$ is the qth Zernike polynomial evaluated at $(\mathbf{r},\theta)$; q is the mode ordering number. The Zernike functions are given as [153]

$$\mathrm{Z_q}(\mathbf{r},\theta) = \begin{cases} \mathrm{R_n^m}(\mathbf{r})\cos(\mathrm{m}\theta) & \mathrm{m} \neq 0 \text{ and even q} \\ \mathrm{R_n^m}(\mathbf{r})\sin(\mathrm{m}\theta) & \mathrm{m} \neq 0 \text{ and odd q} \\ \mathrm{R_n^m}(\mathbf{r}) & \mathrm{m} = 0 \end{cases} \tag{6.4}$$

The Zernike radial polynomial is defined as

$$\mathrm{R_n^m}(\mathbf{r}) = \begin{cases} \sum_{\mathrm{k}=0}^{\frac{\mathrm{n}-\mathrm{m}}{2}} \frac{(-1)^{\mathrm{k}}(\mathrm{n}-\mathrm{k})!}{\mathrm{k}!(\frac{\mathrm{n}+\mathrm{m}}{2}-\mathrm{k})!(\frac{\mathrm{n}-\mathrm{m}}{2}-\mathrm{k})!} \mathrm{r}^{\mathrm{n}-2\mathrm{k}} & \mathrm{n}-\mathrm{m} = \text{even} \\ 0 & \mathrm{n}-\mathrm{m} = \text{odd} \end{cases} \tag{6.5}$$

Here, the non-negative integers n and m are called the radial order and angular frequency of the polynomial functions, respectively. Based on the phase representation given in Eq. (6.3), the fringe pattern intensity can also be modelled for a given set of ZP coefficients as

$$\hat{\mathrm{I}}(\mathbf{r},\theta) = \cos[\hat{\phi}(\mathbf{r},\theta)] = \cos\left(\sum_{\mathrm{q}=1}^{\mathrm{Q}} \mathbf{s}_{\mathrm{q}} \mathrm{Z}_{\mathrm{q}}(\mathbf{r},\theta)\right). \tag{6.6}$$

For the accurate phase representation using ZPs, a set of $\mathbf{s}_{\mathrm{q}}$s needs to be computed such that the following cost function is minimized,

$$\mathrm{f}(\mathbf{s}) = \frac{1}{\mathrm{N}_{\mathrm{S_a}}} \sum_{\mathrm{S_a}} \left[\mathrm{I}(\mathbf{r},\theta) - \hat{\mathrm{I}}(\mathbf{r},\theta)\right]^2, \tag{6.7}$$

where $\mathrm{S_a}$ is the circular region over which fringe intensity is defined; $\mathrm{N_{s_a}}$ represents the total number of pixels in $\mathrm{S_a}$. It can be observed from Eq. (6.6) that the fringe intensity model is a nonlinear function of $\mathbf{s}_{\mathrm{q}}$s. Consequently, we propose to utilize the EKF for the estimation of coefficients. Accordingly, a state space model is defined as below:

$$\mathbf{s}_{\mathrm{x}} = \mathbf{F}\mathbf{s}_{\mathrm{x}-1} \tag{6.8}$$

$$\mathbf{z}_{\mathrm{x}} = \mathrm{h}_{\mathrm{x}}(\mathbf{s}_{\mathrm{x}}) + \mathbf{v}_{\mathrm{x}} \tag{6.9}$$

In the above model, the ZP coefficients are considered to be the elements of state vector $\mathbf{s}$ of size $\mathrm{Q} \times 1$; $\mathbf{F}$ is the state transition matrix; $\mathbf{z}_{\mathrm{x}}$ and $\mathbf{v}_{\mathrm{x}}$ represent normalized fringe intensity and measurement noise at xth pixel location, respectively. The function $\mathbf{h}_{\mathrm{x}}(\cdot)$ represents the nonlinear measurement model given in Eq. (6.6). The fringe pattern is raster-scanned and the variable x is incremented as $0, 1, 2, 3, \cdots$. The state estimation procedure based on the EKF is given Algorithm 7.

6.2 Results

Simulation

The performance of the proposed method is evaluated with a simulated study. Three simulated closed fringe patterns each of size 200×200 pixels were generated are shown

Algorithm 7 Closed fringe demodulation with Zernike Polynomials and Extended Kalman filter

1: The state vector estimate and covariance of the estimation error are initialized as

$\hat{\mathbf{s}}_{0|0} = \mathbb{E}(\mathbf{s}_0)$,

$\mathrm{P}_{0|0} = \mathbb{E}[(\mathbf{s}_0 - \hat{\mathbf{s}}_{0|0})(\mathbf{s}_0 - \hat{\mathbf{s}}_{0|0})^{\mathrm{T}}$,

where, $\mathbb{E}$ represents the expectation operator; $(\cdot)^{\mathrm{T}}$ represents transpose operator. The covariance matrix $\mathrm{P}_{0|0}$ defines the uncertainty in the state estimate. Once the initialization of the EKF is performed, following equations are implemented for $\mathrm{x} = 0, 1, 2, \cdots$

2: The process update equations are given as

$\hat{\mathbf{s}}_{\mathrm{x}|\mathrm{x}-1} = \mathbf{F}\hat{\mathbf{s}}_{\mathrm{x}-1|\mathrm{x}-1}$,

$\mathrm{P}_{\mathrm{x}|\mathrm{x}-1} = \mathbf{F}\mathrm{P}_{\mathrm{x}-1|\mathrm{x}-1}\mathbf{F}^{\mathrm{T}}$,

3: The nonlinear function $\mathbf{h}_{\mathrm{x}}(\mathbf{s}_{\mathrm{x}})$ is linearized around the state estimate $\hat{\mathbf{s}}_{\mathrm{x}|\mathrm{x}-1}$ using first order Taylor series expansion as

$\mathbf{h}_{\mathrm{x}}(\mathbf{s}_{\mathrm{x}}) = \mathbf{h}_{\mathrm{x}}(\hat{\mathbf{s}}_{\mathrm{x}|\mathrm{x}-1}) + \left.\frac{\partial \mathbf{h}_{\mathrm{x}}}{\partial \mathbf{s}}\right|_{\hat{\mathbf{s}}_{\mathrm{x}|\mathrm{x}-1}} (\mathbf{s}_{\mathrm{x}} - \hat{\mathbf{s}}_{\mathrm{x}|\mathrm{x}-1})$.,

The partial derivative matrix $\mathbf{H}_{\mathrm{x}} = \left.\frac{\partial \mathbf{h}_{\mathrm{x}}}{\partial \mathbf{s}}\right|_{\hat{\mathbf{s}}_{\mathrm{x}|\mathrm{x}-1}}$ is computed using Eq. (6.6).

4: The measurement update equations are given as

$\mathbf{K}_{\mathrm{x}} = \mathrm{P}_{\mathrm{x}|\mathrm{x}-1}\mathbf{H}_{\mathrm{x}}^{\mathrm{T}}(\mathbf{H}_{\mathrm{x}}\mathrm{P}_{\mathrm{x}|\mathrm{x}-1}\mathbf{H}_{\mathrm{x}}^{\mathrm{T}} + \mathbf{R}_{\mathrm{x}})^{-1}$,

$\hat{\mathbf{s}}_{\mathrm{x}|\mathrm{x}} = \hat{\mathbf{s}}_{\mathrm{x}|\mathrm{x}-1} + \mathbf{K}_{\mathrm{x}}[\mathbf{z}_{\mathrm{x}} - \mathbf{h}_{\mathrm{x}}(\hat{\mathrm{s}}_{\mathrm{x}|\mathrm{x}-1})]$,

$\mathrm{P}_{\mathrm{x}|\mathrm{x}} = (\mathbf{I} - \mathbf{K}_{\mathrm{x}}\mathbf{H}_{\mathrm{x}})\mathrm{P}_{\mathrm{x}|\mathrm{x}-1}(\mathbf{I} - \mathbf{K}_{\mathrm{x}}\mathbf{H}_{\mathrm{x}})^{\mathrm{T}} + \mathbf{K}_{\mathrm{x}}\mathrm{R}_{\mathrm{x}}\mathbf{K}_{\mathrm{x}}^{\mathrm{T}}$,

where, $\mathbf{R}_{\mathrm{x}}$ and $\mathbf{K}_{\mathrm{x}}$ represent the measurement noise covariance and Kalman gain, respectively. $\mathbf{I}$ represents identity matrix of size $\mathrm{Q} \times \mathrm{Q}$.

5: The measurement equation is highly non-linear. Therefore, the EKF based coefficient estimation may not converge towards true solution. To overcome this difficulty, we propose to utilize the $\ell 1$-norm regularization scheme [154] wherein we utilize the fact that generally for any given fringe pattern, only few phase representing ZP coefficients are non-zero. This prior knowledge of sparsity of the state vector can be incorporated along with the EKF algorithm to improve its convergence performance. Basically, a pseudo measurement process $0 = \|\hat{\mathbf{s}}_{\mathrm{x}|\mathrm{x}}\|_1 - \eta$ is considered to impose the sparsity constraint. As described in [154, 155], a posteriori state estimate $\hat{\mathbf{s}}_{\mathrm{x}|\mathrm{x}}$ is further updated in $\mathrm{N_i}$ number of iterations as follows

$\hat{\mathbf{s}^0} = \hat{\mathbf{s}}_{\mathrm{x}|\mathrm{x}}, \quad \mathrm{P}^0 = \mathrm{P}_{\mathrm{x}|\mathrm{x}}$,

Following equations are implemented for $\mathrm{i} = 1, \cdots, \mathrm{N_i}$:

$\hat{\mathbf{H}}_{\mathrm{i}-1} = \left[\mathrm{sign}\left(\hat{\mathbf{s}}^{\mathrm{i}-1}(1)\right), \mathrm{sign}\left(\hat{\mathbf{s}}^{\mathrm{i}-1}(2)\right), \cdots, \mathrm{sign}\left(\hat{\mathbf{s}}^{\mathrm{i}-1}(\mathrm{P})\right)\right]$,

$\mathbf{K}^{\mathrm{i}-1} = \mathrm{P}^{\mathrm{i}-1}\hat{\mathbf{H}}_{\mathrm{i}-1}^{\mathrm{T}}\left(\hat{\mathbf{H}}_{\mathrm{i}-1}\mathrm{P}^{\mathrm{i}-1}\hat{\mathbf{H}}_{\mathrm{i}-1}^{\mathrm{T}} + \mathbf{R}_{\eta}\right)^{-1}$,

$\hat{\mathbf{s}}^{\mathrm{i}} = \left(\mathbf{I} - \mathbf{K}^{\mathrm{i}-1}\hat{\mathbf{H}}_{\mathrm{i}-1}\right)\hat{\mathbf{s}}^{\mathrm{i}-1}$,

$\mathrm{P}^{\mathrm{i}} = \left(\mathbf{I} - \mathbf{K}^{\mathrm{i}-1}\hat{\mathbf{H}}_{\mathrm{i}-1}\right)\mathrm{P}^{\mathrm{i}-1}$,

where, sign(·) represents the signum function such that

$$\text{sign}\left(\hat{\mathbf{s}}^{i-1}(k)\right) = \begin{cases} 1, & \text{if } \mathbf{s}^{i-1}(k) \geq 0 \\ -1, & \text{otherwise.} \end{cases},$$

$\mathbf{R}_\eta$ represents the pseudo measurement noise covariance. The value of N_i is manually selected depending on the required estimated accuracy.

6: At the end of above iteration, we set

$\hat{\mathbf{s}}_{x|x} = \hat{\mathbf{s}}^{N_i}$,

$P_{x|x} = P^{N_i}$

7: Once all the pixels in the region S_a are scanned, the final state vector $\hat{\mathbf{s}}_{x|x}$ is substituted into Eq. (6.3) to obtain the estimate of phase. The selection of initial state estimate $\hat{\mathbf{s}}_{0|0}$ and estimate error covarianve matrix $P_{0|0}$ plays crucial role in converging towards the true state vector. Since there is no way of obtaining the initial state estimate, the elements of the state vector are randomly chosen in the range of $[-\pi, \pi]$ with a high value of $P_{0|0}$ indicating a low confidence on the initial state estimate.

8: As stated above, the selection of random initial state vector may not always converge toward true state estimate. In order to insure such convergence, the state estimation is performed number of times with a distinct random initial state estimate selected each time. The norm of covariance matrix $P_{x|x}$ is used as a metric to evaluate the convergence of state estimate towards the true value. That is, norm of covariance matrix is compared with a user defined threshold, $t_{\|P\|}$, at each iteration. The state estimate for which the covariance matrix norm goes below the threshold, that value is selected for obtaining the phase estimate.

9: It is important to note that an appropriate selection of number of Zernike functions, Q, is also essential for minimum error phase-estimate. However, in general, we do not have any a-priori knowledge on this selection. In the proposed approach, we compute the phase estimate for a range of values of Q. In each case, the error function given in Eq. (6.7) is computed. The value of Q for which root mean square error (RMSE) is minimum, the corresponding phase is selected as the final phase estimate.

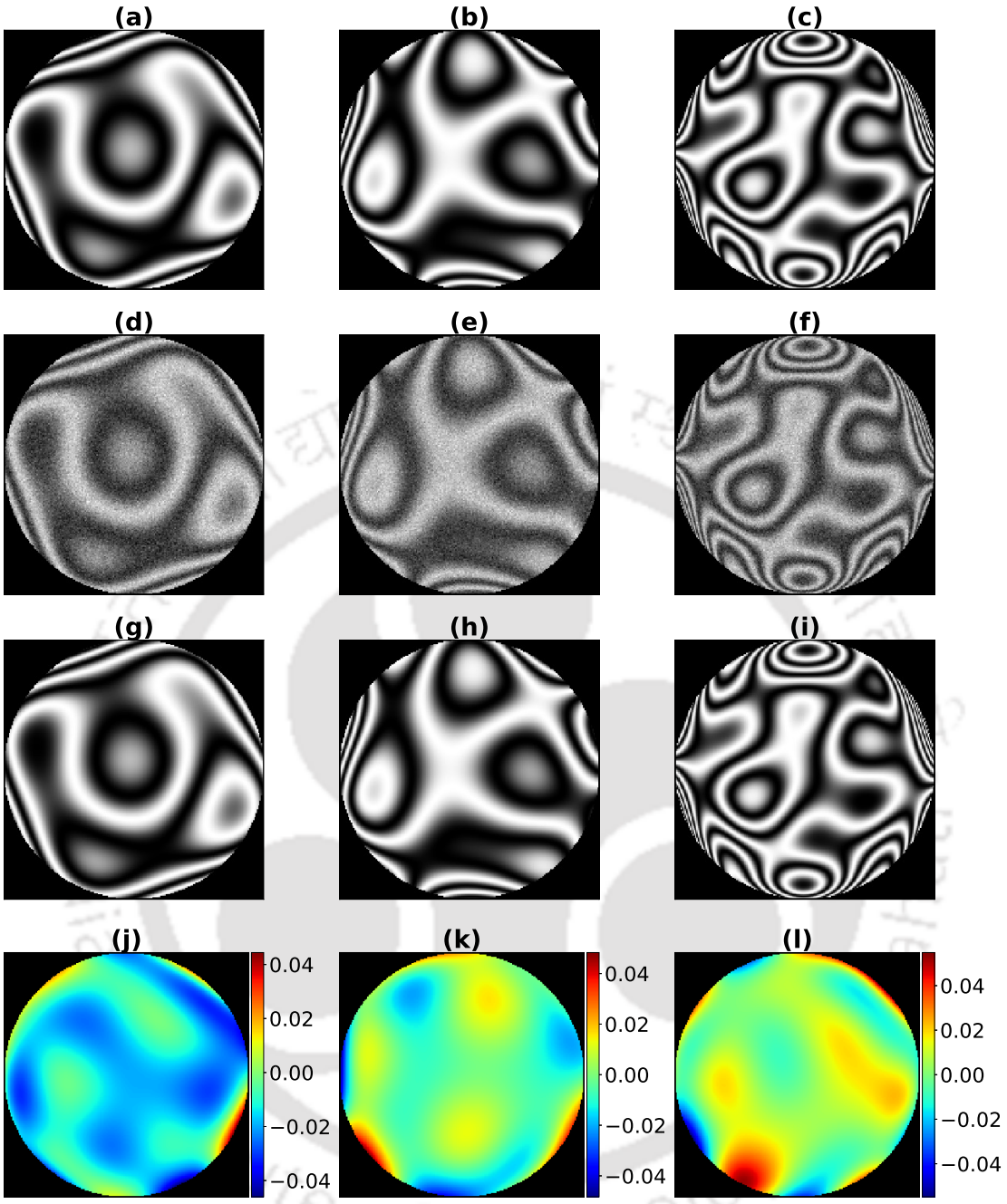

FIGURE 6.1: (**Simulation results**) First row: simulated closed fringe pattern; second row: closed fringe pattern simulated at signal to noise ratio of 10 dB; third row: fringe patterns generated with the estimated phases.; fourth row: pixel-wise maps of errors in the phase estimation. All phase values are in radian [7].

in the first row of Fig. 6.1 using the combinations of ZPs as phase profiles. The ZP coefficients used in the fringe patterns simulation are shown in the first row of Fig. 6.2. The second row of Fig. 6.1 shows the noisy fringe patterns simulated at signal to noise ratio of 10 dB. The algorithm parameters selected for obtaining the simulation and

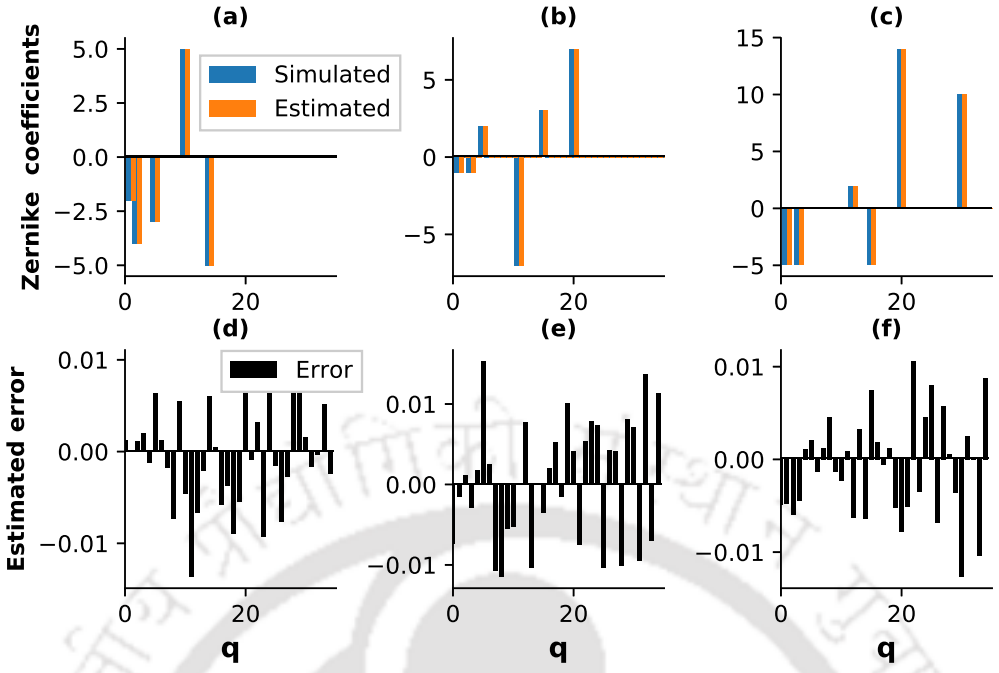

FIGURE 6.2: (**Simulation results**) (a), (b) and (c) plots of true ZP coefficients used in the simulation of fringe patterns shown in first row of Fig. 6.1 and estimated ZP coefficients from the demodulation of fringe patterns shown in third row of Fig. 6.1; (d), (e), and (f) plots of errors in the estimation of ZP coefficients [7].

experimental results are given in Table 6.1. The parameter values have been selected in an empirical manner. It has been observed that small variations in the parameter

Parameters	$\hat{\mathbf{s}}_{0\|0}$	$\mathrm{P}_{0\|0}$	$\mathrm{R_x}$	R_η	$\mathrm{t_P}$	Q
Values	rand$[-\pi, \pi]$	$10^4\mathbf{I}$	10^2	10^8	5	$[1, 35]$

TABLE 6.1: Algorithm parameters used to obtain the simulation and experimental results.

values do not affect the phase estimation performance. The third row in Fig. 6.1 shows the fringe patterns generated using the estimated phase maps. From the comparison between the first row and third row, it can be noted that the proposed method provides good fringe demodulation performance in the presence of noise. Further, the pixel-wise phase estimation error maps are provided in the fourth row of Fig. 6.1.

Figures 6.2(a), 6.2(b), and 6.2(c) show the simulated and estimated ZP coefficients corresponding to the fringe patterns shown in Figs. 6.1(d), 6.1(e), and 6.1(f), respectively. The difference between the simulated and estimated coefficients are also plotted in the

second row of Fig. 6.2. From these results it can be deducted that the proposed algorithm provided accurate estimation of ZP coefficients in each case. In order to emphasize the robustness offered by the proposed method, the fringe demodulation results were obtained at different SNR values. For each SNR, five simulations runs were performed for the demodulation of fringe patterns shown in the first row of Fig. 6.1. The RMSEs and the peak-to-valley (PV) errors in the phase estimations were computed for each run. The RMSE [156] and PV [93] in the phase estimations were computed as

$$\text{RMSE} = \frac{1}{\text{N}_{\text{sa}}}\sqrt{\sum_{\text{i}=1}^{\text{N}_{\text{sa}}}(\phi_{\text{i}} - \hat{\phi}_{\text{i}})^2} \tag{6.10}$$

$$\text{PV} = \max(\phi - \hat{\phi}) - \min(\phi - \hat{\phi}) \tag{6.11}$$

The mean and standard deviation of these errors are plotted in function of SNR in Fig. 6.3(a) and 6.3(b), respectively. These values clearly indicate the high success rate and robustness of the proposed method in closed fringe demodulation.

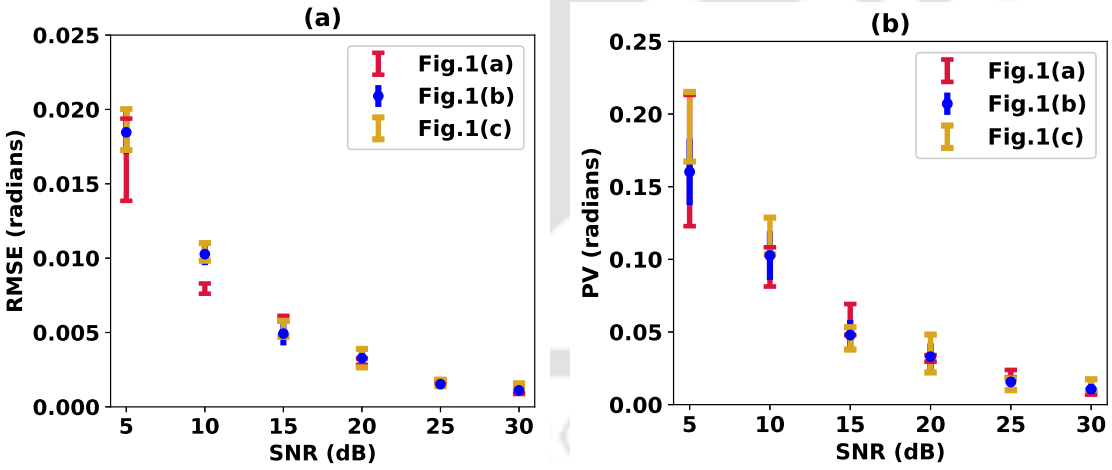

FIGURE 6.3: **Simulation results** (a) RMSEs and (b) PV errors computed in function of SNR (dB) for the phase estimation from fringe patterns shown in Fig. 6.1 [7].

The number of Zernike polynomials used to represent the phase are selected in the range of $\text{Q} \in [1, 35]$. Generally in parameter estimation techniques, the number of measurements N_{sa} should be sufficiently higher than the number of parameters Q. For the simulated fringe patterns of size 200×200, we have $\text{N}_{\text{sa}} = 31064$ which is sufficiently

higher than the optimal values of Q = 31, Q = 32, and Q = 32 required to achieve the results shown in third row of Fig. 6.1.

Experiment

The experimental validation of the proposed method was performed using the experimentally recorded fringe patterns of sizes 511×511, 363×363, and 273×273 pixels, shown in Fig. 6.4(a), 6.4(b), and 6.4(c), respectively. In these fringe patterns, the fringe data are available over circular region such that $N_{Sa} = 201853$, $N_{Sa} = 100639$, and $N_{Sa} = 56982$ pixels, respectively. The adaptive monogenic filter (AMF) algorithm [151] was used for the fringe pattern normalization. The normalized fringe patterns are shown in the second row of Fig. 6.4. Along with the normalized fringe pattern, the AMF algorithm also provides an information on the fringe amplitude. The experimental fringe patterns are usually corrupted by speckle noise. The state estimation process is avoided at pixel locations which are corrupted by speckle noise. Such pixels are identified as those where the fringe amplitude is below 0.1. The estimated phases are shown in the third row of Fig. 6.4. These phases were obtained with Q = 5, Q = 26, and Q = 3. To verify the fidelity of the estimated phases, the fringe patterns generated using these phase maps are shown in the fourth row of Fig. 6.4. It can be deduced from the comparison of first and fourth rows of Fig. 6.4 that the proposed method has accurately estimated all the phase maps.

6.3 Discussion

The proposed algorithm converts the problem of closed fringe pattern demodulation for the phase estimation into the estimation of Zernike polynomial coefficients using the EKF. The incorporation of $\ell 1$-norm regularization of the EKF offers robustness in the present case of highly nonlinear parameter estimation problem. The EKF also takes into account the noise in the measurement of fringe intensity providing noise-robust phase estimation. Since the phase representation is made in terms of continuous Zernike

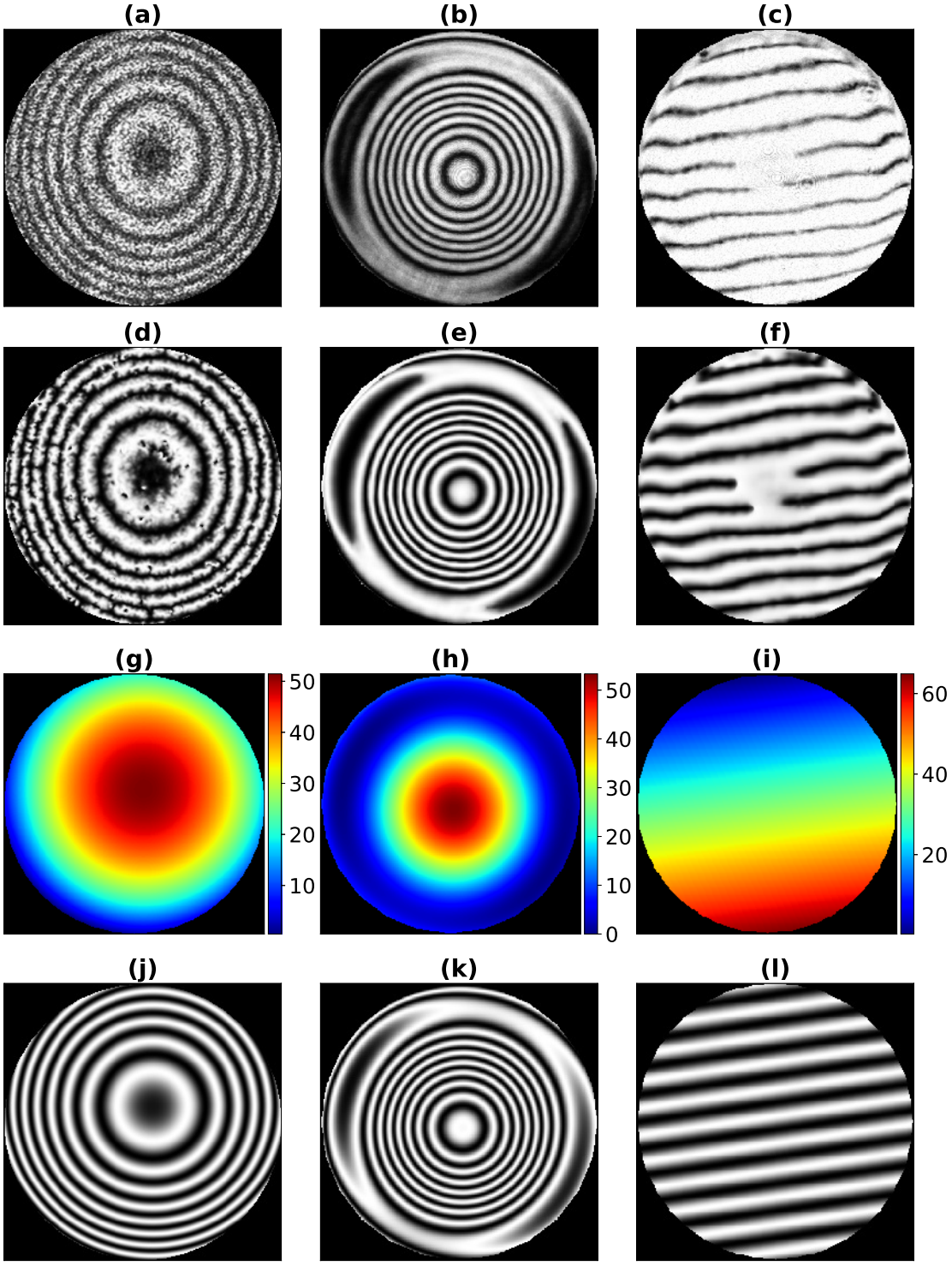

FIGURE 6.4: (**Experimental results**) First row: closed fringe pattern; second row: normalized fringe pattern; third row: estimated phases in radians; fourth row: fringe patterns corresponding to the estimated phases. All phase values are in radian [7].

polynomial functions, the phase profiles which involve inherent discontinuities may not be reconstructed perfectly using the proposed method. However, this limitation exists for all fringe demodulation methods which works on the assumption of phase continuity.

6.4 Conclusion

The phase representation with a weighed linear combination of ZPs offers a solution to estimate an unwrapped phase from a closed fringe pattern. The ZP coefficients are reliably estimated using the EKF endowed with a pseudo measurement equation. The proposed method is found to be noise robust and capable of demodulating fringe patterns with a wide range of fringe densities.

Chapter 7

Phase Aberration Compensation

Phase aberration compensation is an important operation in quantitative phase imaging techniques as outlined in the Section 2.4.1. The phase imaging technique can either be non-interferometric, such as transport-of-intensity equation-based method or interferometric, such as digital holographic microscopy (DHM). The DHM has been employed in a variety of applications, for example, biophotonics, microfluidics and metrology, etc. A typical DHM system consists of a microscope objective (MO) to achieve the required object magnification in the numerically reconstructed object image from the recorded hologram. However, the use of an MO and imperfections of optical components introduces additional phase, that is, phase aberrations, in addition to the phase associated with the specimen under investigation. In quantitative phase imaging of bio-specimen, the phase is associated with cells/tissues parameters such as cell size, dry-mass density, morphological parameters such as surface area, volume, sphericity, etc., and statistical parameters such as mean, standard deviation, entropy, skewness, etc. [157]. Different classes of the same cell/tissue type (e.g. normal and cancer cells) exhibit minuscule variations in the morphological and statistical parameters. Therefore, it is necessary to compensate for phase aberrations in the measurement for the faithful reconstruction and accurate quantification of aforementioned parameters to distinguish different cell's types

like normal and treated/diseased cells using DHM. This chapter introduced a phase aberration compensation techniques in a quantitative phase imaging system based on the Kalman filter (KF). This is fully automatic method and doesn't require any prior knowledge of the setup. To achieve better results, the fixed-lag smoothing KF named Rauch–Tung–Striebel (RTS) algorithm is utilized. The phase pattern is scanned in a zigzag manner for phase aberration estimation.

7.1 Phase Aberration Compensation using Kalman Filter

The DHM consists of optical recording and numerical reconstruction of hologram. The intensity of object scattered/transmitted wavefront and a reference wavefront interference is recorded as a hologram by a digital image sensor. The hologram intensity can be represented as

$$\begin{aligned} \mathrm{H_I(x,y)} &= |\mathrm{O(x,y)} + \mathrm{R(x,y)}|^2 \\ &= |\mathrm{O(x,y)}|^2 + |\mathrm{R(x,y)}|^2 + \mathrm{O(x,y)R^*(x,y)} + \mathrm{O^*(x,y)R(x,y)}. \end{aligned} \tag{7.1}$$

where, $\mathrm{O(x,y)}$ and $\mathrm{R(x,y)}$ represent object and reference wavefronts, respectively; $(\cdot)^*$ represents complex conjugate operation. The object wavefront in the hologram plane can be obtained by spectral filtering of the hologram intensity. Subsequently, the angular spectrum method [158] can be utilized to compute the object wavefront in the object plane by wavefront propagation. The phase measurement consists of two components as follows

$$\phi(\mathrm{x,y}) = \phi_\mathrm{o}(\mathrm{x,y}) + \phi_\mathrm{a}(\mathrm{x,y}) \tag{7.2}$$

where, ϕ_o and ϕ_a represents the object phase and system induced phase aberrations, respectively. This chapter proposes a technique to estimate the phase aberration (ϕ_a) using KF method from the measured phase and remove it in order to extract the object phase (ϕ_o). Pixel-wise zigzag scanning of the phase image is performed to estimate ϕ_a.

In order to utilize the KF, a state-space model is defined with ϕ_{a} as a state variable,

$$\mathbf{s}_{\mathrm{x}} = \mathbf{F}_{\mathrm{x}}\mathbf{s}_{\mathrm{x}-1} + \mathbf{w}_{\mathrm{x}},\ \ \mathbf{w}_{\mathrm{x}} = \mathcal{N}(0, \mathbf{Q}_{\mathrm{x}}), \tag{7.3}$$

$$\mathbf{z}_{\mathrm{x}} = \mathbf{H}_{\mathrm{x}}\mathbf{s}_{\mathrm{x}} + \mathbf{v}_{\mathrm{x}},\ \ \mathbf{v}_{\mathrm{x}} = \mathcal{N}(0, \mathbf{R}_{\mathrm{x}}). \tag{7.4}$$

The system equation (Eq.(7.3)) and the measurement equation (Eq.7.4) updates of the state are governed by the state-transition matrix $\mathbf{F}_{\mathrm{x}}$ and observation-matrix $\mathbf{H}_{\mathrm{x}}$, respectively. In this method, the state $\mathbf{s}_{\mathrm{x}}$ and $\mathbf{z}_{\mathrm{x}}$ represent the estimate of ϕ_{a} and ϕ, respectively, at a given pixel x.

The KF is used as a smoothing filter to extract the slowly varying aberration term from the measured phase. Accordingly, a first-order difference model is considered for state transition dynamics with $\mathbf{F}_{\mathrm{x}} = 1$. Further, ϕ is considered to be the measurement of phase aberration component by setting $\mathbf{H}_{\mathrm{x}} = 1$. This assumption is only valid in regions where ϕ_{o} contribution is minimum. Therefore, a binary mask is generated to avoid the object associated regions in ϕ during the estimation of ϕ_{a}. The system equation (Eq.(7.3)) represents a random walk model driven by the random noise process with zero mean and covariance $\mathbf{Q}_{\mathrm{x}}$. The measurement $\mathbf{z}_{\mathrm{x}}$, which basically represents the measured phase ϕ, is considered to be corrupted by a noise process with zero mean and covariance $\mathbf{R}_{\mathrm{x}}$. The KF algorithm consisting of forward and backward filtering procedures are described in Algorithm 8.

The state $\hat{\mathbf{s}}_{\mathrm{x}}^{(\mathrm{r})}$ estimated using Algorithm 8 represents an estimate phase aberration $\widehat{\phi}_{\mathrm{a}}(\mathrm{x})$. This estimate is subtracted from the measured phase(ϕ) to obtain the object phase estimate as

$$\widehat{\phi}_{\mathrm{o}} = \phi - \widehat{\phi}_{\mathrm{a}} \tag{7.5}$$

The value of $\mathbf{Q}_{\mathrm{x}}$ and $\mathbf{R}_{\mathrm{x}}$ are usually set empirically. In the proposed algorithm, the value of $\mathbf{Q}_{\mathrm{x}}$ is user defined and $\mathbf{R}_{\mathrm{x}}$ is set as $1 - \mathbf{Q}_{\mathrm{x}}$. An object masking scheme is utilized in order to retain the object phase while removing the contribution of aberration component from the measured phase. A binary mask is generated based on the numerically evaluated phase gradient.

Algorithm 8 Phase aberration compensation using Kalman filtering

Prediction and Update

1: The state and its associated error covariance matrix $\mathrm{P_x}$ are initialized at $\mathrm{x} = 0$ as

$\hat{\mathbf{s}}_0^+ = \mathbb{E}(\mathbf{s}_0)$,

$\mathrm{P}_0^+ = \mathbb{E}[(\mathbf{s}_0 - \hat{\mathbf{s}}_0^+)(\mathbf{s}_0 - \hat{\mathbf{s}}_0^+)^{\mathrm{T}}]$,

where, $\mathbb{E}$ represents the expectation operator. For fast convergence, the initial value of P_0^+ is set to be 10.

2: The forward Kalman filter is implemented for $\mathrm{x} = 1, \cdots, \mathrm{K}-1$ as follows

$\hat{\mathbf{s}}_\mathrm{x}^- = \mathbf{F}_\mathrm{x}\hat{\mathbf{s}}_{\mathrm{x}-1}^+$,

$\mathrm{P}_\mathrm{x}^- = \mathbf{F}_\mathrm{x}\mathrm{P}_{\mathrm{x}-1}^+\mathbf{F}_\mathrm{x}^{\mathrm{T}} + \mathbf{G}_\mathrm{x}\mathbf{Q}_\mathrm{x}\mathbf{G}_\mathrm{x}^{\mathrm{T}}$,

$\mathrm{K}_\mathrm{x} = \mathrm{P}_\mathrm{x}^-\mathbf{H}_\mathrm{x}^{\mathrm{T}}\left(\mathbf{H}_\mathrm{x}\mathrm{P}_\mathrm{x}^-\mathbf{H}_\mathrm{x}^{\mathrm{T}} + \mathbf{R}_\mathrm{x}\right)^{-1}$,

$\hat{\mathbf{s}}_\mathrm{x}^+ = \hat{\mathbf{s}}_\mathrm{x}^- + \mathrm{K}_\mathrm{x}\left(\mathbf{z}_\mathrm{x} - \mathbf{H}_\mathrm{x}\hat{\mathbf{s}}_\mathrm{x}^-\right)$,

$\mathrm{P}_\mathrm{x}^+ = \left(1 - \mathrm{K}_\mathrm{x}\mathbf{H}_\mathrm{x}\right)\mathrm{P}_\mathrm{x}^-\left(1 - \mathrm{K}_\mathrm{x}\mathbf{H}_\mathrm{x}\right)^{\mathrm{T}} + \mathrm{K}_\mathrm{x}\mathbf{R}_\mathrm{x}\mathrm{K}_\mathrm{x}^{\mathrm{T}}$,

where, superscripts $-$ and $+$ are used to represent the *a prior* and *a posterior* estimates; $\mathbf{G}_\mathrm{x} = 1$; K_x is the Kalman gain.

RTS smoother algorithm

3: In the backward filtering process, the RTS smoother algorithm is initialized at $\mathrm{x} = \mathrm{K}-1$ as

$\hat{\mathbf{s}}_{\mathrm{K}-1}^{(\mathrm{r})} = \hat{\mathbf{s}}_{\mathrm{K}-1}^+$ and $\mathrm{P}_{\mathrm{K}-1}^{(\mathrm{r})} = \mathrm{P}_{\mathrm{K}-1}^+$,

4: Following steps are implemented for $\mathrm{x} = \mathrm{K}-2, \cdots, 0$

$\mathrm{B}_{\mathrm{x}+1}^- = \left(\mathrm{P}_{\mathrm{x}+1}^-\right)^{-1}$,

$\mathrm{K}_\mathrm{x}^{(\mathrm{r})} = \mathrm{P}_\mathrm{x}^+\mathbf{F}_{\mathrm{x}+1}^{\mathrm{T}}\mathrm{B}_{\mathrm{x}+1}^-$,

$\mathrm{P}_\mathrm{x}^{(\mathrm{r})} = \mathrm{P}_\mathrm{x}^+ - \mathrm{K}_\mathrm{x}^{(\mathrm{r})}\left(\mathrm{P}_{\mathrm{x}+1}^- - \mathrm{P}_{\mathrm{x}+1}^{(\mathrm{r})}\right)(\mathrm{K}_\mathrm{x}^{(\mathrm{r})})^{\mathrm{T}}$,

$\hat{\mathbf{s}}_\mathrm{x}^{(\mathrm{r})} = \hat{\mathbf{s}}_\mathrm{x}^+ + \mathrm{K}_\mathrm{x}^{(\mathrm{r})}\left(\hat{\mathbf{s}}_{\mathrm{x}+1}^{(\mathrm{r})} - \hat{\mathbf{s}}_{\mathrm{x}+1}^-\right)$.

5: The described procedure is performed in a zigzag manner starting from top left corner and the same procedure is performed from its top right corner. Subsequently, maximum of these two estimates is considered as the aberration component estimate $\widehat{\phi}_\mathrm{a}$.

7.2 Results

7.2.1 Simulation

A simulation study was performed to evaluate the performance of the proposed method in comparison with the conventional Zernike polynomial (ZP) fitting-based approach of phase aberration compensation.

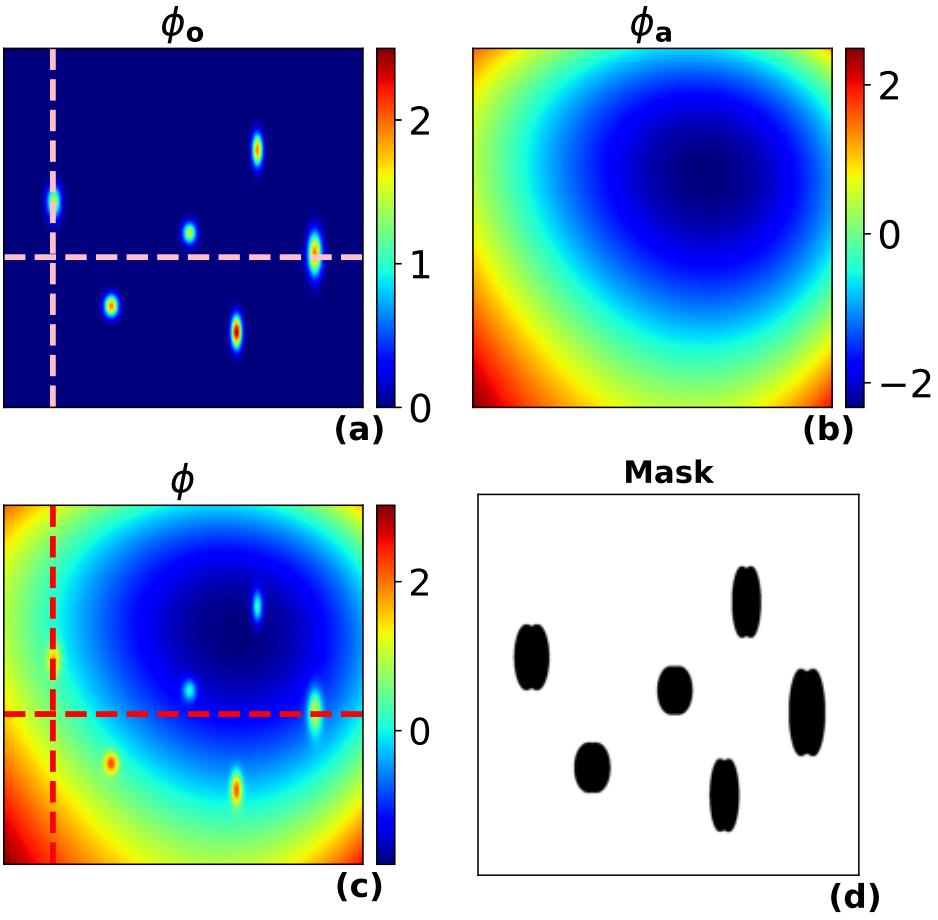

FIGURE 7.1: (**Simulation results**): (a) simulated object phase, (b) simulated phase aberration, (c) distorted phase with aberration and (d) generated binary mask. The phase values are in radians.

Figure 7.1(a) shows the simulated object phase of size 1000×1000. The phase aberration component shown in Fig. 7.1(b) was simulated using first eleven ZPs. These two phases are added together to obtain the aberrated phase shown in Fig. 7.1(c). The binary mask shown in Fig. 7.1(d) was obtained based on the phase gradient. It can be noted that the object phase region is masked which is avoided in the computation of phase aberration.

The performance of the proposed algorithm is compared with the commonly used ZP fitting method for phase aberration compensation. The ZP method compensated phase maps computed without and with mask are illustrated in Figs. 7.2(a) and 7.2(b), respectively. The aberration corrected phase maps obtaining using the proposed KF method

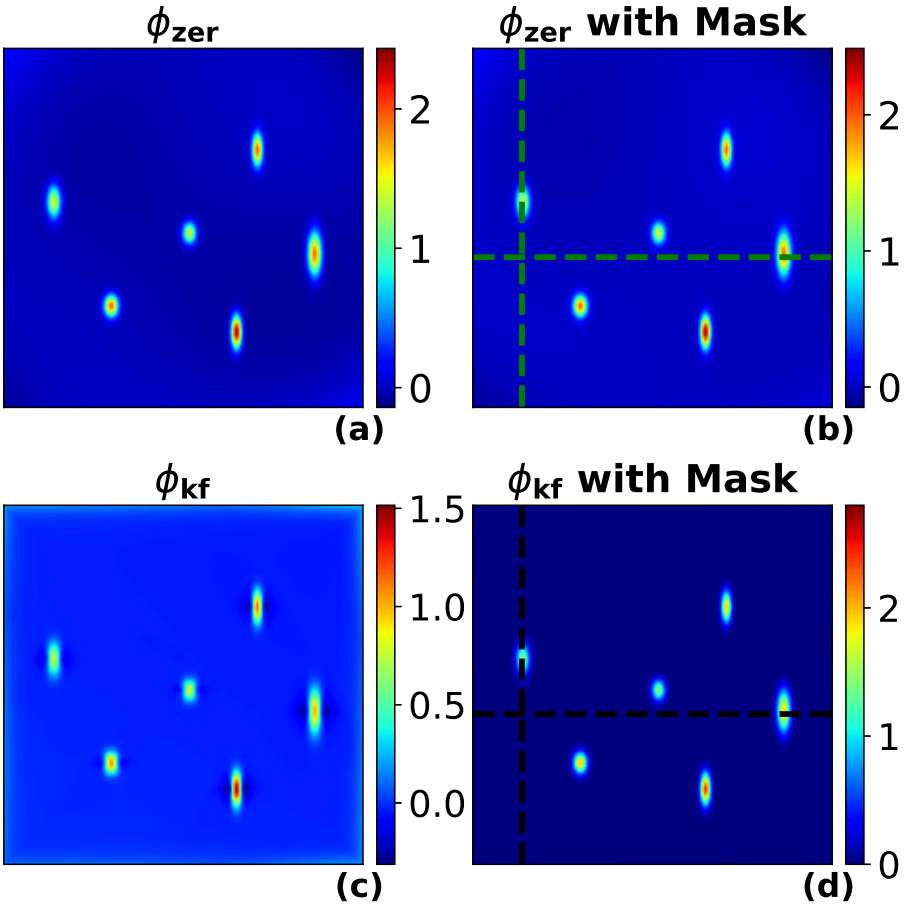

FIGURE 7.2: (**Simulation results**): Aberration compensation results obtained with ZP method (a) without and (b) with mask; KF method (c) without and (d) with mask. The phase values are in radians.

without and with mask are shown in Figs. 7.2(c) and 7.2(d), respectively. For the purpose of comparison, the one-dimensional plot of the object phase, phase with aberration , proposed KF method and Zernike polynomial compensated phase maps along the dotted lines are shown in Fig. 7.3(a) and 7.3(b). Although both methods are found to provide phase aberration compensation, the proposed KF based method provided comparatively better performance than the ZP fitting method especially at image boundaries and near center. The background of the compensated phase using the proposed KF method appear more uniform in the central region and at the edges compared to the ZP compensated phase.

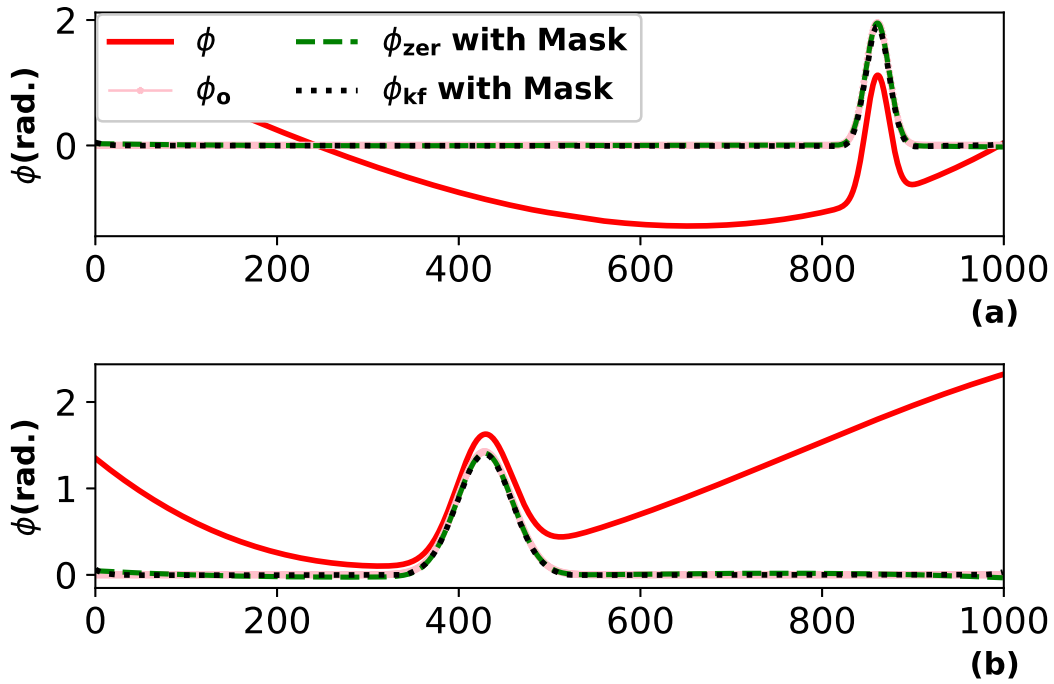

FIGURE 7.3: (**Simulation results**): The one-dimensional plot of the object phase, phase with aberration, proposed KF method and Zernike polynomial compensated phase maps along the dotted lines shown in Fig. 7.1(a), 7.1(c), 7.2(b), and 7.2(d).

The process covariance value was set to 1×10^{-3} for the phase aberration compensation results shown in Fig. 7.2(c,d).

7.2.2 Experiment

The experimental phase data of size 2048×2048 is utilized to demonstrate the capability of the proposed method and compared with Zernike method. The experiment was performed with $10\times/0.25$NA objective lens. Aberration removal of this type of sample would be difficult due to the large sample size, which covered most of the field of view (FOV) as shown in Fig. 7.4(a). The binary mask shown in Fig. 7.4(b) was obtained based on the phase gradient method. The ZP and proposed KF method compensated phases are illustrated in Figs. 7.4(c, d), respectively. It can be seen from Fig. 7.4(c) that the ZP method could not fully compensate the phase aberration especially near the boundary. On the other hand, the proposed KF method performed well and compensated the aberration term with good accuracy. The process covariance value was set to 6×10^{-6} for the phase aberration compensation results shown in Fig. 7.4(d). The line

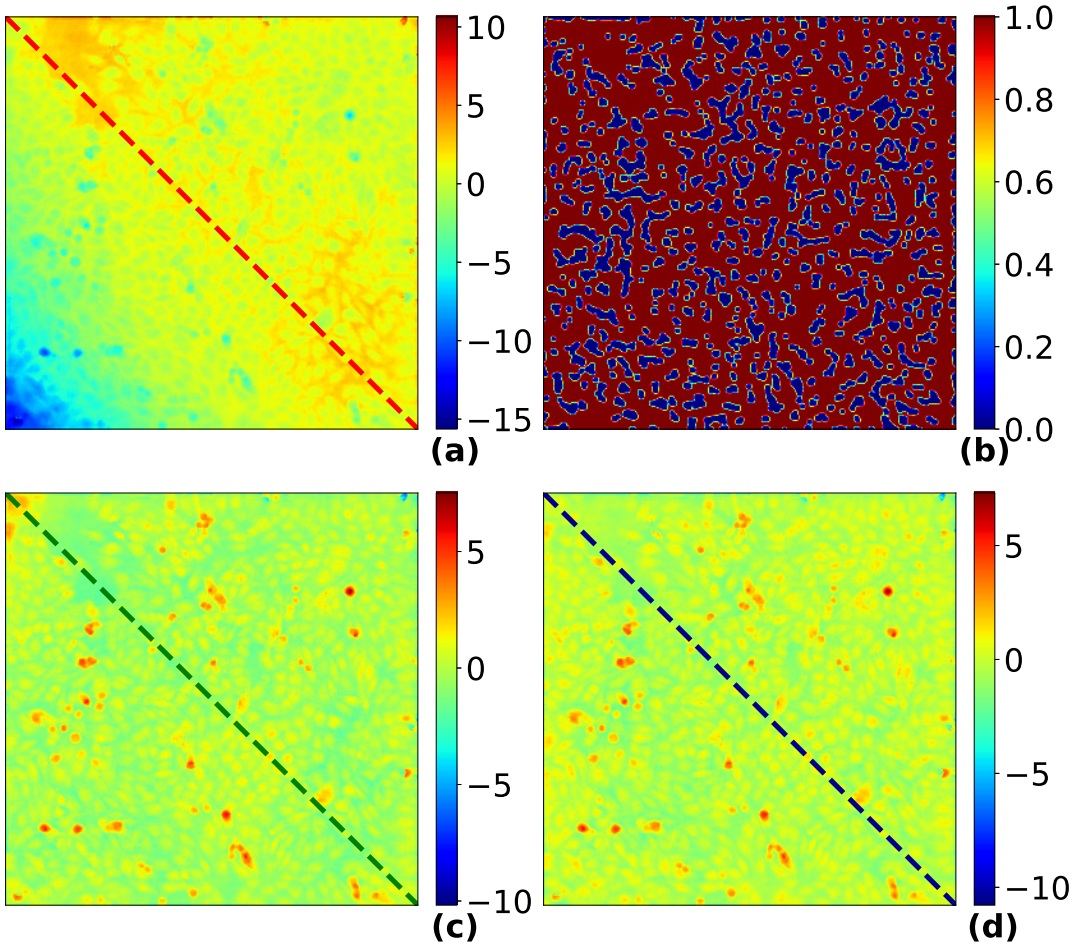

FIGURE 7.4: (**Experimental results**): (a) measured phase with aberrations, (b) generated binary mask, (c, d) ZP and proposed KF method compensated phases, All phase values are in radians.

profiles of the measured phase, ZP and proposed KF method compensated phases along the diagonal are plotted in Fig. 7.5.

Quantitative performance comparison among the ZP and KF methods has been performed using standard deviation (STD), peak-to-valley (PV) errors as given in Table 7.1. In the example given in Fig. 7.4, the STD and PV values were obtained from the object free region. It can be deduced from Table 7.1 that the KF method is more effective than ZP method in phase aberration compensation.

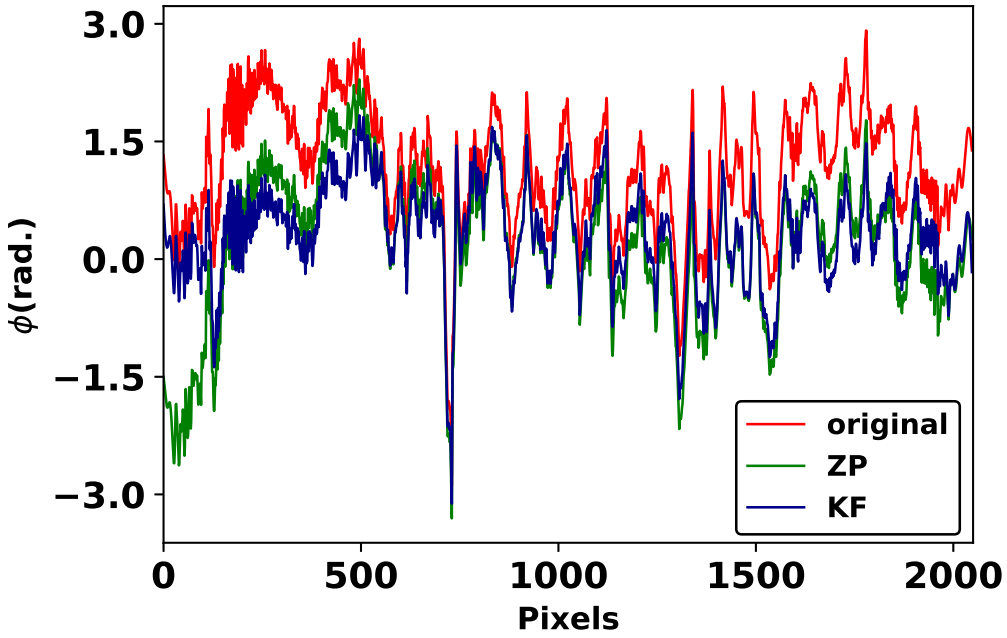

FIGURE 7.5: **(Experimental results)**: (a) line profiles of the measured phase, ZP and proposed KF method compensated phases along the dotted lines shown in Fig. 7.4(a), 7.4(c), and 7.4(d).

	Fig. 7.2(b)	Fig. 7.2(d)	Fig. 7.4(a)	Fig. 7.4(c)	Fig. 7.4(d)
STD	0.095	0.068	2.17	0.78	0.70
PV	0.556	0.417	22.39	13.70	13.06

TABLE 7.1: Quantitative performance comparison of the ZP and KF methods. All values are in radians.

7.3 Conclusion

In this chapter, a KF based method for phase aberration compensation is reported. Compared with the ZP fitting-based approach, the proposed method is found to provide improved accuracy in phase aberration compensation. The proposed method is observed to generate a halo effect at the sharp discontinuities in the aberration compensated phase. Consequently, the proposed algorithm aims to solve this problem by masking the object region during aberration estimation utilizing the numerically evaluated phase gradient map. The simulation results are provided for the qualitative and quantitative performance comparison between the proposed KF and ZP-based methods. The experimental results obtained from the recorded phase demonstrate the practical ability of the

proposed method.

Chapter 8

Conclusion and Future prospects

8.1 Conclusion

The main aim of any spatial carrier fringe pattern analysis technique is to accurately estimate the phase from a given fringe pattern. Such a phase estimation procedure involves multiple steps such as fringe pattern denoising, normalization, demodulation, etc. The limitations of state-of-art techniques developed to implement these steps are reported in the literature. The present thesis proposes Kalman filter(KF)-based spatial fringe pattern analysis algorithms to alleviate some of these limitations. The advantages offered by the proposed algorithm are low computational time, minimum or no user-defined parameters, high noise robustness, and high accuracy (even at image boundary or discontinuity). In addition, the problem of phase aberration compensation is also addressed in the thesis work.

The most important step involved in the implementation of KF is the state-space modeling depending the problem at hand. Accordingly, different state-space models are developed for the purpose of fringe denoising, fringe normalization, fringe demodulation, etc. The state-space models either involve linear or non-linear process update or measurement update equations. Accordingly, linear KF or non-linear KF are used for the state estimation. Since the measurements available in the form of two-dimensional grid of fringe intensities, fixed-length state estimate smoother algorithm is utilized for improving the state estimation accuracy. The process noise covariance and measurement noise covariance are two important algorithm parameters which decide the KF performance. These parameters are usually selected empirically depending on the prior knowledge of the process and measurement. In the present thesis, guidelines for the selection these parameters are provided for the effective implementation of the algorithms. Furthermore,

the adaptive estimation of these parameters are also utilized for improving the state estimation accuracy. Since the state estimation is performed pixel-wise, either row-column or zigzag scanning is performed depending the type of fringe pattern.

The performances of all the KF-based fringe processing algorithms are numerically evaluated with under different conditions with simulation examples. The performance comparisons are provided with the state-of-art algorithms. The simulation results validates the effectiveness of the proposed algorithms in terms of accuracy, noise robustness and low computational complexity. The practical applicability of these algorithms are demonstrated with the fringe patterns recorded in different measurement setups such as electronic speckle pattern interferometry, digital holograghic interferometry, digital holographic microscopy, optical interferometry, and fringe projection profilometry. We believe that the proposed set of algorithms can be an important contribution in the field of fringe pattern analysis. The ubiquity of KF allows the proposed set of algorithm to provide a single platform for all the fringe processing operations.

8.2 Scope of the Future Work

Based on the outcomes of this thesis work, possible directions for the further research are outlined below.

- Most of the proposed algorithms consider either the row/column-wise or the zigzag scanning of fringe pattern. **However, it may be advantageous to perform the localized fringe pattern analysis considering a two-dimensional window around each pixel.**
- The computational efficiency can be further enhanced with the implementation of the proposed algorithms using graphical processing units.
- The closed fringe pattern demodulation is currently limited to fringe patterns defined over a circular region. In addition, the underlying phase is assumed to be continuous. It will be useful to explore other polynomial functions for more efficient phase representation.
- The Kalman filter formulation in combination with quality-guided scanning of the phase pattern can be utilized for noise-robust phase unwrapping.
- It will be worth exploring the extension of the proposed algorithms in temporal fringe pattern analysis.

Bibliography

[1] S. Sharma and R. Kulkarni, "Noise reduction in speckle interferometry fringe pattern using adaptive kalman filter," *Optical Engineering*, vol. 60, no. 12, pp. 124 105–124 105, 2021.

[2] S. Sharma, R. Kulkarni, A. Vishnoi, and R. Gannavarpu, "Wrapped phase denoising using adaptive kalman smoother algorithm," *Journal of Modern Optics*, vol. 69, no. 15, pp. 838–849, 2022.

[3] S. Sharma, R. Kulkarni, S. Ajithaprasad, and R. Gannavarpu, "Fringe pattern normalization algorithm using kalman filter," *Results in Optics*, vol. 5, p. 100152, 2021.

[4] S. Sharma and R. Kulkarni, "Phase demodulation from a spatial carrier fringe pattern using extended complex kalman filter," *Optics and Lasers in Engineering*, vol. 138, 2020.

[5] S. Sharma and R. Kulkarni, "Adaptive extended complex kalman filter based spatial carrier fringe pattern demodulation," *Asian Journal of Physics*, vol. 31, pp. 961–971, 2022.

[6] S. Sharma and R. Kulkarni, "State-space modeling approach for fringe pattern demodulation," *Applied Optics*, vol. 62, no. 27, pp. 7330–7337, 2023.

[7] S. Sharma and R. Kulkarni, "Fringe pattern demodulation using zernike polynomials and a l1-norm regularized extended kalman filter," *Applied Optics*, vol. 61, no. 18, pp. 5517–5523, 2022.

[8] P. K. Rastogi, *Digital Speckle Pattern Interferometry and Related Techniques*, 2000.

[9] Z. M. Daniel Malacare, Manuel Servin, *Interferogram Analysis for Optical Testing*. Taylor Francis Publishers, 2005, no. 1.

[10] V. Pagliarulo and P. Ferraro, "New applications of electronic speckle pattern interferometry in novel materials and structures," in *Proceedings of SPIE - The International Society for Optical Engineering*, vol. 11059, 2019.

[11] J. Baqersad, P. Poozesh, C. Niezrecki, and P. Avitabile, "Photogrammetry and optical methods in structural dynamics – A review," *Mechanical Systems and Signal Processing*, vol. 86, pp. 17–34, 2017.

[12] T. Sun, P. Lu, Z. Zhuo, W. Zhang, and J. Lu, "Single-shot two-channel fresnel bimirror interferometric microscopy for quantitative phase imaging of biological cell," *Optics Communications*, vol. 426, pp. 77–83, 2018.

[13] P. M. . Servin M, Quiroga JA, "Fringe pattern analysis for optical metrology: theory, algorithms, and applications." 2014.

[14] J. Vargas, S. Wang, J. A. Gómez-Pedrero, and J. C. Estrada, "Robust weighted principal components analysis demodulation algorithm for phase-shifting interferometry," *Opt. Express*, vol. 29, no. 11, pp. 16 534–16 546, May 2021.

[15] M. A. Escobar, J. C. Estrada, and J. Vargas, "Phase-shifting vu factorization for interferometry," *Optics and Lasers in Engineering*, vol. 124, p. 105797, 2020.

[16] C. Quan, H. Niu, and C. Tay, "An improved windowed fourier transform for fringe demodulation," *Optics and Laser Technology*, vol. 42, no. 1, pp. 126–131, 2010.

[17] R. Kulkarni and P. Rastogi, *Single and Multicomponent Digital Optical Signal Analysis*, ser. 2053-2563. IOP Publishing, 2017.

[18] J. Vargas, S. Wang, J. A. Gómez-Pedrero, and J. C. Estrada, "Robust weighted principal components analysis demodulation algorithm for phase-shifting interferometry," *Optics Express*, vol. 29, no. 11, pp. 16 534–16 546, 2021.

[19] M. Servin and J. Estrada, "Analysis and synthesis of phase shifting algorithms based on linear systems theory," *Optics and Lasers in Engineering*, vol. 50, no. 8, pp. 1009–1014, 2012.

[20] J. W. Goodman, *Introduction to Fourier optics*. Roberts and Company Publishers, 2005, no. 1.

[21] A. T. Fleury, F. C. Trigo, and F. P. R. Martins, "A new approach based on computer vision and non-linear kalman filtering to monitor the nebulization quality of oil flames," *Expert systems with applications*, vol. 40, no. 12, pp. 4760–4769, 2013.

[22] M. B. Alatise and G. P. Hancke, "Pose estimation of a mobile robot based on fusion of imu data and vision data using an extended kalman filter," *Sensors*, vol. 17, no. 10, p. 2164, 2017.

[23] S. F. Schmidt, "The kalman filter-its recognition and development for aerospace applications," *Journal of Guidance and Control*, vol. 4, no. 1, pp. 4–7, 1981.

[24] J. Ali and M. Ushaq, "A consistent and robust kalman filter design for in-motion alignment of inertial navigation system," *Measurement*, vol. 42, no. 4, pp. 577–582, 2009.

[25] J. Tan and N. Kyriakopoulos, "Implementation of a tracking kalman filter on a digital signal processor," *IEEE transactions on industrial electronics*, vol. 35, no. 1, pp. 126–134, 1988.

[26] R. Vullings, B. De Vries, and J. W. Bergmans, "An adaptive kalman filter for ecg signal enhancement," *IEEE transactions on biomedical engineering*, vol. 58, no. 4, pp. 1094–1103, 2010.

[27] R. Zhan and J. Wan, "Neural network-aided adaptive unscented kalman filter for nonlinear state estimation," *IEEE Signal Processing Letters*, vol. 13, no. 7, pp. 445–448, 2006.

[28] X. Xie, "Iterated unscented kalman filter for phase unwrapping of interferometric fringes," *Optics Express*, vol. 24, no. 17, pp. 18 872–18 897, 2016.

[29] W. Zhou and J. Hou, "A new adaptive robust unscented kalman filter for improving the accuracy of target tracking," *IEEE Access*, vol. 7, pp. 77 476–77 489, 2019.

[30] G. Valverde and V. Terzija, "Unscented kalman filter for power system dynamic state estimation," *IET generation, transmission & distribution*, vol. 5, no. 1, pp. 29–37, 2011.

[31] P. R. Rishikesh Kulkarni, "Fringe denoising algorithms: A review," *Optics and Lasers in Engineering*, June 3 2020.

[32] L. X. . Yu Q, Sun X, "Spin filtering with curve windows for interferometric fringe patterns." *Proc SPIE Int Soc Opt Eng*, 2001.

[33] L. X ., Yu Q , Sun X , "Removing speckle noise from speckle fringe patterns by spin filtering with curved surface windows." *Proc SPIE Int Soc Opt Eng*, 2002.

[34] L. Cheng, C. Tang, S. Yan, X. Chen, L. Wang, and B. Wang, "New fourth-order partial differential equations for filtering in electronic speckle pattern interferometry fringes," *Optics Communications*, vol. 284, no. 24, pp. 5549–5555, 2011.

[35] W. Xu, C. Tang, F. Gu, and J. Cheng, "Combination of oriented partial differential equation and shearlet transform for denoising in electronic speckle pattern interferometry fringe patterns," *Appl. Opt.*, vol. 56, no. 10, pp. 2843–2850, Apr 2017.

[36] M. M. . Luis A, Louis LP, "Image selective smoothing and edge detection by nonlinear diffusion." *II. Siam J Num Anal*, vol. 29, 1992.

[37] C. Tang, L. Han, H. Ren, D. Zhou, Y. Chang, X. Wang, and X. Cui, "Second-order oriented partial-differential equations for denoising in electronic-speckle-pattern interferometry fringes," *Optics letters*, vol. 33, no. 19, pp. 2179–2181, 2008.

[38] L. Cheng, C. Tang, S. Yan, X. Chen, L. Wang, and B. Wang, "New fourth-order partial differential equations for filtering in electronic speckle pattern interferometry fringes," *Optics Communications*, vol. 284, no. 24, pp. 5549–5555, 2011.

[39] A. J. E. J. C. J. . Vargas J, COS S, "Fringe pattern denoising by image dimensionality reduction." *Opt Laser Eng*, vol. 51, 2013.

[40] B. Li, C. Tang, G. Gao, M. Chen, S. Tang, and Z. Lei, "General filtering method for electronic speckle pattern interferometry fringe images with various densities based on variational image decomposition," *Applied Optics*, vol. 56, no. 16, pp. 4843–4853, 2017.

[41] M. Wielgus and K. Patorski, "Filtering espi fringe images with non-local means algorithm," in *Fringe 2013: 7th International Workshop on Advanced Optical Imaging and Metrology*. Springer, 2014, pp. 317–320.

[42] Y. Tounsi, M. Kumar, A. Nassim, and F. Mendoza-Santoyo, "Speckle noise reduction in digital speckle pattern interferometric fringes by nonlocal means and its related adaptive kernel-based methods," *Applied Optics*, vol. 57, no. 27, pp. 7681–7690, 2018.

[43] M. Zhao and K. Qian, "Wff-bm3d: a hybrid denoising scheme for fringe patterns," in *International Conference on Optical and Photonic Engineering (icOPEN 2015)*, vol. 9524. SPIE, 2015, pp. 564–569.

[44] H. A. Aebischer and S. Waldner, "A simple and effective method for filtering speckle-interferometric phase fringe patterns," *Optics Communications*, vol. 162, no. 4, pp. 205–210, 1999.

[45] F. Palacios, E. Gonçalves, J. Ricardo, and J. L. Valin, "Adaptive filter to improve the performance of phase-unwrapping in digital holography," *Optics Communications*, vol. 238, no. 4, pp. 245–251, 2004.

[46] Y.-H. Li, S.-L. Qu, X.-J. Chen, and Z.-Y. Luo, "Phase pattern denoising using a regularized cost function with complex-valued Markov random fields based on a discrete model," *Appl. Opt.*, vol. 49, no. 36, pp. 6845–6849, Dec 2010.

[47] J. Villa, R. Rodríguez-Vera, J. Antonio Quiroga, I. de la Rosa, and E. González, "Anisotropic phase-map denoising using a regularized cost-function with complex-valued Markov-random-fields," *Optics and Lasers in Engineering*, vol. 48, no. 6, pp. 650–656, 2010.

[48] H. C. . Hong KC, Hyun SR, "Least-squares fitting of the phase map obtained in phase-shifting electronic speckle pattern interferometry." *Opt Lett*, vol. 20, 1995.

[49] C. Tang, W. Wang, H. Yan, and X. Gu, "Tangent least-squares fitting filtering method for electrical speckle pattern interferometry phase fringe patterns," *Appl. Opt.*, vol. 46, no. 15, pp. 2907–2913, May 2007.

[50] C. Tang, L. Han, H. Ren, T. Gao, Z. Wang, and K. Tang, "The oriented-couple partial differential equations for filtering in wrapped phase patterns," *Opt. Express*, vol. 17, no. 7, pp. 5606–5617, Mar 2009.

[51] Q. Kemao, W. Gao, and H. Wang, "Windowed Fourier-filtered and quality-guided phase-unwrapping algorithm," *Appl. Opt.*, vol. 47, no. 29, pp. 5420–5428, Oct 2008.

[52] C. Li, C. Tang, H. Yan, L. Wang, and H. Zhang, "Localized Fourier transform filter for noise removal in electronic speckle pattern interferometry wrapped phase patterns," *Appl. Opt.*, vol. 50, no. 24, pp. 4903–4911, Aug 2011.

[53] H. A. Aebischer and S. Waldner, "A simple and effective method for filtering speckle-interferometric phase fringe patterns," *Optics Communications*, vol. 162, no. 4-6, pp. 205–210, 1999.

[54] C. Tang, F. Zhang, H. Yan, and Z. Chen, "Denoising in electronic speckle pattern interferometry fringes by the filtering method based on partial differential equations," *Optics communications*, vol. 260, no. 1, pp. 91–96, 2006.

[55] C. Tang, F. Zhang, B. Li, and H. Yan, "Performance evaluation of partial differential equation models in electronic speckle pattern interferometry and the δ-mollification phase map method," *Applied optics*, vol. 45, no. 28, pp. 7392–7400, 2006.

[56] N. Escalante, J. Villa, I. de la Rosa, E. de la Rosa, E. González-Ramírez, O. Gutiérrez, C. Olvera, and M. Araiza, "2-d continuous wavelet transform for espi phase-maps denoising," *Optics and Lasers in Engineering*, vol. 51, no. 9, pp. 1060–1065, 2013.

[57] M. K. F. M.-S. Sara Zada, Yassine Tounsi and A. Nassima, "Contribution study of monogenic wavelets transform to reduce speckle noise in digital speckle patter interferometry," *Opt. Eng.*, vol. 58, March 2019.

[58] R. Kulkarni and P. Rastogi, "Patch-wise denoising of phase fringe patterns based on matrix enhancement," *Optics and Lasers in Engineering*, vol. 87, pp. 191–196, 2016.

[59] K. Yan, Y. Yu, C. Huang, L. Sui, K. Qian, and A. Asundi, "Fringe pattern denoising based on deep learning," *Optics Communications*, vol. 437, pp. 148–152, 2019.

[60] J. Gurrola-Ramos, O. Dalmau, and T. Alarcon, "U-net based neural network for fringe pattern denoising," *Optics and Lasers in Engineering*, vol. 149, p. 106829, 2022.

[61] K. Yan, Y. Yu, T. Sun, A. Asundi, and Q. Kemao, "Wrapped phase denoising using convolutional neural networks," *Optics and Lasers in Engineering*, vol. 128, p. 105999, 2020.

[62] K. Yan, L. Chang, M. Andrianakis, V. Tornari, and Y. Yu, "Deep learning-based wrapped phase denoising method for application in digital holographic speckle pattern interferometry," *Applied Sciences*, vol. 10, no. 11, p. 4044, 2020.

[63] J. A. Quiroga, J. Antonio Gómez-Pedrero, and Ángel Garcıa-Botella, "Algorithm for fringe pattern normalization," *Optics Communications*, vol. 197, no. 1, pp. 43–51, 2001.

[64] J. A. Quiroga and M. Servin, "Isotropic n-dimensional fringe pattern normalization," *Optics communications*, vol. 224, no. 4-6, pp. 221–227, 2003.

[65] N. A. Ochoa and A. Silva-Moreno, "Normalization and noise-reduction algorithm for fringe patterns," *Optics Communications*, vol. 270, no. 2, pp. 161–168, 2007.

[66] J. A. Guerrero, J. L. Marroquin, M. Rivera, and J. A. Quiroga, "Adaptive monogenic filtering and normalization of ESPI fringe patterns," *Optics Letters*, vol. 30, no. 22, pp. 3018–3020, Nov 2005.

[67] M. B. Bernini, A. Federico, and G. H. Kaufmann, "Normalization of fringe patterns using the bidimensional empirical mode decomposition and the Hilbert transform," *Applied Optics*, vol. 48, no. 36, pp. 6862–6869, Dec 2009.

[68] J. S.-S. Y. . H.-M. Tien, Chuen-Lin, "A method for fringe normalization by Zernike polynomial," *Optical Review*, vol. 16, no. 2, pp. 173–175, 2009.

[69] C. Tian and S. Liu, "Demodulation of two-shot fringe patterns with random phase shifts by use of orthogonal polynomials and global optimization," *Optics Express*, vol. 24, no. 4, pp. 3202–3215, 2016.

[70] J. Xu, Q. Xu, and H. Peng, "Spatial carrier phase-shifting algorithm based on least-squares iteration," *Applied optics*, vol. 47, no. 29, pp. 5446–5453, 2008.

[71] J. Muñoz-Maciel, M. Mora-Gonzalez, V. M. Duran-Ramírez, F. J. Casillas-Rodriguez, and F. G. Peña-Lecona, "Spatial carrier phase shifting method for the phase recovery from two interferograms with closed fringes," *Optics Communications*, vol. 437, pp. 226–230, 2019.

[72] M. Takeda, H. Ina, and S. Kobayashi, "Fourier-transform method of fringe-pattern analysis for computer-based topography and interferometry," *JosA*, vol. 72, no. 1, pp. 156–160, 1982.

[73] M. Takeda and K. Mutoh, "Fourier transform profilometry for the automatic measurement of 3-d object shapes," *Applied optics*, vol. 22, no. 24, pp. 3977–3982, 1983.

[74] Q. Kemao, "Windowed fourier transform method for demodulation of carrier fringes," *Optical Engineering*, vol. 43, no. 7, pp. 1472–1473, 2004.

[75] Q. Kemao, "Two-dimensional windowed fourier transform for fringe pattern analysis: principles, applications and implementations," *Optics and Lasers in Engineering*, vol. 45, no. 2, pp. 304–317, 2007.

[76] B. D. . Gdeisat M, Lalor M, "Spatial carrier-fringe demodulation by use of a two-dimensional wavelet transform ." *Applied Optics*, vol. 45, 2000.

[77] D. R. B. Munther A. Gdeisat, Abdulbasit Abid, "Spatial and temporal carrier fringe pattern demodulation using the one-dimensional continous wavelet transform : Recent progress, challenges and suggested developments ." *Optics and Lasers in Engineeringn*, vol. 47, 2009.

[78] T. H. O. S. E. N. Dursun A, Sarac Z, "Phase recovery from interferance fringes by using s-transform." *Measurement*, vol. 41, 2008.

[79] M. Trusiak, Ł. Służewski, and K. Patorski, "Single shot fringe pattern phase demodulation using hilbert-huang transform aided by the principal component analysis," *Optics Express*, vol. 24, no. 4, pp. 4221–4238, 2016.

[80] M. Cywińska, M. Trusiak, K. Patorski, J. A. Picazo-Bueno, and V. Mico, "Modified variational image decomposition algorithm aided by the hilbert transform as an alternative to 2d hilbert-huang transform for fringe pattern phase retrieval," in *Speckle 2018: VII International Conference on Speckle Metrology*, vol. 10834. SPIE, 2018, pp. 536–547.

[81] C. Tian, Y. Yang, D. Liu, Y. Luo, and Y. Zhuo, "Demodulation of a single complex fringe interferogram with a path-independent regularized phase-tracking technique," *Applied optics*, vol. 49, no. 2, pp. 170–179, 2010.

[82] L. Kai and Q. Kemao, "A generalized regularized phase tracker for demodulation of a single fringe pattern," *Optics Express*, vol. 20, no. 11, pp. 12 579–12 592, 2012.

[83] X. Zhu, C. Tang, B. Li, C. Sun, and L. Wang, "Phase retrieval from single frame projection fringe pattern with variational image decomposition," *Optics and Lasers in Engineering*, vol. 59, pp. 25–33, 2014.

[84] M. Servin, J. Marroquin, and F. Cuevas, "Demodulation of a single interferogram by use of a two-dimensional regularized phase-tracking technique," *Applied Optics*, vol. 36, no. 19, pp. 4540–4548, 1997.

[85] M. Servin, J. Marroquin, and F. Cuevas, "Fringe-follower regularized phase tracker for demodulation of closed-fringe interferograms," *JOSA A*, vol. 18, no. 3, pp. 689–695, 2001.

[86] C. Tian, Y. Yang, D. Liu, Y. Luo, and Y. Zhuo, "Demodulation of a single complex fringe interferogram with a path-independent regularized phase-tracking technique," *Applied Optics*, vol. 49, no. 2, pp. 170–179, 2010.

[87] L. Kai and Q. Kemao, "A generalized regularized phase tracker for demodulation of a single fringe pattern," *Opt. Express*, vol. 20, no. 11, pp. 12 579–12 592, May 2012.

[88] L. Kai and Q. Kemao, "Improved generalized regularized phase tracker for demodulation of a single fringe pattern," *Opt. Express*, vol. 21, no. 20, pp. 24 385–24 397, Oct 2013.

[89] C. Tian, Y. Yang, S. Zhang, D. Liu, Y. Luo, and Y. Zhuo, "Regularized frequency-stabilizing method for single closed-fringe interferogram demodulation," *Optics letters*, vol. 35, no. 11, pp. 1837–1839, 2010.

[90] K. G. Larkin, D. J. Bone, and M. A. Oldfield, "Natural demodulation of two-dimensional fringe patterns. i. general background of the spiral phase quadrature transform," *JOSA A*, vol. 18, no. 8, pp. 1862–1870, 2001.

[91] J. Estrada, M. Servin, and J. Marroquín, "Local adaptable quadrature filters to demodulate single fringe patterns with closed fringes." *Optics Express*, vol. 15, no. 5, pp. 2288–2298, 2007.

[92] Q. Kemao and L. Kai, "Fast frequency-guided sequential demodulation of a single fringe pattern," *Optics Letters*, vol. 35, no. 22, pp. 3718–3720, 2010.

[93] Ulises H. Rodriguez-Marmolejo, Miguel Mora-Gonzalez, Jesus Muñoz-Maciel, Tania A. Ramirez-delreal, "FSD-HSO Optimization Algorithm for Closed Fringes Interferogram Demodulation," *Mathematical Problems in Engineering*, march 2016.

[94] J. Ma, Z. Wang, B. Pan, T. Hoang, M. Vo, and L. Luu, "Two-dimensional continuous wavelet transform for phase determination of complex interferograms," *Appl. Opt.*, vol. 50, no. 16, pp. 2425–2430, Jun 2011.

[95] R. Kulkarni and P. Rastogi, "Simultaneous estimation of unwrapped phase and phase derivative from a closed fringe pattern," *Optics and Lasers in Engineering*, vol. 87, pp. 168–175, 2016.

[96] R. Kulkarni and P. Rastogi, "Closed fringe demodulation using phase decomposition by fourier basis functions," *Journal of the Optical Society of America A: Optics and Image Science, and Vision*, vol. 33, no. 6, pp. 1120–1125, 2016.

[97] C. Tian, Y. Yang, T. Wei, T. Ling, and Y. Zhuo, "Demodulation of a single-image interferogram using a zernike-polynomial-based phase-fitting technique with a differential evolution algorithm," *Optics letters*, vol. 36, no. 12, pp. 2318–2320, 2011.

[98] D. Kando, S. Tomioka, N. Miyamoto, and R. Ueda, "Phase extraction from single interferogram including closed-fringe using deep learning," *Applied Sciences*, vol. 9, no. 17, 2019.

[99] S. Yuan, Y. Hu, Q. Hao, and S. Zhang, "High-accuracy phase demodulation method compatible to closed fringes in a single-frame interferogram based on deep learning," *Optics express*, vol. 29, no. 2, pp. 2538–2554, 2021.

[100] Q. Weijuan, Y. Yingjie, C. O. Choo, and A. Asundi, "Digital holographic microscopy with physical phase compensation," *Optics letters*, vol. 34, no. 8, pp. 1276–1278, 2009.

[101] E. Sánchez-Ortiga, P. Ferraro, M. Martínez-Corral, G. Saavedra, and A. Doblas, "Digital holographic microscopy with pure-optical spherical phase compensation," *JOSA A*, vol. 28, no. 7, pp. 1410–1417, 2011.

[102] A. I. Doblas, E. Sánchez-Ortiga, M. Martínez-Corral, G. Saavedra, and J. Garcia-Sucerquia, "Accurate single-shot quantitative phase imaging of biological specimens with telecentric digital holographic microscopy," *Journal of biomedical optics*, vol. 19, no. 4, p. 046022, 2014.

[103] R. Castañeda and J. Garcia-Sucerquia, "Single-shot 3d topography of reflective samples with digital holographic microscopy," *Applied Optics*, vol. 57, no. 1, pp. A12–A18, 2018.

[104] H. Cui, D. Wang, Y. Wang, J. Zhao, and Y. Zhang, "Phase aberration compensation by spectrum centering in digital holographic microscopy," *Optics Communications*, vol. 284, no. 18, pp. 4152–4155, 2011.

[105] J. Min, B. Yao, S. Ketelhut, C. Engwer, B. Greve, and B. Kemper, "Simple and fast spectral domain algorithm for quantitative phase imaging of living cells with digital holographic microscopy," *Optics Letters*, vol. 42, no. 2, pp. 227–230, 2017.

[106] C. Zuo, Q. Chen, W. Qu, and A. Asundi, "Phase aberration compensation in digital holographic microscopy based on principal component analysis," *Optics letters*, vol. 38, no. 10, pp. 1724–1726, 2013.

[107] J. Min, B. Yao, S. Ketelhut, C. Engwer, B. Greve, and B. Kemper, "Simple and fast spectral domain algorithm for quantitative phase imaging of living cells with digital holographic microscopy," *Optics Letters*, vol. 42, no. 2, pp. 227–230, 2017.

[108] T. Colomb, F. Montfort, J. Kühn, N. Aspert, E. Cuche, A. Marian, F. Charrière, S. Bourquin, P. Marquet, and C. Depeursinge, "Numerical parametric lens for shifting, magnification, and complete aberration compensation in digital holographic microscopy," *JOSA A*, vol. 23, no. 12, pp. 3177–3190, 2006.

[109] X. Lai, S. Xiao, Y. Ge, K. Wei, and K. Wu, "Digital holographic phase imaging with aberrations totally compensated," *Biomedical Optics Express*, vol. 10, no. 1, pp. 283–292, 2019.

[110] J. Di, J. Zhao, W. Sun, H. Jiang, and X. Yan, "Phase aberration compensation of digital holographic microscopy based on least squares surface fitting," *Optics communications*, vol. 282, no. 19, pp. 3873–3877, 2009.

[111] D. Zhang, J. Fan, H. Zhao, X. Lu, S. Liu, and L. Zhong, "Error evaluation for zernike polynomials fitting based phase compensation of digital holographic microscopy," *Optik*, vol. 125, no. 18, pp. 5148–5152, 2014.

[112] T. Nguyen, G. Nehmetallah, C. Raub, S. Mathews, and R. Aylo, "Accurate quantitative phase digital holographic microscopy with single-and multiple-wavelength telecentric and nontelecentric configurations," *Applied Optics*, vol. 55, no. 21, pp. 5666–5683, 2016.

[113] T. Nguyen, V. Bui, V. Lam, C. B. Raub, L.-C. Chang, and G. Nehmetallah, "Automatic phase aberration compensation for digital holographic microscopy based on deep learning background detection," *Optics express*, vol. 25, no. 13, pp. 15 043–15 057, 2017.

[114] S. Liu, W. Xiao, and F. Pan, "Automatic compensation of phase aberrations in digital holographic microscopy for living cells investigation by using spectral energy analysis," *Optics & Laser Technology*, vol. 57, pp. 169–174, 2014.

[115] M. Tur, K. C. Chin, and J. W. Goodman, "When is speckle noise multiplicative?" *Appl. Opt.*, vol. 21, no. 7, pp. 1157–1159, Apr 1982.

[116] V. Kumar, A. Kumar Dubey, M. Gupta, V. Singh, A. Butola, and D. Singh Mehta, "Speckle noise reduction strategies in laser-based projection imaging, fluorescence microscopy, and digital holography with uniform illumination, improved image sharpness, and resolution," *Optics and Laser Technology*, vol. 141, 2021.

[117] R. Kulkarni and P. Rastogi, "Fringe denoising algorithms: A review," *Optics and Lasers in Engineering*, vol. 135, 2020.

[118] A. Schlogl, J. Fortin, W. Habenbacher, and M. Akay, "Adaptive mean and trend removal of heart rate variability using Kalman filtering," in *2001 Conference Proceedings of the 23rd Annual International Conference of the IEEE Engineering in Medicine and Biology Society*, vol. 1, 2001, pp. 571–573.

[119] R. Vullings, B. de Vries, and J. W. M. Bergmans, "An Adaptive Kalman Filter for ECG Signal Enhancement," *IEEE Transactions on Biomedical Engineering*, vol. 58, no. 4, pp. 1094–1103, 2011.

[120] S. Akhlaghi, N. Zhou, and Z. Huang, "Adaptive adjustment of noise covariance in Kalman filter for dynamic state estimation," in *IEEE Power Energy Society General Meeting*, 2017.

[121] S. D., *Optimal state estimation: Kalman, H∞, and nonlinear approaches.* John Wiley Sons,Ltd., 2006, pp. 1–526.

[122] Q. Kemao, "Two-dimensional windowed Fourier transform for fringe pattern analysis: Principles, applications and implementations," *Optics and Lasers in Engineering*, vol. 45, no. 2, pp. 304–317, 2007.

[123] J. Vargas, C. Sorzano, J. Antonio Quiroga, J. Estrada, and J. Carazo., "Fringe pattern denoising by image dimensionality reduction," *Optics and Lasers in Engineering*, vol. 51, no. 7, pp. 921–928, 2013.

[124] Q. Kemao, "Two-dimensional windowed Fourier transform for fringe pattern analysis: Principles, applications and implementations," *Optics and Lasers in Engineering*, vol. 45, no. 2, pp. 304–317, 2007.

[125] P. H.S., H. L. Shashidhara, and K. N. Balasubramanya Murthy, "Image Scaling Comparison Using Universal Image Quality Index," in *International Conference on Advances in Computing, Control, and Telecommunication Technologies*, 2009, pp. 859–863.

[126] Wang Yuanji, Li Jianhua, Lu Yi, Fu Yao, and Jiang Qinzhong, "Image quality evaluation based on image weighted separating block peak signal to noise ratio," in *International Conference on Neural Networks and Signal Processing, 2003*, vol. 2, pp. 994–997.

[127] T. R. Crimmins, "Geometric filter for speckle reduction," *Appl. Opt.*, vol. 24, no. 10, pp. 1438–1443, May 1985.

[128] Q. Kemao, "A simple phase unwrapping approach based on filtering by windowed Fourier transform: A note on the threshold selection," *Optics Laser Technology*, vol. 40, no. 8, pp. 1091–1098, 2008.

[129] M. Zhao, L. Huang, Q. Zhang, X. Su, A. Asundi, and Q. Kemao, "Quality-guided phase unwrapping technique: comparison of quality maps and guiding strategies," *Appl. Opt.*, vol. 50, no. 33, pp. 6214–6224, Nov 2011.

[130] S. Akhlaghi, N. Zhou, and Z. y. Huang, "Adaptive adjustment of noise covariance in kalman filter for dynamic state estimation," in *2017 IEEE Power & Energy Society General Meeting*, 2017, pp. 1–5.

[131] H. Xia, S. Montresor, R. Guo, J. Li, F. Yan, H. Cheng, and P. Picart, "Phase calibration unwrapping algorithm for phase data corrupted by strong decorrelation speckle noise," *Opt. Express*, vol. 24, no. 25, pp. 28 713–28 730, Dec 2016.

[132] P. Memmolo, M. Iannone, M. Ventre, P. A. Netti, A. Finizio, M. Paturzo, and P. Ferraro, "Quantitative phase maps denoising of long holographic sequences by using SPADEDH algorithm," *Appl. Opt.*, vol. 52, no. 7, pp. 1453–1460, Mar 2013.

[133] N. Escalante, J. Villa, I. de la Rosa, E. de la Rosa, E. González-Ramírez, O. Gutiérrez, C. Olvera, and M. Araiza, "2-D Continuous Wavelet Transform for ESPI phase-maps denoising," *Optics and Lasers in Engineering*, vol. 51, no. 9, pp. 1060–1065, 2013.

[134] S. Montresor and P. Picart, "Quantitative appraisal for noise reduction in digital holographic phase imaging," *Opt. Express*, vol. 24, no. 13, pp. 14 322–14 343, Jun 2016.

[135] A. Vishnoi and G. Rajshekhar, "Rapid deformation analysis in digital holographic interferometry using graphics processing unit accelerated wigner–ville distribution," *Appl. Opt.*, vol. 58, no. 16, pp. 4420–4424, Jun 2019.

[136] M. A. Herráez, D. R. Burton, M. J. Lalor, and M. A. Gdeisat, "Fast two-dimensional phase-unwrapping algorithm based on sorting by reliability following a noncontinuous path," *Applied optics*, vol. 41, no. 35, pp. 7437–7444, 2002.

[137] M.F.Kasim, "Fast 2D phase unwrapping implementation in MATLAB," 2017.

[138] Z. Wang and A. C. Bovik, "A Universal Image Quality Index," *IEEE Signal Processing Letters*, vol. 9, pp. 81–84, 2002.

[139] A. Patil, R. Langoju, P. Rastogi, and S. Ramani, "Statistical study and experimental verification of high-resolution methods in phase-shifting interferometry," *Journal of the Optical Society of America A: Optics and Image Science, and Vision*, vol. 24, no. 3, pp. 794–813, 2007.

[140] A. V. Satya Vithin, I. Show, S. Ajithaprasad, and R. Gannavarpu, "Demodulating interferograms with non-uniform amplitude variations for precision non-contact optical profilometry," *Optics and Lasers in Engineering*, vol. 134, p. 106292, 2020.

[141] A. V. S. Vithin, S. Ajithaprasad, and G. Rajshekhar, "Step phase reconstruction using an anisotropic total variation regularization method in a diffraction phase microscopy," *Applied Optics*, vol. 58, no. 26, pp. 7189–7194, Sep 2019.

[142] G.-B. . Quiroga JA, Gómez-Pedrero JA, "Algorithm for fringe pattern normalization." *Opt Communication*, vol. 197, 2001.

[143] R. M. Q. J. . Guerrero JA, Marroquin JL, "Adaptive monogenic filtering and normalization of espi fringe patterns." *Opt Lett*, vol. 30, 2005.

[144] P. G. R. A. . Dash PK, Jena RK, "An extended complex kalman filter for frequency measurement of distorted signals." *IEEE Trans Instrum Meas*, vol. 49, 2000.

[145] M. Takeda and K. Mutoh, "Fourier transform profilometry for the automatic measurement of 3-d object shapes," *Appl. Opt.*, vol. 22, no. 24, pp. 3977–3982, Dec 1983.

[146] J. L. Marroquin, M. Servin, and R. Rodriguez-Vera, "Adaptive quadrature filters and the recovery of phase from fringe pattern images," *J. Opt. Soc. Am. A*, vol. 14, no. 8, pp. 1742–1753, Aug 1997.

[147] J. Antonio Quiroga and M. Servin, "Isotropic n-dimensional fringe pattern normalization," *Optics Communications*, vol. 224, no. 4, pp. 221–227, 2003.

[148] E. Siavashi, S. Afsharnia, M. T. Bina, M. K. Zadeh, and M. Baradar, "Frequency estimation of distorted signals in power systems using particle extended kalman filter," in *2009 2nd International Conference on Power Electronics and Intelligent Transportation System (PEITS)*, vol. 1. IEEE, 2009, pp. 174–178.

[149] S. Sharma and R. Kulkarni, "Phase demodulation from a spatial carrier fringe pattern using extended complex kalman filter," *Optics and Lasers in Engineering*, vol. 138, p. 106409, 2021.

[150] J. Antonio Quiroga and M. Servin, "Isotropic n-dimensional fringe pattern normalization," *Optics Communications*, vol. 224, no. 4, pp. 221–227, 2003.

[151] J. A. Guerrero, J. L. Marroquin, M. Rivera, and J. A. Quiroga, "Adaptive monogenic filtering and normalization of espi fringe patterns," *Opt. Lett.*, vol. 30, no. 22, pp. 3018–3020, Nov 2005.

[152] R. J. Noll, "Zernike polynomials and atmospheric turbulence," *JOsA*, vol. 66, no. 3, pp. 207–211, 1976.

[153] A. Prata and W. V. T. Rusch, "Algorithm for computation of zernike polynomials expansion coefficients," *Appl. Opt.*, vol. 28, no. 4, pp. 749–754, Feb 1989.

[154] C. Zhang, J.-Z. Huang, G.-Q. Song, and L. Chen, "Structural damage identification by extended k alman filter with l 1-norm regularization scheme," *Structural Control and Health Monitoring*, vol. 24, no. 11, p. e1999, 2017.

[155] A. Carmi, P. Gurfil, and D. Kanevsky, "Methods for sparse signal recovery using kalman filtering with embedded pseudo-measurement norms and quasi-norms," *IEEE Transactions on Signal Processing*, vol. 58, no. 4, pp. 2405–2409, 2010.

[156] A. V. S. Vithin, A. Vishnoi, and R. Gannavarpu, "Phase derivative estimation in digital holographic interferometry using a deep learning approach," *Applied Optics*, vol. 61, no. 11, pp. 3061–3069, 2022.

[157] K. Lee, K. Kim, J. Jung, J. Heo, S. Cho, S. Lee, G. Chang, Y. Jo, H. Park, and Y. Park, "Quantitative phase imaging techniques for the study of cell pathophysiology: from principles to applications," *Sensors*, vol. 13, no. 4, pp. 4170–4191, 2013.

[158] G. Nehmetallah and P. P. Banerjee, "Applications of digital and analog holography in three-dimensional imaging," *Advances in Optics and Photonics*, vol. 4, no. 4, pp. 472–553, 2012.